Spin Evolution of Galaxies in the Magneticum Pathfinder Simulations

Silvio Fortuné

Munich 2022

Drehimpulsentwicklung von Galaxien in den Simulationen von Magneticum Pathfinder

Silvio Fortuné

München 2022

Spin Evolution of Galaxies in the Magneticum Pathfinder Simulations

Silvio Fortuné

Master's Thesis

at the University Observatory Munich

Ludwig Maximilian University

Submitted by

Silvio Fortuné

born in Munich

Supervised by

Klaus Dolag

Rhea-Silvia Remus

Lucas Valenzuela

Munich, 08.08.2022

Contents

Chapter 1

Introduction

As far as we can trace back human history, we find evidence of people trying to understand the phenomena of the night sky. While most of the objects discovered there lie far beyond our reach, they have inspired us not only to search for the origin of the universe and humankind but also to discover technical and cultural advancements. Popular examples are making use of celestial bodies for naval navigation, providing proof of the general relativity theory and the desire to reach moons and planets. Among the objects discoverable by bare eye were galaxies: the most common accumulation of bound material in the universe. As hosts of stars, galaxies play a key role connecting the small scales of star formation with the large scale structures of the universe as inhabitants of clusters and the cosmic web. In addition to that, they let us understand the evolution of the universe from as far back as $z \approx 13$ (Cooper, 2022) until today. Galaxies appear in various different shapes, sizes and colors. The features we find in them today tell us the story of their formation path and the more we learn to analyze their features, the better we understand their interaction with larger-scale structures.

Over the last decades, numerous series of surveys such as HDF (Williams et al., 1996), SDSS (York & SDSS Collaboration, 2000), DES (The Dark Energy Survey Collaboration, 2005), GAMA (Baldry et al., 2008) and GAIA (Gaia Collaboration, 2016) added millions of galaxies with photometric and spectral data to be analyzed. With updates to these surveys and new observations with the *James Webb Space Telescope*, we are provided with the means for more and more insight. They allowed for statistical methods like weak lensing to understand matter distribution in clusters or let us trace the cosmic web with galaxy-position-based structure finders like DisPerSE (Sousbie, 2011; Sousbie et al., 2011).

With observations improving on one side, computational power and numerical methods made extensive cosmological hydrodynamical simulations possible with box lengths of up to 3.818 Gpc. To date, several simulations (see section 2.1) include baryonic and dark matter

interplay, plasma physics, feedback, sub-grid models and zoom simulations. With simulations, we can see explicitly watch structure forming over cosmological time scales and follow the evolution path leading to the cosmic web. In Figure 1.1 the cosmic web becomes visualized mainly through gas, but also through the distribution of galaxies.

(a) 500 Mpc   (b) 25 Mpc
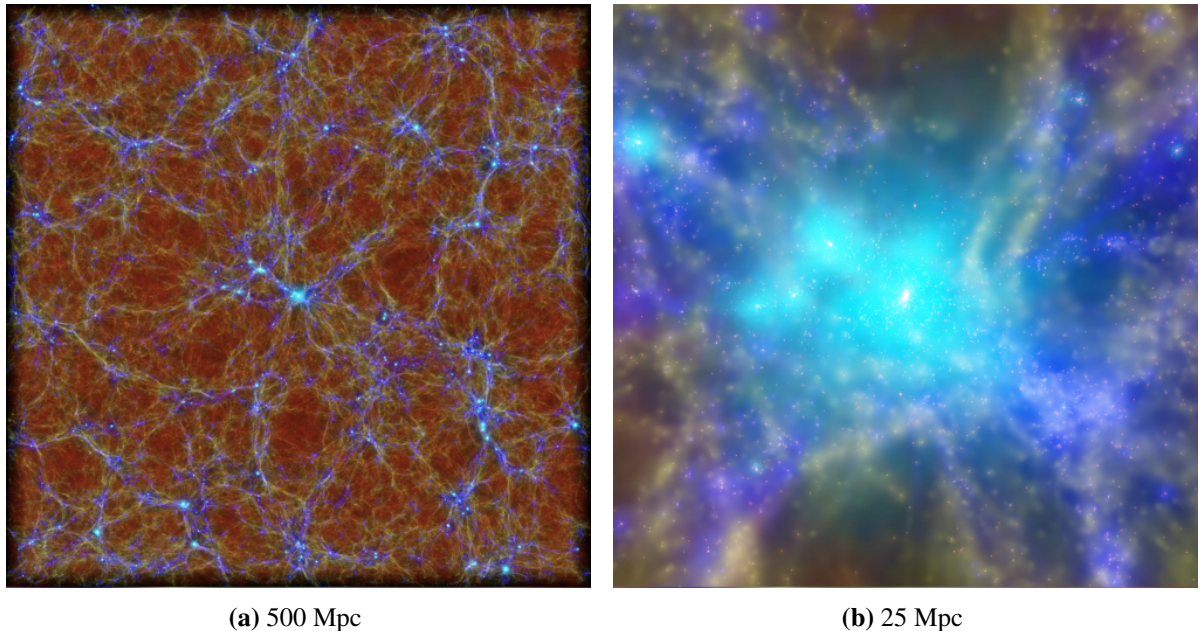
Figure 1.1: Visualizations of Magneticum Box2/hr at $z = 0$ with stars/galaxies (white) and gas colored by temperature Full box with side length of 500 Mpc (left) and zoom onto a 25 Mpc region around the most massive cluster in the simulation. Courtesy of Dolag (2016a).

Our understanding of the connection of galaxies with the cosmic web heavily depends on how well we understand their formation histories. Two types of formation scenarios have been in the discussion for galaxies: "top-down" by large structures breaking up into substructures producing galaxies or "bottom-up" with galaxies growing as they accrete other galaxies (Peebles, 1993). The former used to be popular, which also lead to the naming convention in the Hubble tuning fork with "early-type" galaxies evolving into "late-type" galaxies in Figure 1.2a. Stellar ages and peculiar velocities of galaxies in the local group spread doubt about the top-down scenario. As the fundamental plane for ellipticals (Oegerle & Hoessel, 1991) and the Tully-Fisher relation, tightly connecting luminosity and rotation velocity of disks (Tully & Fisher, 1977), asked for a unifying assembly model, the bottom-up accretion scenario became favored. Fall (1983) found that the different morphological groups of galaxies follow parallel tracks in the j_*-M_*-plane (revised by Romanowsky & Fall (2012) and Fall & Romanowsky (2013)) a classification scheme as displayed in Figure 1.2b emerged.

These parallel tracks scale as

$$\log_{10}\left(\frac{j_*}{\text{kpc km/s}}\right) \propto \frac{2}{3}\,\log_{10}\left(\frac{M_*}{M_\odot}\right) \tag{1.1}$$

The classification scheme was further refined by the introduction of the b-value by Teklu et al. (2015), who also revealed strong relation to the circularity parameter (Scannapieco et al., 2008; Abadi et al., 2003)

$$\varepsilon \equiv \frac{j_z}{rV_{\text{circ}}} \tag{1.2}$$

that compares the z-component of the measured spin to the idealized circular-disk case. Supporting the b-value as a valid quantity for morphological classification, Schulze et al. (2018) showed clear relations with the ellipticity

$$\epsilon \equiv 1 - \frac{b}{a} \tag{1.3}$$

and

$$\lambda_R \equiv \frac{\langle R\,|V|\rangle}{\langle R\,\sqrt{V^2 + \sigma^2}\rangle} \tag{1.4}$$

quantifying the amount of stellar rotation in the system (Emsellem et al., 2007). While the b-value provides a gradual scale for the degree of rotational support, Kudritzki et al. (2021) and Mayer et al. (2022) inferred thresholds to classify galaxies into disks, intermediates and spheroids.
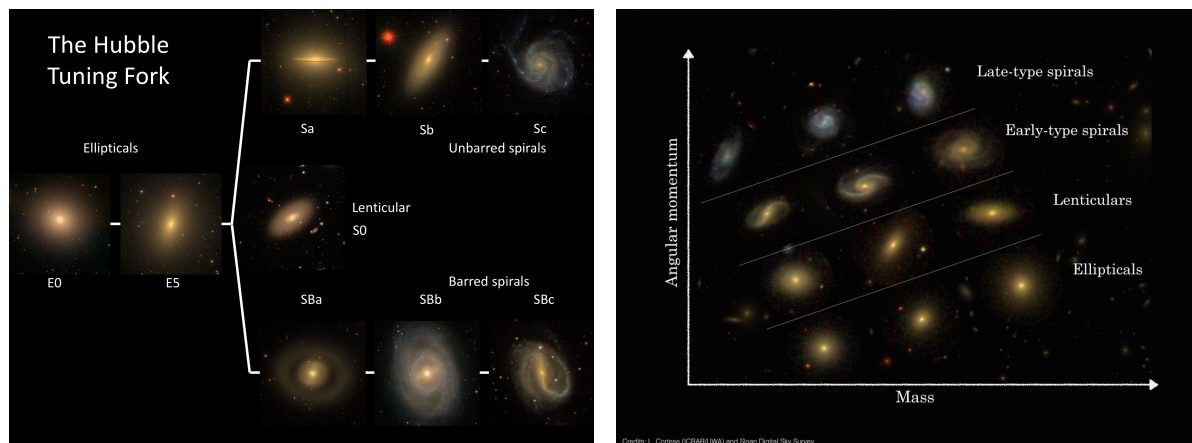

(a) Hubble tuning-fork. Credits: Masters (2019)

(b) Classification by angular momentum. Credits: Cortese (2016)

Figure 1.2: Example galaxies for morphological types drawn from the SDSS catalogue and ordered along the Hubble-tuning-fork classification scheme (left) and the spin-based classification scheme that will be used later in this work.

In this work the evolution of kinematic features will be traced through time. The assumptions for the interpretation of the galaxy formation histories rely on the bottom-up formation scenario, which is characterized by the attraction of smaller galaxies to walls, filaments and massive galaxy clusters, sitting at the nodes of the cosmic web. On their way to the overdense regions, they accrete gas and galaxies which change their angular momentum anisotropically and could, for instance align the galaxy's spin vector with the filament spine. This picture is outlined in Figure 1.3.
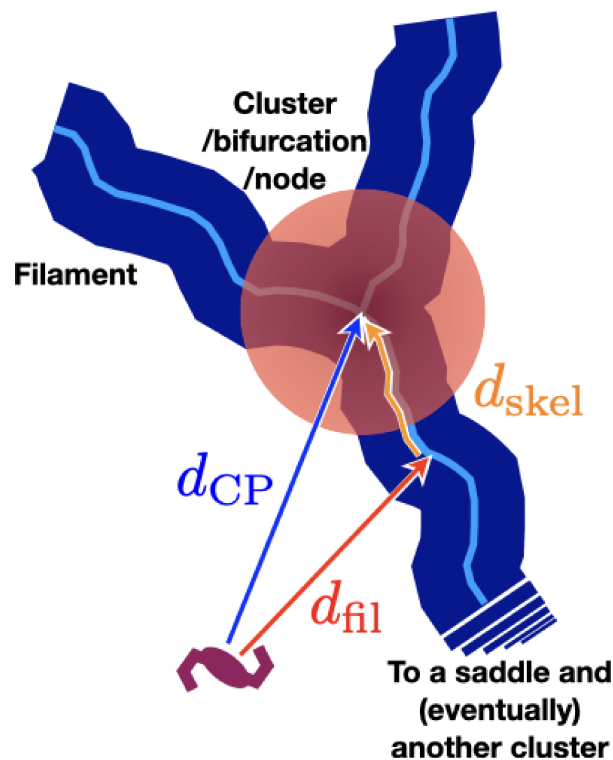

Figure 1.3: Schematics by Malavasi et al. (2021) of a galaxy near filaments and nodes. In their work, the arrows represent the distance types they considered for their analysis. The red and yellow arrows draw the idealized pathway of a galaxy in the bottom-up structure formation scenario.

In effort to find evidence for these processes, galactic kinematics and morphology play an essential role, as they serve as tracers for the interaction with the cosmic web. Without interaction with outside influences, angular momentum is a conserved quantity, initially determined by collapsing gas and dark matter with tidal torque from the surroundings. Over time, the gas condenses in the center and forms the stars that inherit a fixed fraction of the initial spin. In case of an undisturbed halo, the disk spin should hold a fraction of the halo spin corresponding to the mass fraction (Mo et al., 1998). As the galaxies approach the filaments, they accrete mass primarily via satellites that fall into the center of a halo preferentially perpendicular to the spin vector (Aubert et al., 2004; Knebe et al., 2004). With the assumption of directional

accretion onto galaxies while approaching filaments, Welker et al. (2020) used data from simulations and observations to find that galactic masses are larger the closer they are to the filaments. Increasing mass also showed an alignment trend with the filaments, whereas in a DM-only simulation with a semi-analytic model, the trend almost vanishes. Malavasi et al. (2021) use IllustrisTNG simulation to relate galaxy properties to distances to filaments and nodes. They only find a correlation with mass and star-formation rates, but no clear relation signal for angular momentum. In addition, Birnboim & Dekel (2003) find in hydrodynamical simulations that no virial shocks develop for gas falling into less massive halos and halos at $z > 2$. This means, that the gas reaches the disk where it fuels star formation. After a galaxy is quenched, further growth in stellar population is dominated by accretion. Oser et al. (2010) demonstrate with cosmological simulations, that stellar mass growth in galaxies happens in two phases. In their overview in Figure 1.4 over the origins of stars found in the galaxies at $z = 0$, a clear bimodal distribution emerges with stars either forming within 10% R_{vir} or are accreted from beyond the virial radius. In agreement with the results by Birnboim & Dekel (2003), the large bulk of stars have been formed before $z = 2$, while smaller galaxies tend to continue star-formation, albeit at a lower rate.

It has proven to be difficult to find unambiguous signals of angular momentum in observational data to support the picture of galaxies wandering from voids to walls, then to filaments and eventually to nodes. In this work, I want to add pieces to the puzzle of the pathway that galaxies take along their formation history by describing the evolutionary steps of their intrinsic stellar kinematics. Understanding how the angular momentum vector flips under what conditions can help with interpreting the alignment of galaxies with their surroundings.

First, the numerical foundation will be outlined in chapter 2, by describing the simulation, structure finder and limits to the data set. After that, chapter 3 will give a basic overview of the quantities studied in this work, before we have an explicit look into the evolution of several galaxies in chapter 4 to give a first impression of how the statistical data relates to the individual fates of the galaxies. The ensuing chapters 5 through 8 will discuss the impact of spin changes on the characteristics of the galaxies on a statistical level and we will see how mergers fit into the picture before the results are summarized in chapter 9.
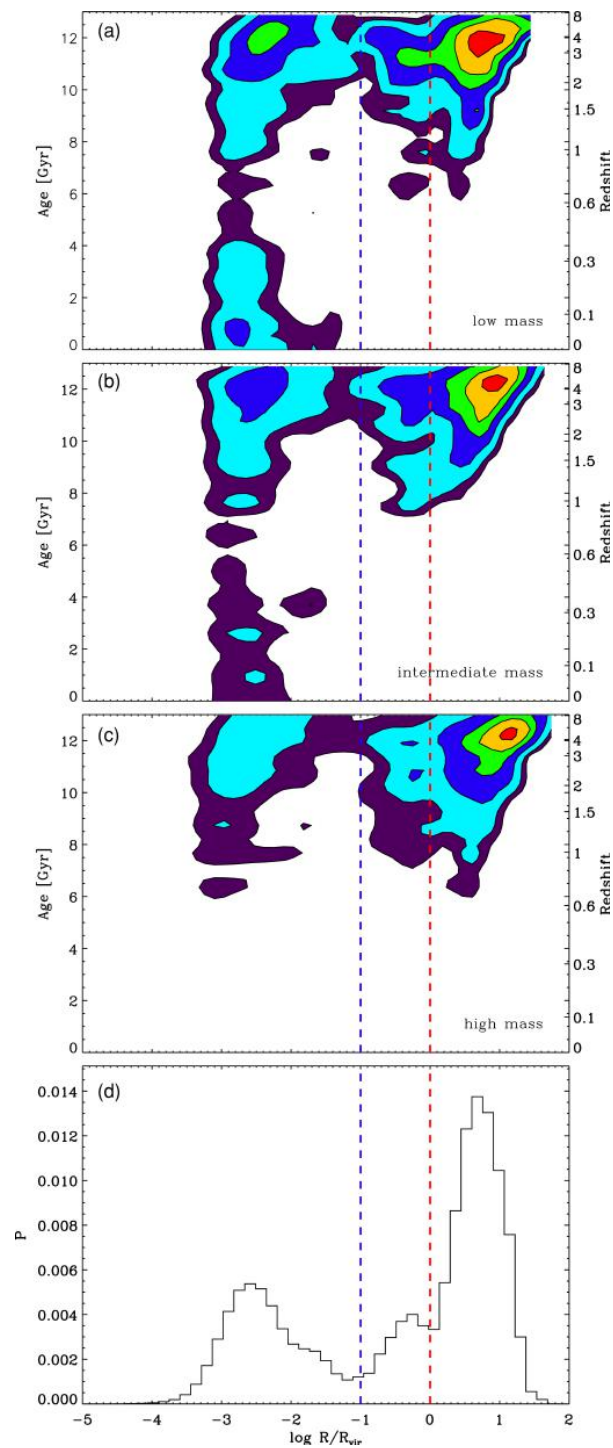
Figure 1.4: The two phases of galaxy formation by Oser et al. (2010). The heat map shows the origin of stars in the galaxies at $z = 0$. The highest densities are found in the top area corresponding to higher redshifts. Top to bottom sub-panels show bins of increasingly higher galaxy masses and an overall histogram.

Chapter 2

Simulation & Galaxy Tracking

In order to study the evolution of galaxies in simulations, different approaches can be taken. Apart from differences from prioritization when working around the limits of computational power, there are two fundamentally different approaches with different goals. One is to set up an idealized isolated scenario with well-controlled conditions and near-perfect information. This approach allows for a detailed study of specific cause-and-effect relations of scenarios, such as the importance of the exact kinematic set-up of a galaxy merger event for the production of different features. Thereby, an in-depth understanding can be achieved of how tidal arm, shells, rings or bars in galaxies are produced. The second approach are cosmological simulations. They allow us to study the greater picture, as they put galaxies in the context of their large-scale environment and epoch of the universe. This approach introduces more chaotic formation histories but can also inspire findings that were beyond the scope of our expectations. I took the approach of cosmological simulations of which the numerical and physical foundation is presented in this chapter.

2.1   The Magneticum Pathfinder Simulations

In the past decade, we have experienced a golden age of cosmological simulations with a full array of simulations with different strengths becoming available.

While simulations vary by their numerical method, a unifying measure of quality is provided by their mass resolution, number of particles and volume. Figure 2.1 shows an overview of several large cosmological simulations in a figure compiled by Kimmig (2022). The figure also differentiates between stellar and gas mass resolution, pointing out a major difference of mass resolutions for the two components in the case of the Magneticum simulations. Since

one gas particle can spawn up to four stellar particles, the average stellar mass is one fourth the mass of gas particles.
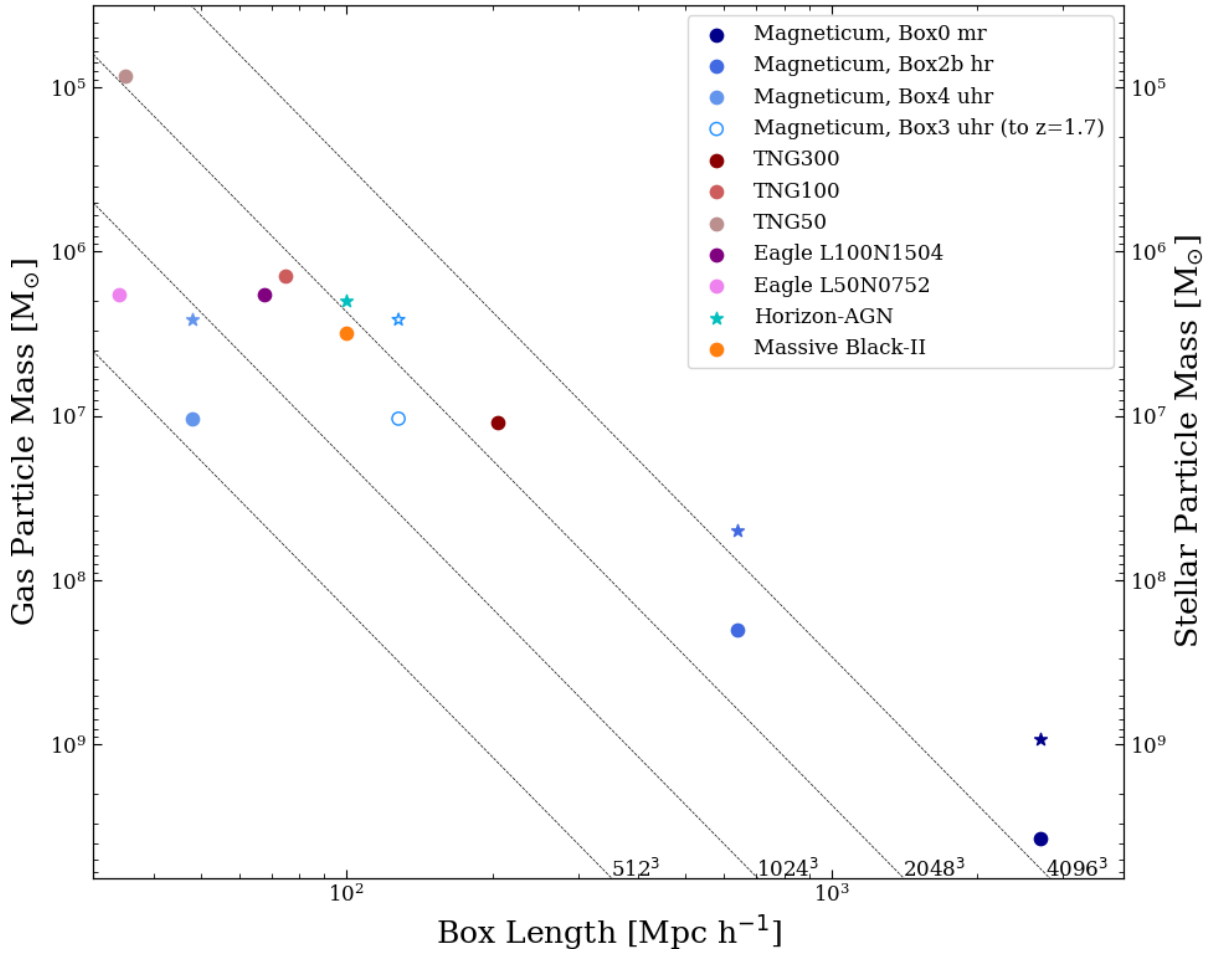
Figure 2.1: Comparison of cosmological simulations by their mass resolution and volume: Magneticum Pathfinder (Dolag, 2016b), IllustrisTNG (Nelson et al., 2018), EAGLE (Schaye et al., 2015), Horizon-AGN (Dubois et al., 2014) and MassiveBlack-II (Khandai et al., 2015). The volumes are compared by their comoving cube box lengths. The mass resolution is provided two-fold by the particle masses of gas and stars. Its mass axis is inverted to sort higher resolutions towards the top of the figure. Also, the number of particles can be inferred from the diagonal contour lines. (Courtesy of Kimmig (2022))

In this work, I have used the data from the hydrodynamical cosmological simulation Magneticum box 4 *uhr* (ultra-high resolution). Box 4 *uhr* has the highest mass resolution among the Magneticum simulations that completed their run until $z \approx 0$. Its stellar mass resolution is crucial to the analysis of galactic kinematics, since lower resolutions mean fewer particles and less reliable estimates of the galactic kinematics. The size of the simulation box is still large enough to host hundreds of thousands subhalos representing galaxies and satellites. A detailed description of the numerical code is found in the work by Hirschmann et al. (2014),

but the key aspects are summarized in the following section. The underlying cosmology follows the ΛCDM model using the WMAP7 results as described by Komatsu et al. (2011). The key parameters are summarized in their table 1 with $h = 0.704$, $\sigma_8 = 0.809$, $\Omega_\Lambda = 0.728$ and the primordial power spectrum index $n = 0.963$. The simulation was performed using the parallel cosmological TreePM-SPH code P-GADGET3, a variation of GADGET-3. It is an entropy-conserving formulation of SPH, which accounts for the problem of overcooling gas flows, that affect the thermal-energy version (Springel & Hernquist, 2002). The physics included in the simulations rely on the multi-phase model for star formation as described by Springel & Hernquist (2003). In this model, the ISM appears in two phases as cold and hot gas. The transition from hot to cold is achieved by cooling, whereas the hot phase is entered when gas particles surpass a density threshold. 10% of massive stars explode as Type II supernovae releasing an energy of 10^{51} erg that trigger galactic winds with $v_{wind} = 350$ km/s.

2.2 SUBFIND

The automatic identification of halos and subhalos or galaxies is performed using a variance of the SUBFIND algorithm (Dolag et al., 2009; Springel et al., 2001). A friend-of-friend (FoF) algorithm to identify parent halos. The condition for overdensity identification is defined by the linking length of $0.2 \cdot (\Delta_c / \Omega)^{-1/3} = 0.16$ times the mean dark matter (DM) particle separation. The factor is a modification of the standard linking length accounting for the cosmology. Then, the density for each particle in the FoF group is estimated, while only accepting halos that contain at least 32 DM particles. Each baryonic particle is associated with its nearest DM particle for the association with the group. Having defined the particles that belong to the group, density fields for each component are computed separately to avoid biases via a unified computation and added on top of each other to create a total density field. This defines the FoF group and the central subhalo at the same time. Then the main improvement of SUBFIND is applied: the identification of substructures in the halo by including stellar particles. As depicted in Figure 2.2, SUBFIND considers three neighbor particles to find saddle points. For a subhalo to be accepted, it must contain at least 20 stellar and/or DM particles, while gas is ignored for this condition.

Particles that lie just outside of a secondary subhalo are again associated with the central subhalo. As the focus of this work lies on the central galaxies, all particles that are not attributed to a secondary subhalo, are at first considered for the kinematic properties, which will be an important point that we come back to in section 2.4. Following the approach by Schulze
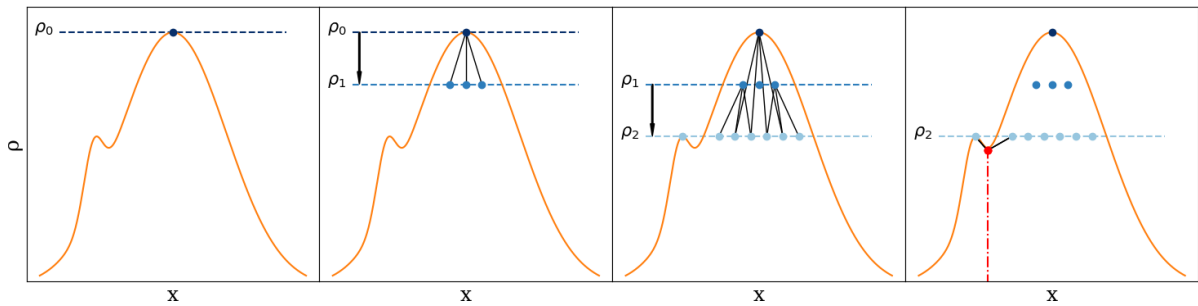
Figure 2.2: Schematic view of the updated SUBFIND algorithm (Dolag et al., 2009). The yellow line marks the density distribution derived from the particles (blue dots). The red dot in the right-most sub-panel marks a particle at the saddle point in the density field. Courtesy of Kimmig (2022).

et al. (2018), only subhalos with a sufficient mass resolution were considered by imposing a threshold of $M_* \geq 2 \cdot 10^{10}\,\mathrm{M}_\odot$ to be included.

This concludes the key aspects of SUBFIND for this work. For further details, I refer the reader to the work by Dolag et al. (2009).

2.3   Merger Trees

To study the evolution of halos through the simulation, the SUBFIND-identified galaxies must be traced through time. This process starts in the final snap shot at $z \approx 0$. The subhalos found here define the root galaxies from where we start to trace them back in time. To achieve this, a subhalo is linked to its progenitors by assessing which subhalos of the preceding snap shot contained the particles that are found in the current subhalo. In most cases, this is one progenitor. In some cases, multiple progenitors are found. The most massive progenitor is then considered as the main or "first" one. The others are considered as mergers, which again branch off to their own progenitors. A schematic depiction of this process is shown in Figure 2.3. It illustrates why the merger histories of the galaxies are called "trees". While the figure gives a more detailed explanation of how exactly the different subhalos at different times reference to each other in the code, the main principle is explained with the blue connection and lines. The figure also illustrates an example of how the merger tree organizes around the case when a subhalo is missing a progenitor in a snap shot, as it is not identified by SUBFIND. In this case, the mergers are attributed to the subhalo in the next snap shot.

As I looked into some galaxy pathways that showed jumpy properties, creating 3D-particle plots of these cases revealed inconsistencies. I noticed that in some cases an unexpected progenitor (e. g. much smaller, in volume and mass) was found. The "central switch" method was applied to fix this issue. It is based on the approach that I only use central subhalos
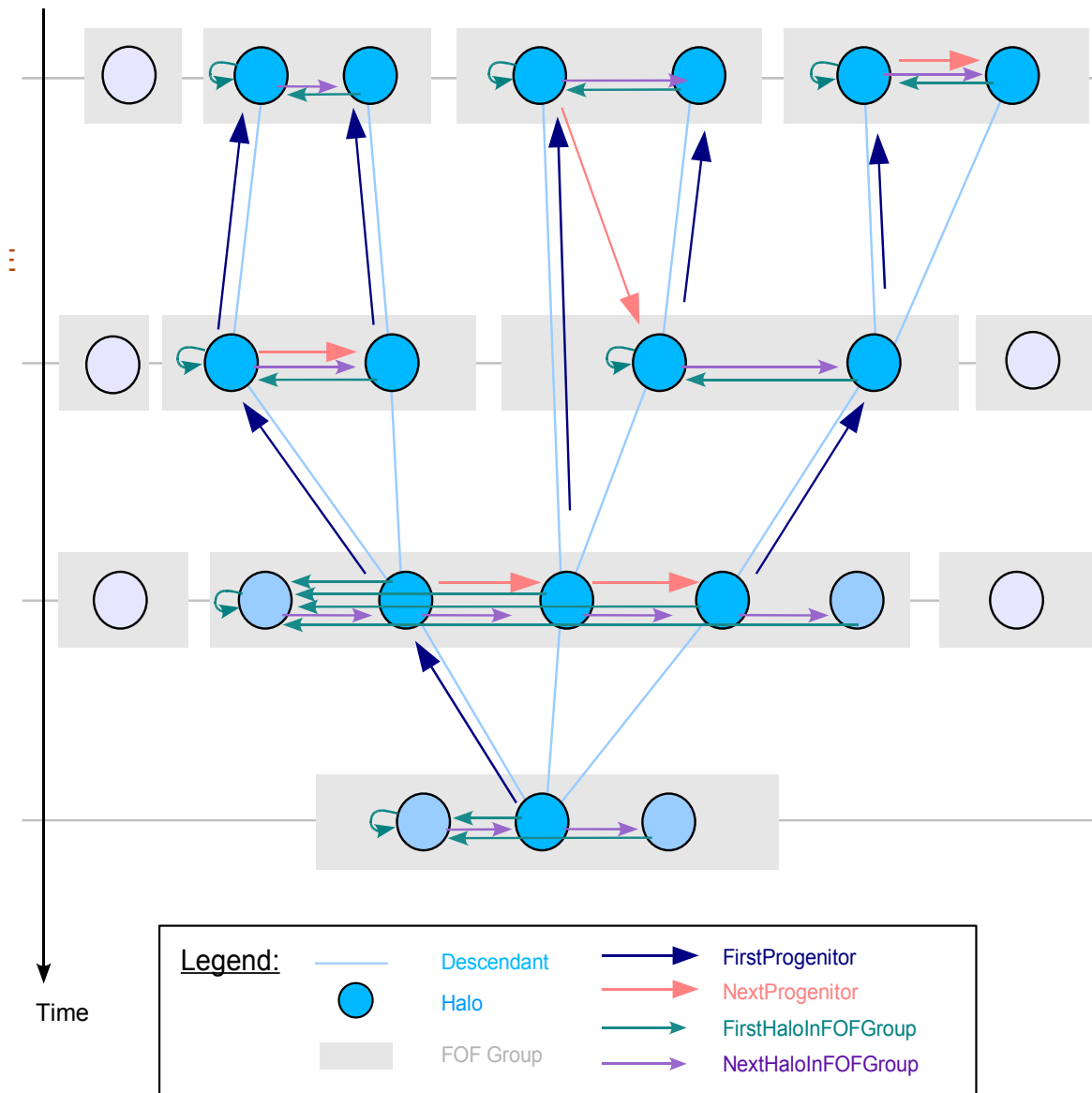
Figure 2.3: Schematic picture of the "merger trees". Each SUBFIND-identified halo in a snap shot is traced back to one or more progenitors in the previous snap shot (above), connected by light blue lines in this figure. While the most massive ("first") progenitor is tracked as the main galaxy (dark blue arrows), the smaller ("next") progenitors are registered as mergers. The grey boxes mark the galaxy ("friend-of-friend") group that is dominated by the left-most ("central") subhalo.

of a galaxy group for the analysis in this work. The underlying assumption is that a galaxy that dominates its group is expected to do so in the preceding snap shot. In other words, the progenitor must also be a central galaxy. If not, the progenitor assignment is considered incorrect and the central galaxy of a group containing the original progenitor assumes its place. In Figure 2.4 a modification of Figure 2.3 is shown with an example of a central switch.
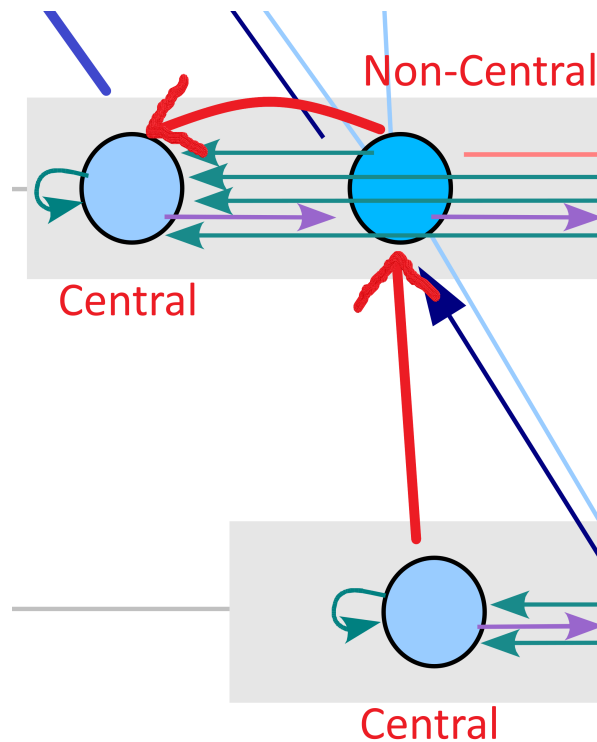
Figure 2.4: Alternation of Figure 2.3, to picture the scenario of central switches. The upward red arrow marks the path of a central to a non-central subhalo. The red arrow pointing to the left highlights the correction that ensues such a transition. These transitions are disregarded in the further analysis.

Since this is a very rough solution, that again introduces new problems and since no statistical evaluation on the success rates of the method were done, such transitions were excluded from the later analysis. With this trade-off, the method still allowed to trace galaxies until higher redshifts than before, as the path did not have to be interrupted.

One problem caused by this method is shown by cases in which different root galaxies trace back to the same central subhalo, which is physically impossible. These instances create duplicate tracks, which was fixed during the collection of all galaxy formation histories into one sample. Here, duplicates are identified unambiguously by the combination of the snap shot number and the SUBFIND ID assigned to a galaxy in a snap shot.

2.4   Fly-By Incidents

As I investigated on curious signals which showed the imprint of a short-lived spin change, I found the influence of a subhalo passing by the central galaxies on its kinematics. In an extreme case like this, it is clear that a significant amount of particles that share the same trajectory

as a subhalo are associated by SUBFIND with the cluster or central galaxy and dominate the intrinsic spin just for that moment. These events were sorted out, as the focus of this work lies on permanent spin changes. As can be seen in Figure 2.5, the problem is related to the difficult discussion of which particles to associate with a subhalo or the central galaxy.

(a) Face-on view   **(b)** Edge-on view
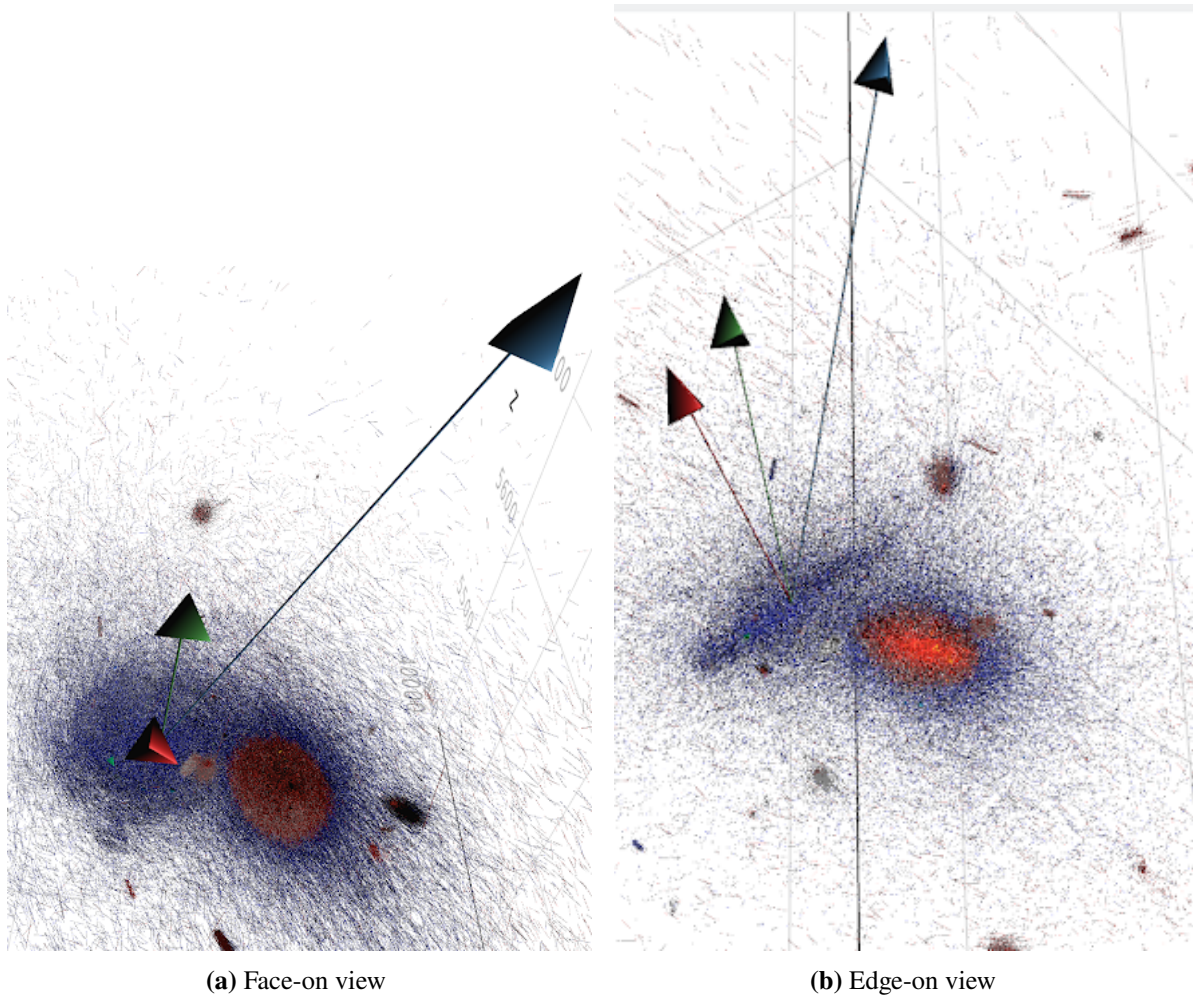
Figure 2.5: Galaxy experiencing a fly-by. Left and right show the same galaxy and moment in time from two different points of view. The figure shows only every 10th stellar particle for a more clear view of the situation. The blue particles are attributed to the main galaxy by SUBFIND and used for the spin calculation. The red particles represent stars of a different subhalo and are elevated to the front of the plot to make them visible as they are embedded in blue particles. Each particle appears elongated since they are expressed by vectors showing their velocity. While the global normalization is arbitrary, the lengths make comparisons between velocities possible. The three giant vectors express the specific angular momentum j_* at three consecutive moments in time as previous (red), current (blue) and next (green) snap shot.

To exclude these events as noise, the specific angular momentum j is compared at three consecutive moments in time. Then the spin change from the second transition $\Delta j_{23} := j_3 - j_2$

is compared to the vector difference $\Delta \boldsymbol{j}_{13} := \boldsymbol{j}_3 - \boldsymbol{j}_1$ between the last and the first snap shots. Both transitions are registered as part of the fly-by incident, when the third spin vector is more similar to the first one than to the second as $|\Delta \boldsymbol{j}_{13}| < |\Delta \boldsymbol{j}_{23}|$.

To put it in a nutshell, three conditions have been imposed for a time step to be included in the analysis. First, the galaxy must surpass the stellar mass threshold of $M_{\text{thr}} = 2 \cdot 10^{10} M_{\odot}$ at the start and end point of a transition. Second, the transition must have have happened without a central switch. And as a third condition, the transition must have been free of fly-by incidents. Applying these restrictions reduces the noise level of the data. There is also a risk of losing signal transitions, but refining the transition sample rules will be left for future work. An overview over how large the impact was on the data set is provided in Table 2.1.

$N_{\text{tot}} = 17825$	Instant ($\Delta t \approx 0.3$ Gyr)	Long-term ($\Delta t \approx 1$ Gyr)
Start mass	782	1897
Central switch	122	330
Fly-by	2357	2302
Sum	3261	4529

Table 2.1: Number of transitions that were excluded from the final data set, either because the galaxy mass did not surpass the threshold at the beginning of the transition, a central switch was applied to that transition or a fly-by incident was registered. The two time step sizes label two data sets that consider instant and long-term transitions (see section 3.5). The numbers are provided hierarchically in this table, so that their cases do not overlap and the lower lines always only count incidents that were not considered by the conditions in the lines above.

Chapter 3

The Galaxy Sample

This thesis will largely focus on a statistical evaluation of a sample of galaxies across snapshots over the cosmological simulation. It is important to outline the structure, possibilities and limits of the sample in order to put the conclusions drawn in the later chapters into perspective. This overview of the sample as well as a description of the considered Galactic features is the goal of this chapter.

3.1   Sample Evolution

The initial selection of subhalos was determined by their stellar masses and environment at $z = 0$. Due to the mass cut and focus on central subhalos, the number of available galaxies is reduced to 10^2 to 10^3 in each snapshot as can be seen in Figure 3.1a. Especially the number of available galaxies at z > 2 drops below 10^2 for each snapshot. The transitional data (cyan line) appears shifted by one time step. In order to accept their transitions, the galaxies have to satisfy the mass condition in the current and prior snapshot, which lowers the numbers to each prior level. In addition to that, flips caused by fly-by events were also excluded (see section 2.4) since the angular momentum in these moments are obscured by the contribution of the passing galaxy and can therefore not be considered.

When considering different epochs of the universe, an interesting point is the peak of cosmic star formation at redshift $z \approx 2$, demarcating a global transition of galaxies from a star-forming state into a quenched state. Figure Figure 3.2 shows that this transition moment depends on the galaxy sample. While the full subhalo sample agrees perfectly with the total star formation, excluding less massive ones not only causes an overall decrease but also shifts the transition point to almost agreeing with the high-resolution box. The star-formation rate density (SFRD) of central galaxies with $M_* \geq 2 \cdot 10^{10}$ $M_\odot$ peaks at around $z \approx 2$ agreeing

(a) Number of subhalos

(b) Sum of sample stellar mass
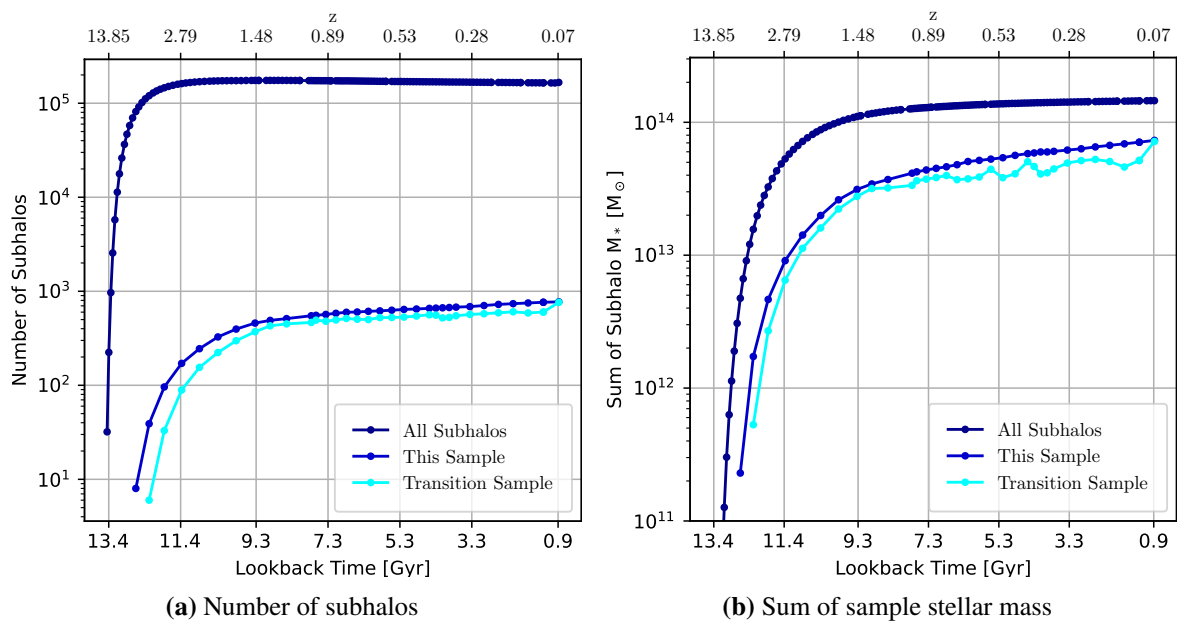
Figure 3.1: Evolution of sum of subhalos (left) and their masses (right) over time. Dark blue colors indicate sample of all SUBFIND-identified subhalos, medium blue represents the sample used in this work and cyan shows the transitional sample as described in section 2.4.

with observations as derived by Madau & Dickinson (2014). This encourages speculations on as to how the distribution relies on galaxy selection. However, a thorough comparison to observations is beyond the scope of this work. The agreement of the SFRD peak redshift in observations and the sample used in this work will be used to assume the observational peak at $z = 1.9$ for the further course of this work.

3.2   How is Mass Distributed?

Before looking at the distribution of mass, it is necessary to specify that the mass value used provided by SUBFIND. This is important to mention, since it is different from the mass included in the calculation of (specific) angular momenta. The latter is limited by the radial cut of $0.1 R_{\mathrm{vir}}$, while the former includes all stellar particles associated with the subhalo. The SUBFINDmass is chosen for consistency since it is also available for snapshots that do not provide particle data and therefore no angular momentum. This is crucial for the later calculation of merger ratios in chapter 7. Figure 3.3 compares the two mass values of the sample galaxies and also shows that most of the stellar mass is captured within the radius. From this figure I conclude that possible errors introduced from the difference can be neglected. The figure also suggests that disk galaxies cluster at the low-mass end and ellipticals dominate at higher masses. While this would agree with general expectations for the most massive objects
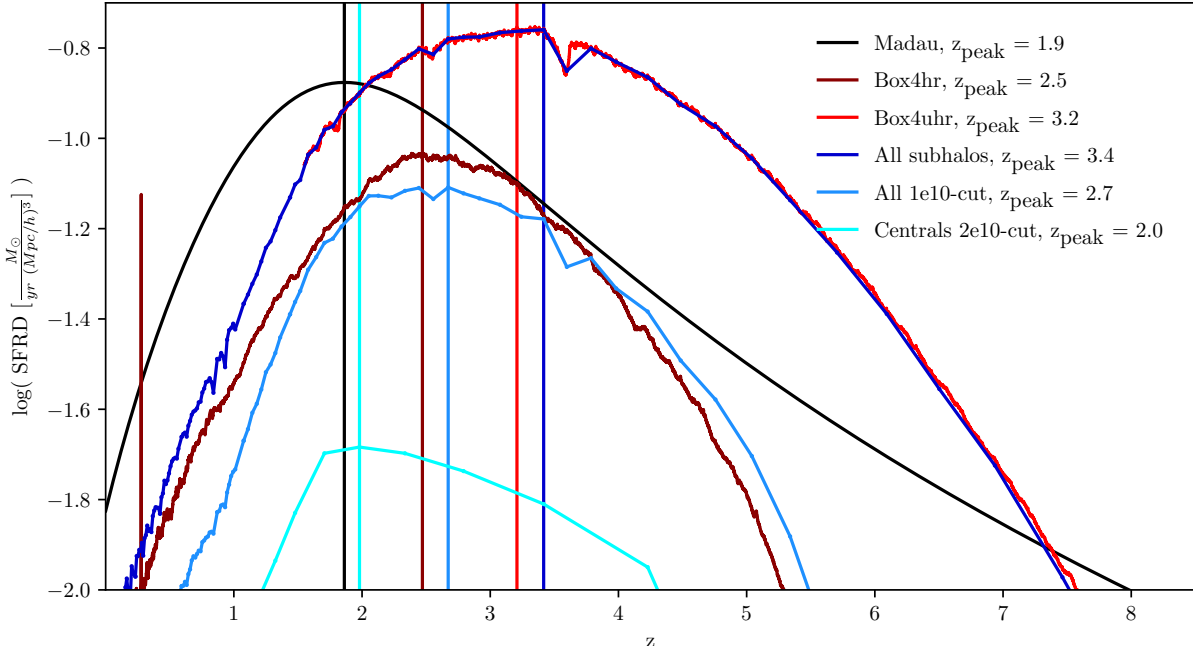
Figure 3.2: Star-formation rate density in comoving coordinates as a function of redshift. The black line depicts the best-fitting double power law by Madau & Dickinson (2014) found in observational data. The full star-formation as a direct simulation output is shown in red colors for the ultra-high resolution (bright) and high resolution (dark) boxes. The blue lines are found by summing up star-formation in sub-samples of SUBFIND-identified subhalos. Dark represents all subhalos, medium represents a selection satisfying $\log M_*/M_\odot \geq 10$ and cyan shows the values for subhalos considered in the further analysis of this work. The vertical lines highlight the respective peak values.

ending up as ellipticals, Figure 3.3 does not give that away, as disks are generally much less abundant and therefore may have a small chance of appearing among the comparatively few massive objects, which is shown in Figure 3.4. Figure 3.3 does show however, that higher-mass galaxies are less concentrated as the mass discrepancy rises to ~ 0.1 magnitudes. In addition to an overview of the subhalo masses involved in this sample, Figure 3.4 confirms that the dark matter component for our sample is generally larger by a magnitude. However, this picture is not as apparent for the mergers since their DM particles are likely associated with their central halo prior to the merger event due to the way SUBFINDattributes particles to subhalos. The small overlap of the central and merger mass distribution hints at the chance of major merger events compared to mini mergers. The plot also shows that the number of time steps is much larger than the number of mergers, which implies that most transitions over that time happen without any merger event.

In order to check for further biases in the sample, the stellar mass function can be viewed in Figure 3.5. The figure includes a comparison with previous work by Hirschmann et al. (2014). Two effects emerge: First, the overall density lies below the density measured by Hirschmann
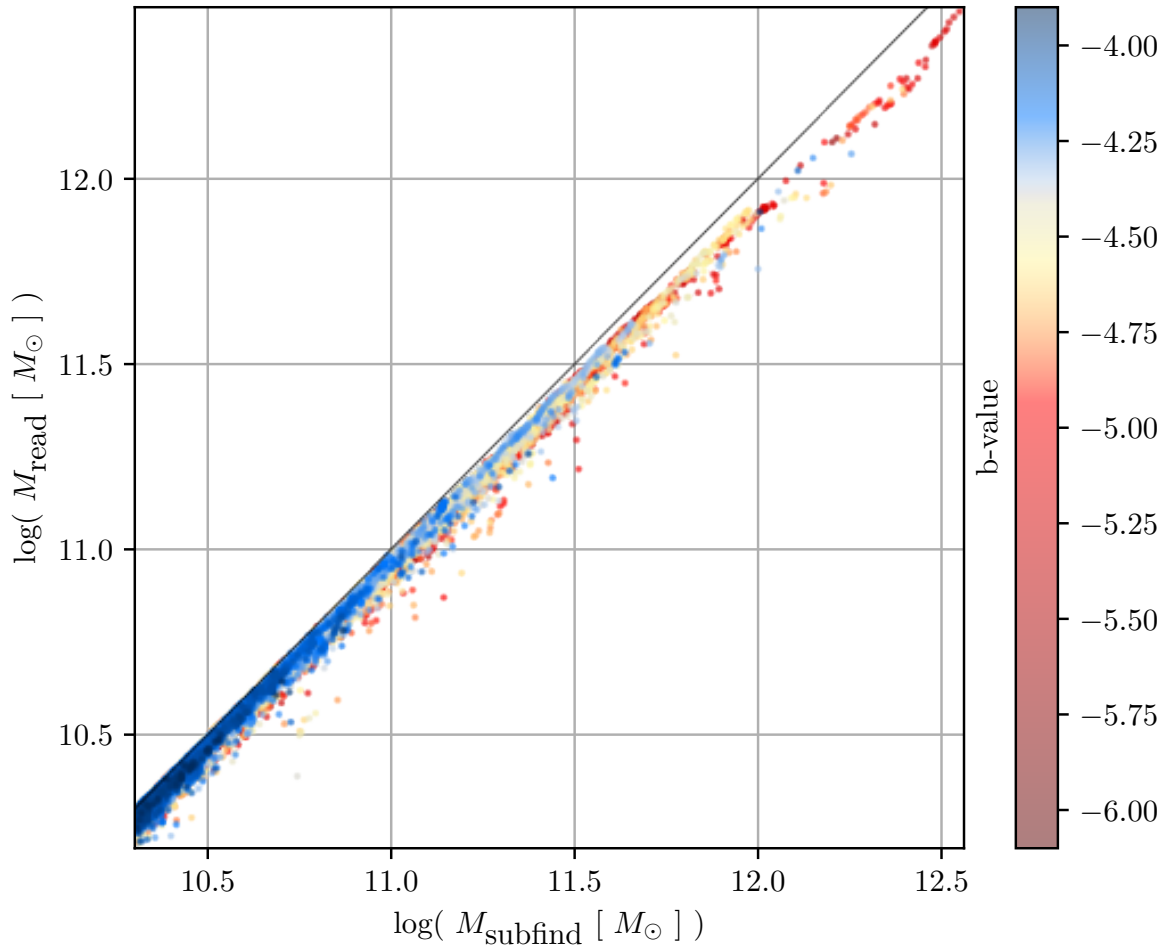
Figure 3.3: Subhalo stellar masses from particle readout for spin calculation against masses from SUBFIND. The color bar indicates the b-value. Since higher b-value points are in front, they are overrepresented in this figure.

et al. (2014), which is likely due to the limitation to central halos. Second, the evolution agrees in the steeper slopes and generally declining values over increasing redshift.

3.3   Galactic Spin

After the coverage of fundamental quantities in the previous sections, it is time to have a look at the data on the quantity in focus of this thesis: Angular momentum. The total angular momentum of a galaxy emerges from the sum of the particles' angular momenta with respect to their galactic center as

$$\boldsymbol{J} = \sum_k \left(\sum_{i \in N_k} m_{k,i} \boldsymbol{r}_{k,i} \times \boldsymbol{v}_{k,i} \right) \tag{3.1}$$
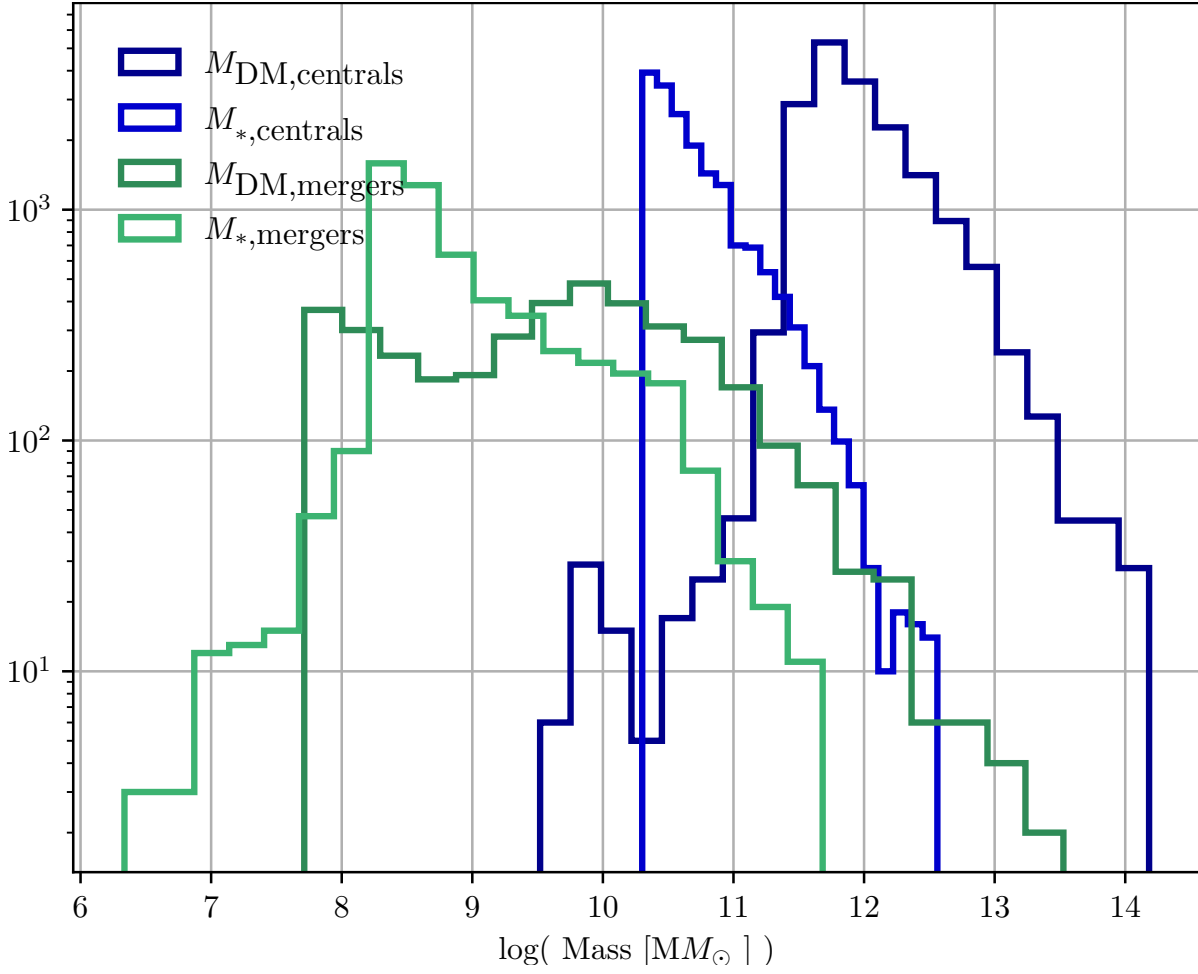
Figure 3.4: Dark matter and stellar mass distributions of central subhalos (blue) and mergers (green). The central halo mass cut becomes visible in medium-blue color.

with $k \in \{*, \text{gas}, \text{DM}\}$ iterating over the stellar, gas and dark matter component, consisting of N_k particles. Since this work focuses on the stellar component, $k = *$ is implied when not specified. In order to quantify the kinematic independently from the mass dependence of J, the specific angular momentum is introduced as

$$\boldsymbol{j_k} = \frac{\sum_{i \in N_k} m_{k,i} \boldsymbol{r}_{k,i} \times \boldsymbol{v}_{k,i}}{\sum_{i \in N_k} m_{k,i}} \tag{3.2}$$

or more simple when regarding only the magnitudes:

$$j_k = \frac{J_k}{M_k} \tag{3.3}$$

(a) This sample

(b) Sum of sample stellar mass
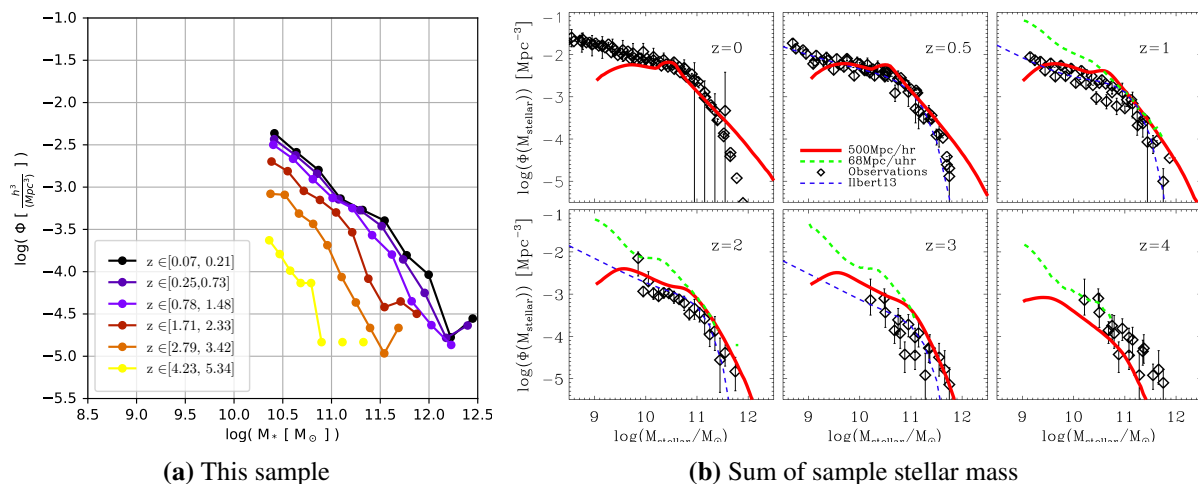
Figure 3.5: *Left:* Stellar mass function of the galaxies included in this work at different redshifts. The sample size for each redshift bin is $N_z \in \{3750,\ 8480,\ 4313,\ 968,\ 267,\ 47\}$. *Right:* For comparison to previous work by Hirschmann et al. (2014), snapshots have been grouped accordingly and divided by the number of snapshots in one group. The green dashed line represents the simulation used in this work. The red line represents a simulation with a greater box. A blue line and black data points show observational results.

Figure 3.6 provides a first glimpse at the distribution of angular momenta J and specific angular momenta j. In this figure, the distribution has already been split into disks, intermediates and disks according to their b-value. As expected, the distributions of ellipticals, intermediates and disks peak at increasing values of angular momenta. Also, the larger separation between the distributions from one plot to the other is expected by the definition of the b-value and the derived sub-samples. Consequently, the difference between galaxies of different morphological class is most apparent in Figure 3.6b. It is however interesting to see how close the populations are in Figure 3.6a, where total mass plays a role and ellipticals even dominate the regime of disks. This becomes important to the discussion of angular momentum changes with respect to their robustness.

It is to be noted that the spin calculation considers only stellar particles within 10% of the virial radius, as this corresponds to what is considered as the galaxy, where the bulk of the stellar population resides (Oser et al., 2010; Teklu et al., 2015). This assumption is explicitly tested and in Figure 3.7. The running median line mostly agrees well with the ideal line. Only towards larger spin values, where the scatter also becomes larger, an offset of about 0.5 to 1 orders of magnitude appears. The offset mostly appears for ellipticals that are expected to store larger amounts of angular momentum at large radii (Fall, 1983), a claim that is more clearly shown in Figure A.1 in the appendix.

(a) Angular momentum J

(b) Specific angular momentum j
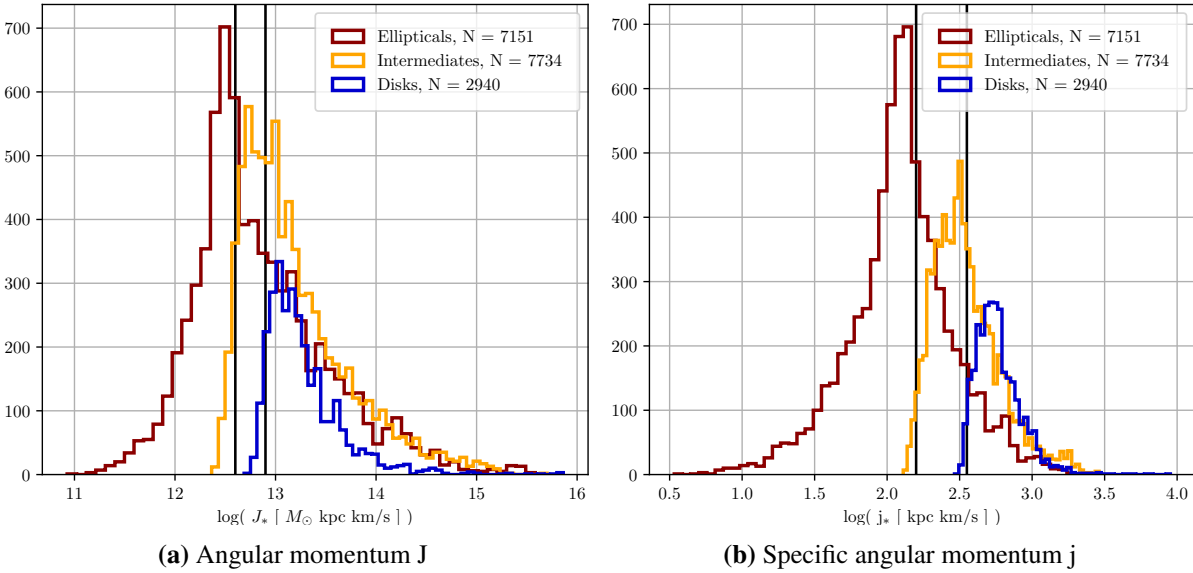
Figure 3.6: Histograms of angular momentum magnitudes of the full galaxy sample. The galaxies have been split into the classification scheme by their b-values.

To conclude the general picture on angular momentum, Figure 3.8a compares the M_*-j_*-plane of the sample at redshift 0 and 2. The first difference standing out is the scatter of the populations. At higher redshift, is not only the the range of j_* and M_* more concentrated around lower values, but also the scatter of the distribution is smaller as expressed by the 68th-percentile regions. The median values agree largely with a negligible offset to lower values for high-redshift galaxies. This contradicts expectations of decreasing spin with redshift, expressed by the offset between dashed and solid lines in Figure 3.8b. Following the argumentation in the other direction, it can be concluded that galaxies tend to be more disk-like at higher redshifts.

3.3.1 Morphology by b-value

In order to perform morphological classification, the b-value introduced by Teklu et al. (2015) provides a powerful tool that is simple in its application. Teklu et al. (2015) showed that it describes the overall intrinsic rotational support of a galaxy. Defined as

$$b = \log_{10}\left(\frac{j_*}{\text{kpc km/s}}\right) - \frac{2}{3}\log_{10}\left(\frac{M_*}{M_\odot}\right) \tag{3.4}$$

it appears as a linear function in the j_*-M_* plane. Interesting values are the separation between disks and intermediate galaxies at $b_0 = -4.357$ and between intermediates and ellipticals at $b_0 = -4.732$ as found by Mayer et al. (2022) and Kudritzki et al. (2021) respectively. Due to cosmological expansion, j_* changes for a given stellar mass as described by Obreschkow
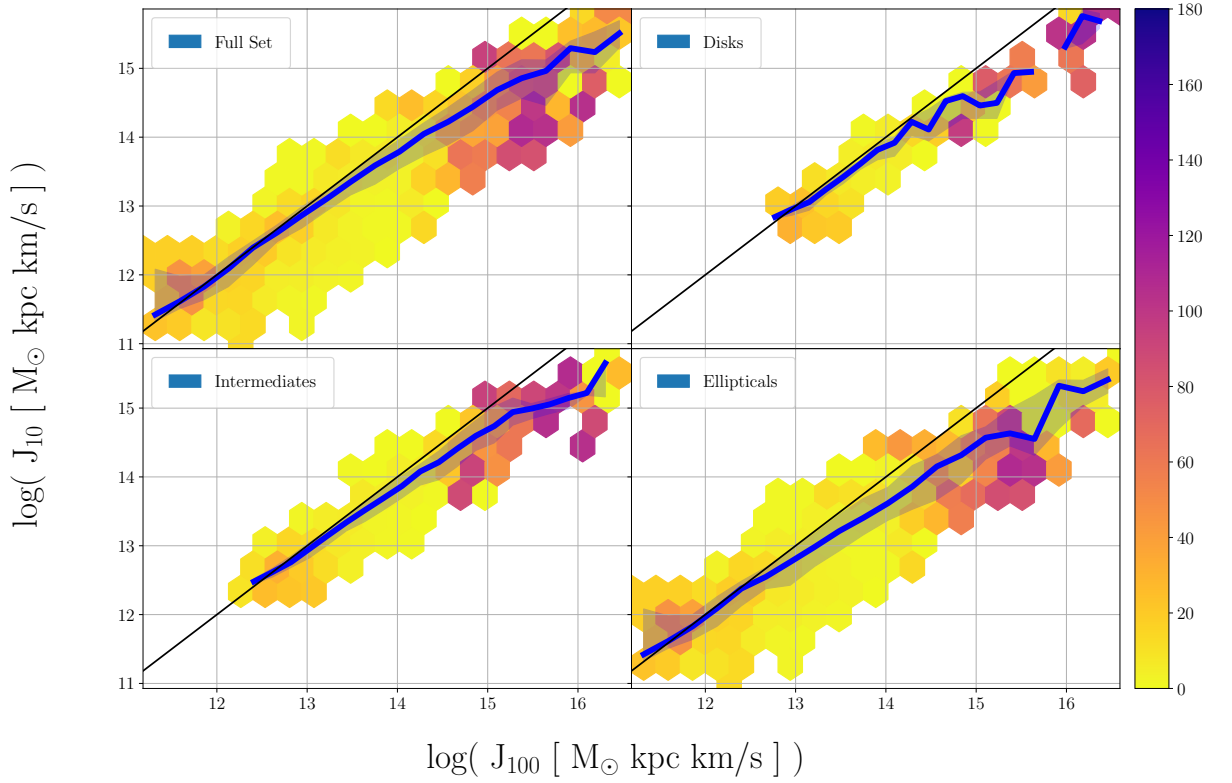
Figure 3.7: Stellar spin magnitude within 10% of the virial radius plotted against the value within the full viral radius. The colors represent the average alignment angle between the two quantities in a bin. The black line marks the theoretical perfect-agreement relation. The blue line and shade follow the running median and 68th-percentile area of the sample distribution. A version with colors according to the b-values is found in Figure A.1 in the appendix.

et al. (2015). This also affects the b-value and means that in order compare galaxy classes at different redshifts, we need to apply a correction factor to translate the b-value to $z = 0$ as

$$b_0 = b|_z + \frac{1}{2} \log_{10} (1 + z) \tag{3.5}$$

In order to make comparisons across redshifts possible, the adaption in Equation 3.5 will be applied whenever the b-value is referred to in this work.

To picture the classification by b-value, we can look at Figure 3.9. On the left-hand figure, the overall distribution is shown in a heat-map format summarizing the sample distribution for the full sample and in sub-samples at different redshifts. When comparing the low- and high-redshift panels it becomes even more evident than in Figure 3.8a that the high-redshift galaxies occupy the same region, but are more concentrated around the median. Figure 3.9b makes the link between the j_*-M_* plane and the color bar associated with the b-value classification. It

(a) This sample
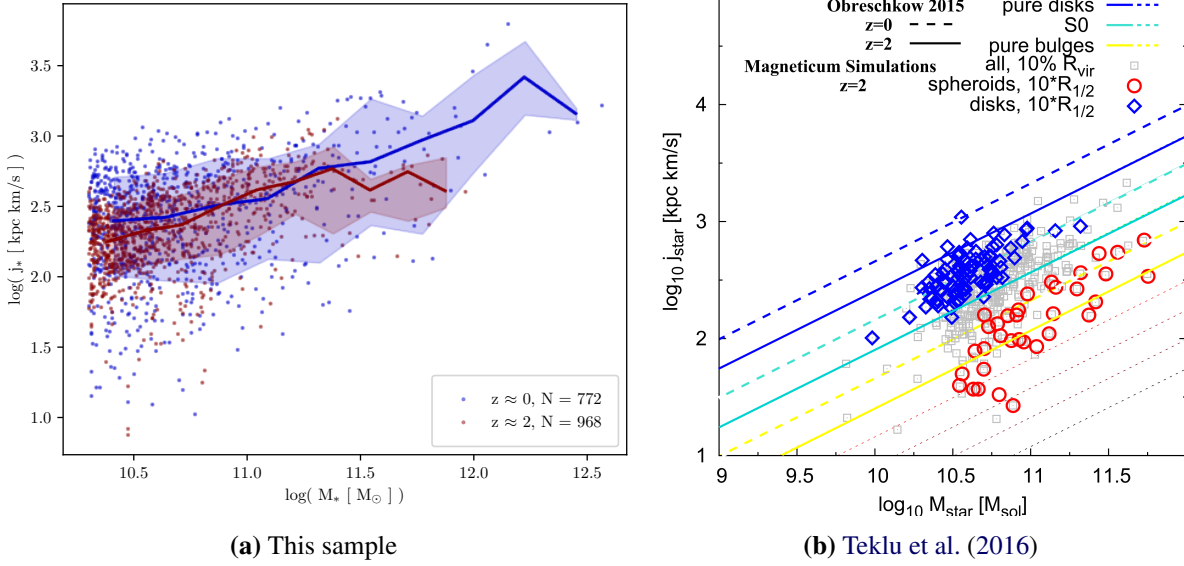
(b) Teklu et al. (2016)

Figure 3.8: Stellar specific angular momentum j_* against stellar mass M_* *Left:* Galaxies at $z \approx 0$ (blue) and $z \approx 2$ (red), the running median and the 68th percentile. *Right:* Reference plot by Teklu et al. (2016). Unlike Figure 3.8a, the MAGNETICUM galaxies are here divided by their kinematic morphology. The lines highlight the relations predicted by Obreschkow et al. (2015) for each morphological type at $z = 0$ (dashed) and $z = 2$ (solid).

marks the disks as blue, intermediate galaxies as yellow and ellipticals as red. Overall, one can see that the sample mostly clusters around intermediates and ellipticals.

(a) Bin Count
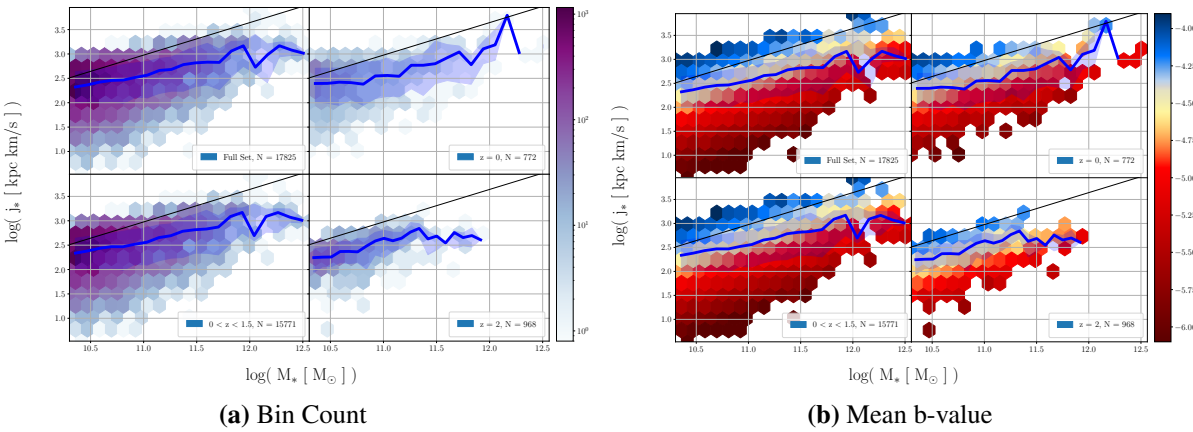
(b) Mean b-value

Figure 3.9: 2D histogram of the sample j_*-M_* plane. The colors represent the count in a bin on the left figure and the mean b-value of galaxies in a bin on the right figure. The black line marks the transition border from disks to intermediates and the blue line and shade traces the running median and 68th percentiles. Each figure is divided into four panels with sub-samples from top left to bottom right: full sample across all redshifts, galaxies at $z = 0$, galaxies within $0 < z < 1.5$, galaxies at $z = 2$.

3.4   Star Formation

This work focuses on kinematic features of galaxies. Star-formation is not directly a kinematic feature. However, since star-formation is strongly connected to morphology in observations and it is known to be triggered in events of kinematic disturbances such as mergers or accretion (Oser et al., 2010; Hwang et al., 2021), it is expected to show correlations with spin changes in the course of this work.

Figure 3.10 provides a general overview of the distribution of star formation rates in the sample of this work.

(a) Star-formation Rate   **(b)** Specific star-formation rate
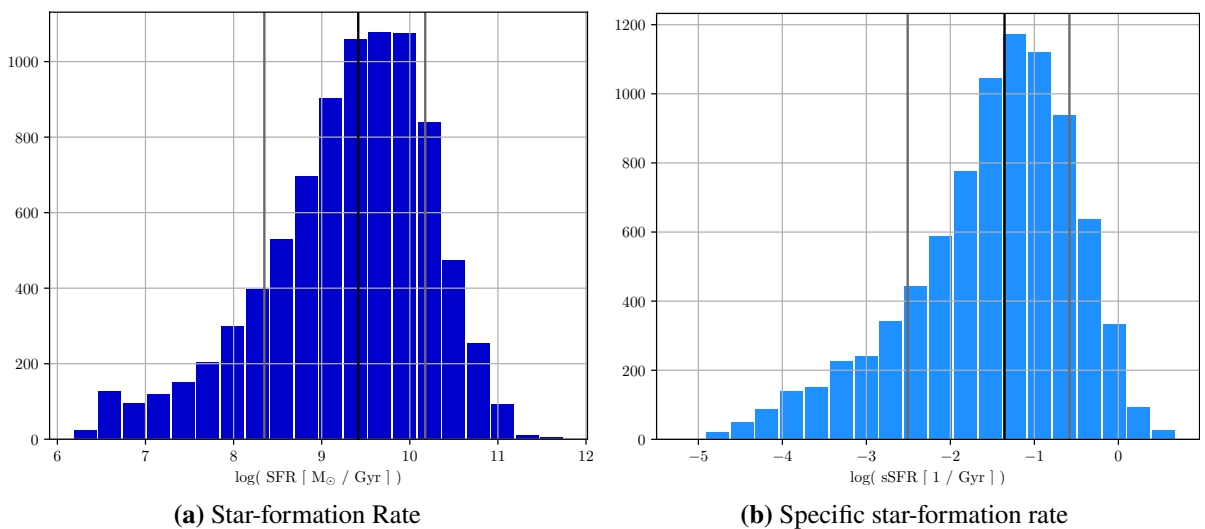
Figure 3.10: Distribution of the star-formation rate (left) and the specific star-formation rate (right) of the galaxies across all redshifts.

To characterize the sample further with respect to where stars are formed, Figure 3.11. It shows a trend for more massive galaxies to be generally less star-forming. The few super-massive galaxies with $M_* > 10^1 1.5 \ M_\odot$ lie above the trend around the peak (Figure 3.10b), which makes them significant for the global star formation despite their few numbers. It is important to note that many galaxies in the sample have zero values for star-formation rates and are therefore missing in the corresponding figures.

3.5   Transitions

After an overview over momentary values of the galaxy sample, this section will shed light on the evolution aspect of the the sample by displaying the transitions of galactic features over time steps. By its nature, it will serve as a transition into the analysis part of this work. Generally,
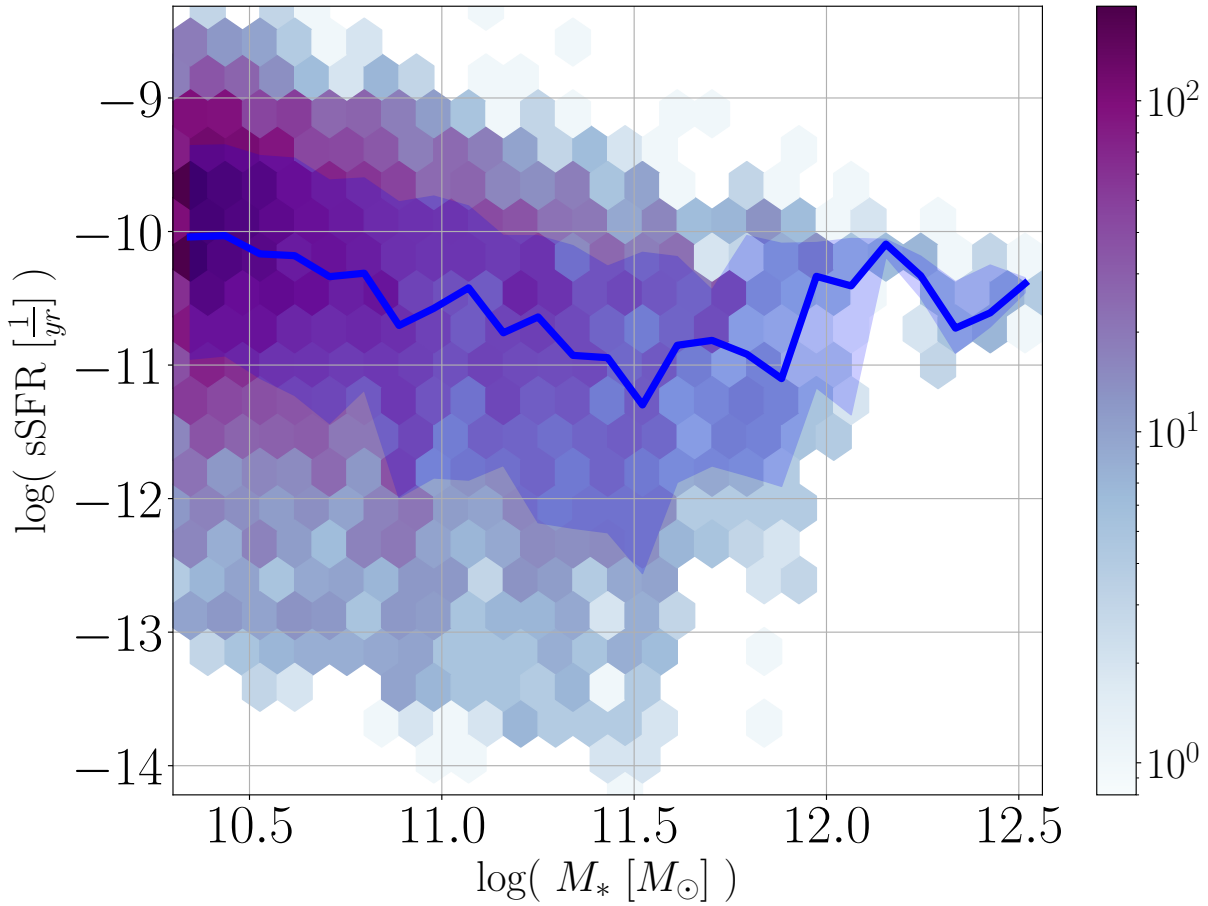
Figure 3.11: Heat map of specific star-formation rates against stellar mass. The blue line and shadow trace the running median and 68th percentiles.

data is available for instant transitions ($\Delta t \approx 0.3$ Gyr) and long-term transitions ($\Delta t \approx 1$ Gyr). Figure 3.12 shows the range of time step sizes. The large range is a result of multiple effects. First, snapshots of the simulation with particle data are available with varying time step sizes. Second, even in those snapshots, there can be problems calculating angular momenta in some cases. These two effects mark the bottom line for temporal resolution and determine the green distribution in Figure 3.12. Third, when a minimum step size threshold is set, the first and second effects are added on top of that resulting in the range of 0.9 to 1.4 Gyr for the denoted as "1 Gyr".

3.5.1 Drastic Mass Changes?

As a fundamental quantity, the transitions of galaxy masses are first in focus in order to provide an overview of the range of mass changes that also impact the later discussed angular momentum. In Figure 3.13b, we can observe changes ranging from the resolution limit to
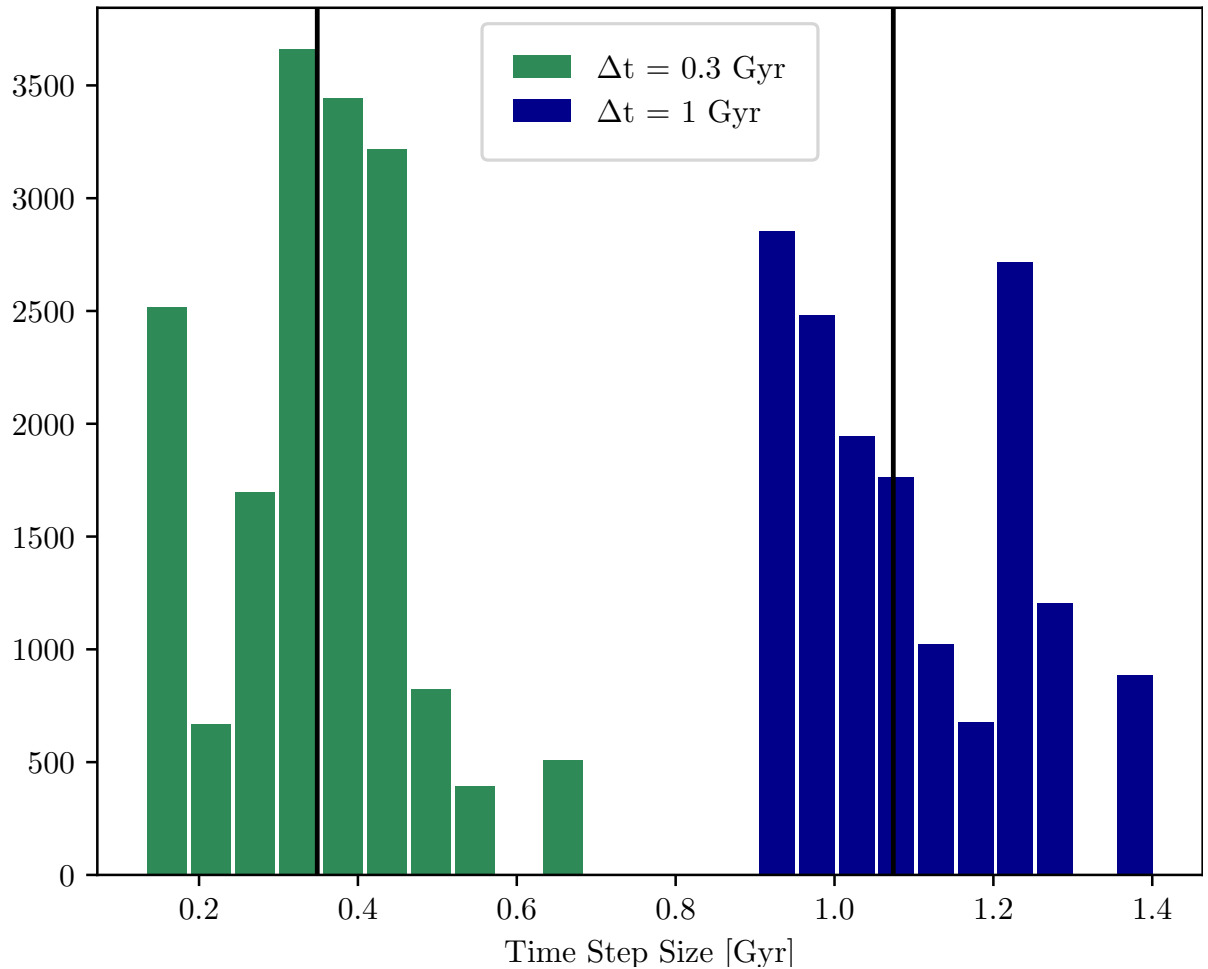
Figure 3.12: Time step size distribution of for the case of $\Delta t \approx 0.3$ Gyr (green) and $\Delta t \approx 1$ Gyr (blue). The green distribution has no minimum set size defined. The blue distribution comes with a requirement of $\Delta t \geq 0.9$ Gyr.

even beyond the initial subhalo mass. The scatter between the two extremes is largest for small galaxies and while large galaxies are expected to be more stable, small changes appear exclusive to small galaxies. In addition to mass data, the Figure 3.13 also links the spin flip angles to the transitional data and it becomes evident that larger flip angles are more common for larger mass differences and small subhalos. However, spin flips with mass changes magnitudes below subhalo masses do occur and ask for explanation beyond stellar mass accretion or formation. Figure 3.13a shows the same trend for mass loss. While with a much more clear offset from the black line, there are still some cases in which subhalos lose at least an order of magnitude over a time step, which pushes them down onto the black line.

The plots presented in Figure 3.14 are similarly structured. They compare the stellar mass differences with DM mass differences between time steps and also show the relation to

(a) Mass loss   **(b)** Mass gain
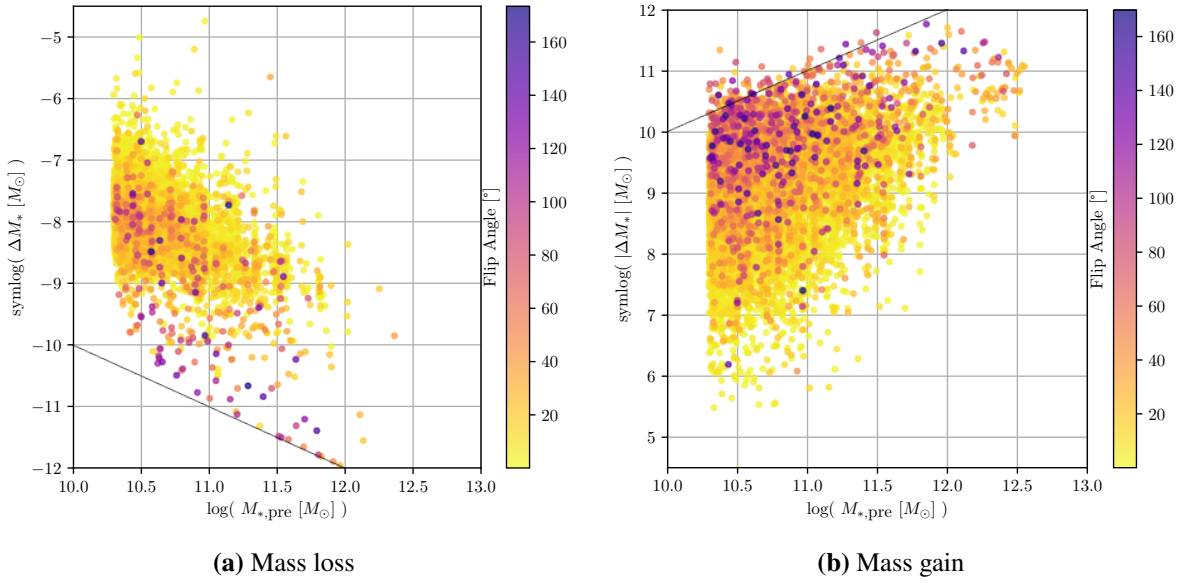
Figure 3.13: Stellar mass changes over the minimum time steps ($\Delta t \approx 0.3$ Gyr) against the galaxies' masses prior to the change. To express mass loss, the symmetric logarithm was used meaning that the left plot shows the same range of mass difference as the right plot with mass increases. The black line marks changes that are as large as the initial mass of a galaxy. The color is determined by the flip angle of the galactic spin vector with higher values in front for visibility, since they are less common.

the spin vector flip. Here, a correlation between the magnitudes of mass changes for both components can be observed. A closer look at Figure 3.14a shows that such a correlation mainly emerges from transitions coming with large spin spin flip angles. The small-flip sub-sample is presented with a much less constrained range of combinations for changes of both mass components, especially in the low-mass region but also beyond the subhalo mass threshold of $M_* \geq 2 \cdot 10^10 M_\odot$, i.e. a region possible major mass changes. While the scatter becomes large for small-flip transitions, the sample generally seems to cluster where the DM component undergoes mass changes one to two magnitudes greater than the stellar component, which matches expectations for the mass ratio of stellar and DM masses in galaxies. In an attempt to link the transitions to their halos, Figure 3.14b shows the relative mass changes on a logarithmic scale. The distribution remains similar while slightly compressed compared to Figure 3.14a and the offset from the reference line vanishes. While small-angle flips appear almost randomly scattered, large-angle flips mainly happen to galaxies that undergo mass changes of their magnitude down to one tenth of their initial mass. Below that, large spin flips still occur for mass changes down to 3 orders of magnitude while the relative DM mass change scatters around a constant value of -1.5 orders of magnitude.

(a) Absolute mass change   **(b)** Relative mass change
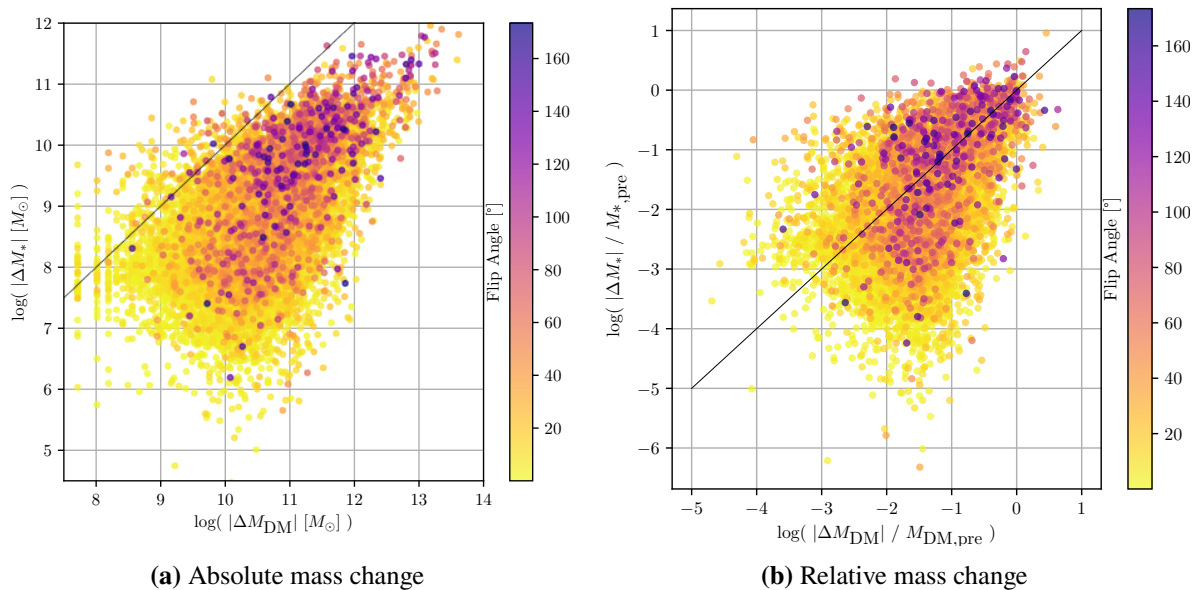
Figure 3.14: Stellar mass changes over the minimum time steps ($\Delta t \approx 0.3$ Gyr) against DM mass changes with absolute values (left) and relative values with respect to their masses prior to the time step (right). Mass loss and gain are not differentiated. The black reference line marks changes that are of the same size for both mass components. The color is determined by the flip angle of the galactic spin vector with higher values in front for visibility, since they are less common.

### 3.5.2   Spin Transitions

With this section we finally move to the main quantity of this work: angular momentum transitions defined as $\Delta \boldsymbol{J} \equiv \boldsymbol{J}_{t_2} - \boldsymbol{J}_{t_1}$ or $\Delta \boldsymbol{j} \equiv \boldsymbol{j}_{t_2} - \boldsymbol{j}_{t_1}$ by the difference of the spin vector measured at two subsequent snap shots. As angular momentum is added or removed from a subhalo, this event is expected to also change its morphology. This claim is investigated in Figure 3.15. The absolute spin transitions are distributed symmetrically around static b-values. Larger morphology changes come with larger spin changes, but most transitions have no impact on the morphology. The symmetry vanishes for relative spin changes, where we have to differentiate between transitions increasing or decreasing a galaxy's b-value. For static b-values ($\Delta b \approx 0$) the distribution concentrates strongly around small spin changes, but in absolute counts a large range of relative spin changes is covered. Transitions that make a galaxy more bulge-dominated converge to a relative spin change of 1. The trend for increasing b-values coming with larger spin changes than the initial spins, hints at that this region consists of ellipticals that are easily dominated by the spin that is transported via accretion or tidal interaction. These points above remain the same for long-term transitions, with the only difference lying in a slightly stronger scatter towards the borders of the distribution.

(a) $|\Delta J_*|$, $\Delta t \approx 0.3$ Gyr

(b) $|\Delta J_*|/|J_{*,\mathrm{pre}}|$, $\Delta t \approx 0.3$ Gyr

(c) $|\Delta J_*|$, $\Delta t \approx 1$ Gyr

(d) $|\Delta J_*|/|J_{*,\mathrm{pre}}|$, $\Delta t \approx 1$ Gyr
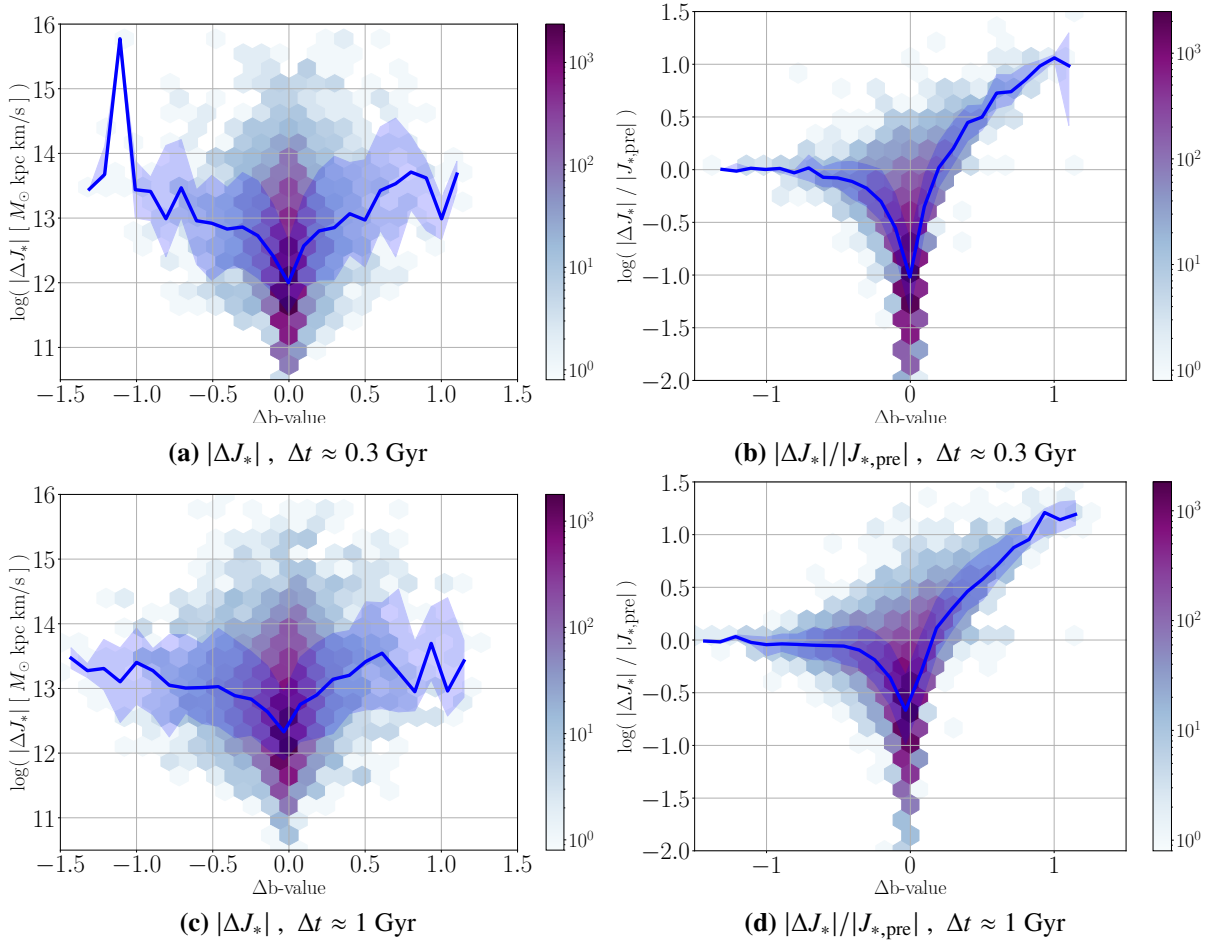
Figure 3.15: 2D-histogram of changes of angular momenta ΔJ_* [$M_\odot$ kpc km/s] against changes of their b-value. The blue lines and shades trace the running median and 68th percentile. The top row considers short-term transitions in contrast to long-term transitions in the bottom row. On the left, absolute values are taken, while on the right, values relative to the spin magnitudes prior to the time steps are shown.

Figure 3.16 links the specific kinematic change $|\Delta j_*|$ to mass accretion. What can be seen in all panels of the figure is a clear correlation between mass and specific spin change. In the case of mergers masses, the mass cut for what is considered a merger galaxy cuts off the distribution. However, even though the panels with mass differences have data there, the median spin change remains constant. Also, for the relation seen for merger masses, large mass values only impose a bottom-line limit on kinematic changes, while even for small merger masses, high kinematic changes are common. Just like in Figure 3.15, the difference between short- and long-term time steps is marginal with mass changes seeming slightly larger on average for the latter case.

As many of the plots above take into account the state of a galaxy before a transition, Figure 3.17 relates the morphological changes to the initial morphological states. Similar to Figure 3.15 small b-value changes are the most common case. However, an asymmetric trend
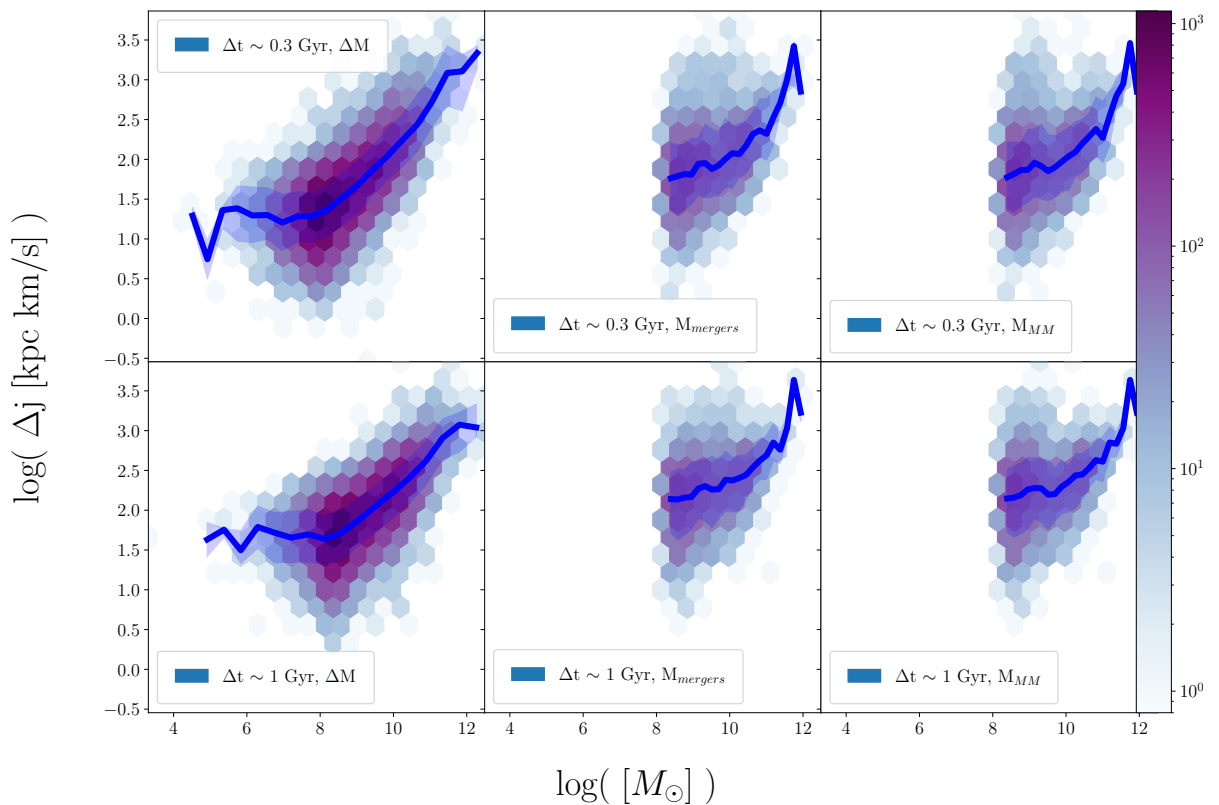
Figure 3.16: Change of specific angular momentum $|\Delta j_*|$ against mass accretion. The top row considers short time steps of $\Delta t \approx 0.3$ Gyr, while at the bottom $\Delta t \approx 1$ Gyr. Different mass types are considered from left to right: Total mass change ΔM_*, sum of stellar mass accreted through mergers, stellar mass of exclusively the largest merger.

can be seen for growing b-value changes. From the trend drawn by the running median I deduce that when rotational support is lost, it was likely suffered by a more disk-like galaxy than when gained. While the interpretation comes with the caveat that the scatter in the plot is very large as outlined by the 68th-percentile areas, the overall skewness of the distribution is clearly visible and agrees with the interpretation of Figure 3.15b and Figure 3.15d. The trend becomes slightly more constrained when regarding Figure 3.17b

3.5.3   What is a Spin Flip?

In addition to the magnitude of a spin vector, I looked a the orientation. For transitions, the spin flip angle ϕ_{flip} is defined as the orientation difference of a spin over a time step Δt. An overview of the distribution of ϕ_{flip} is presented in Figure 3.18. The use of the logarithmic scale emphasizes the clear favor of small spin flips for time step sizes considered, so viewing the spin orientation as a generally stable quantity is justified. The figure could serve as a hint at the amount of violent interactions such as major mergers, but it does not differentiate between
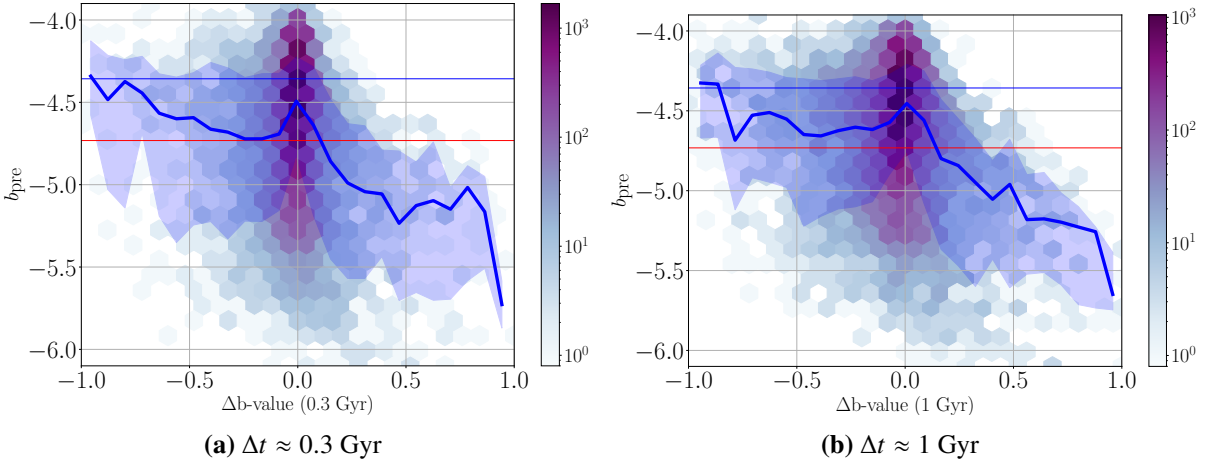
Figure 3.17: Morphological b-values plotted against b-value changes in a heat map for the two different time-step-size samples. The two straight lines mark the transitions points from disks to intermediates and from intermediates to ellipticals. The other blue line with its blue shadow trace the running median and 68th percentile of the distribution.

halos of different rotational support. For long-term flips the distribution flattens slightly as it moves towards the random distribution. A peak even appears at $\phi_{\text{flip}} \approx 7°$.
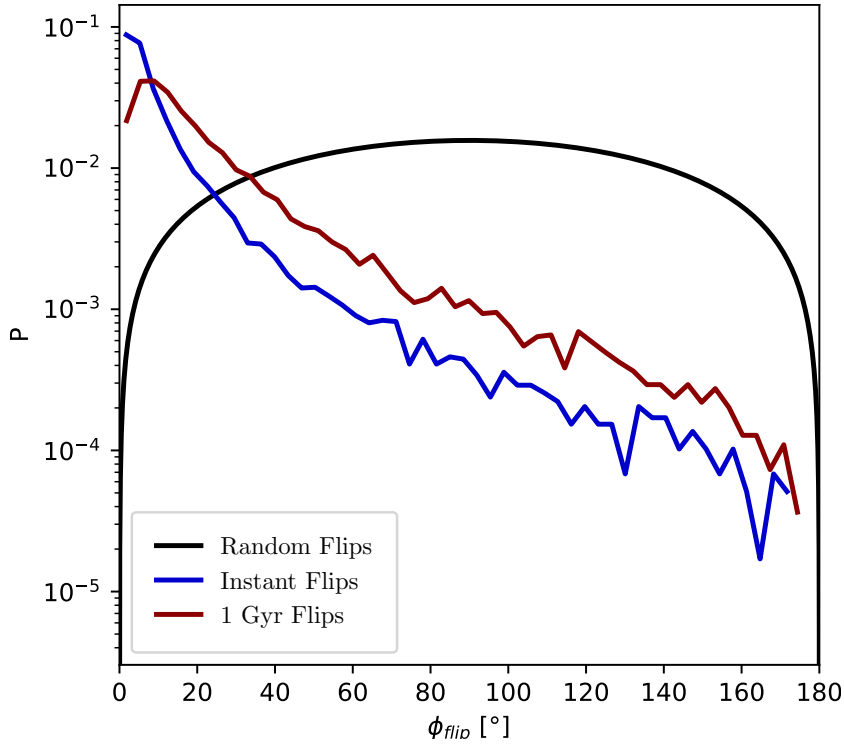
Figure 3.18: Density distribution of spin flip angles for $\Delta t \approx 0.3$ Gyr time steps (blue) and $\Delta t \approx 1$ Gyr time steps (red). A random distribution is drawn in black for reference.

Using ϕ_{flip} as an additional source of information, we revisit Figure 3.17 and the result is portrayed in Figure 3.19. As to be expected, larger flips come with larger values of $|\Delta b|$. Considering that the expectation value for random flips is 90°, flips can be considered random for $|\Delta b| > 0.4$ over 0.3-Gyr time steps and even for $|\Delta b| > 0.3$ for 1-Gyr time-steps. Now a clear picture is drawn for disks to be stable against small changes of their b-value and ellipticals undergoing larger flips even for small kinematic changes.

(a) $\Delta t \approx 0.3$ Gyr   **(b)** $\Delta t \approx 1$ Gyr
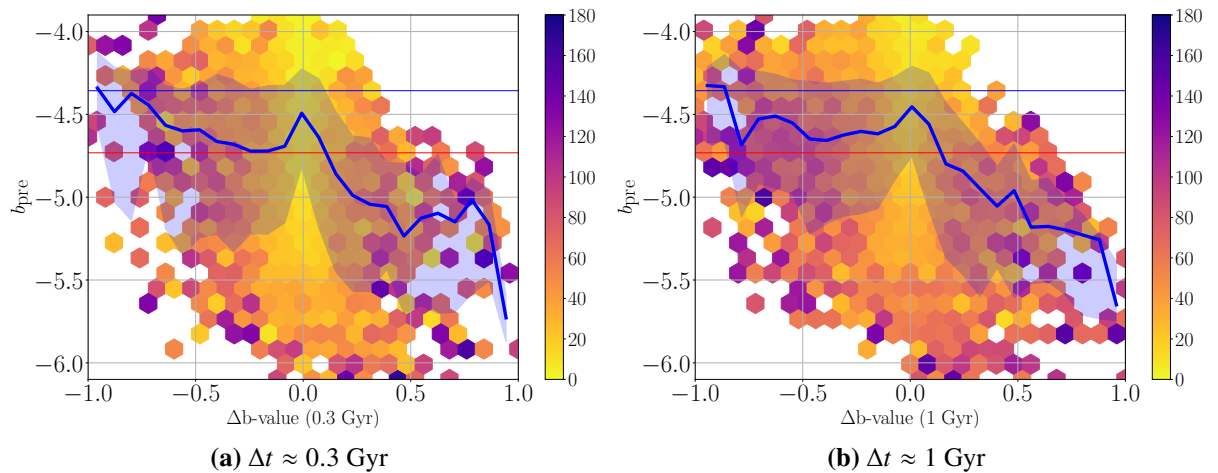
Figure 3.19: Morphological b-values plotted against b-value changes, as in Figure 3.17. The color in this figure is not count but the mean flip angle of data point in a bin. The two straight lines mark the transitions points from disks to intermediates and from intermediates to ellipticals. The other blue line with its blue shadow trace the running median and 68th percentile of the distribution.

Chapter 4

Halo Stories

Using SUBFIND and the merger trees (chapter 2), each galaxy can now be traced through time and we can now follow their full formation histories. In this chapter, a selection of these galaxy "halo stories" will be discussed in detail. By doing so, we can see explicitly what transition scenarios can look like and also get a sense of the effect of the selection criteria for transitions.

The first halo story shown in Figure 4.1 provided the example to identify a fly-by scenario. On the left side, we can see that the first transitions are disregarded as they do not meet the mass threshold requirement implemented as the vertical black line in the mass panel at the bottom. The two right-hand side transitions that were disregarded are the fly-by transitions shown in Figure 2.5. The first flag is for the transition from the red to blue spin vector and the second flag from blue to green. We can also see that the accretion of the merger with $M_* \approx 10^1 1 \, M_\odot$ is completed before the last snap shot, causing a lasting spin increase while the b-value remains constant. In contrast to that we can also see a true flip at a look-back time of $\Delta t_{\mathrm{lbt}} \approx 10$ Gyr. This spin flip is related to the major merger during that transition, which is an interesting point as it spins up the galaxy from an elliptical classification, close to an intermediate one. After that the galaxy experiences a continuous stream of very small mergers that must be aligned with the intrinsic angular momentum, as the spin and b-value increase continuously into the disk class without any major flip. The star-formation drops severely after the major merger, but then stabilizes and even increases, so this galaxy is never quenched and keeps converting gas inflow that likely come with the tiny mergers.

Figure 4.2 shows the halo story of one of the most massive galaxies in the simulation. Its highly turbulent environment with 909 subhalos in the cluster, causes the galaxy to undergo many spin flips and a highly fluctuating b-value and spin magnitude. As a result, many transitions are removed from the later analysis. Until $t_{\mathrm{lbt}} \approx 4.5$ Gyr, the star-formation rate stays stable until it drops by almost one order of magnitude after a larger merger event.
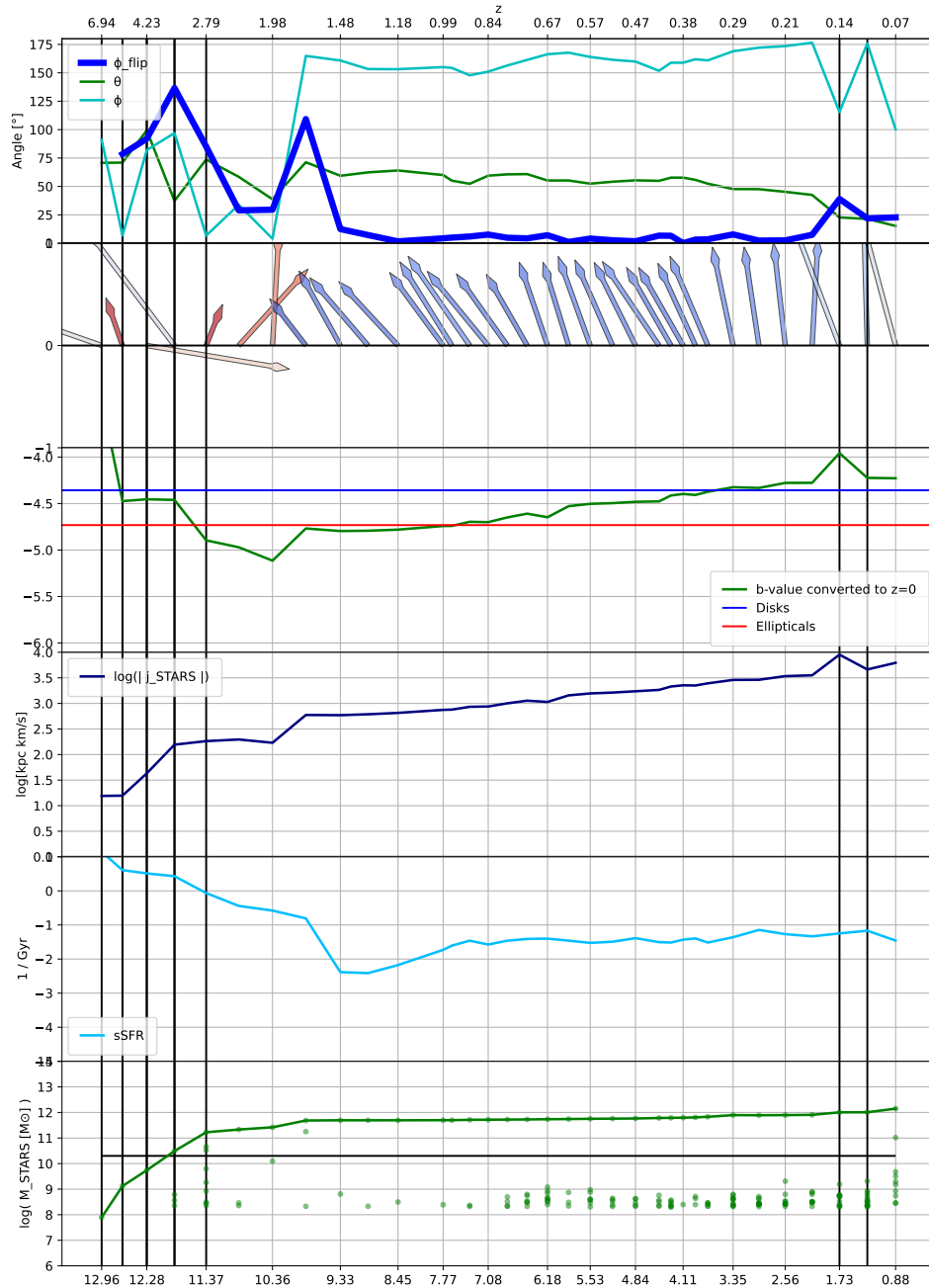
Figure 4.1: Evolution of the features of subhalo 3212. Vertical black lines mark the end points of transitions that were disregarded according to the rules summarized in section 2.4. The redshift and lookback time are indicated at the top and bottom of the figure. The top panel shows the flip angle (blue), and spherical coordinates with respect to the simulation box coordinate system. The second panel shows the spin orientation evolution over time with the color representing the orientation into (red) or out of (blue) the plane. The third panel shows the evolution of the b-value. The fourth, fifth and last panels show logarithmic values of the magnitude of j_*, sSFR and stellar mass. In the mass panel, the dots off the line are the mergers that fall into the galaxy during the transition to that snap shot.
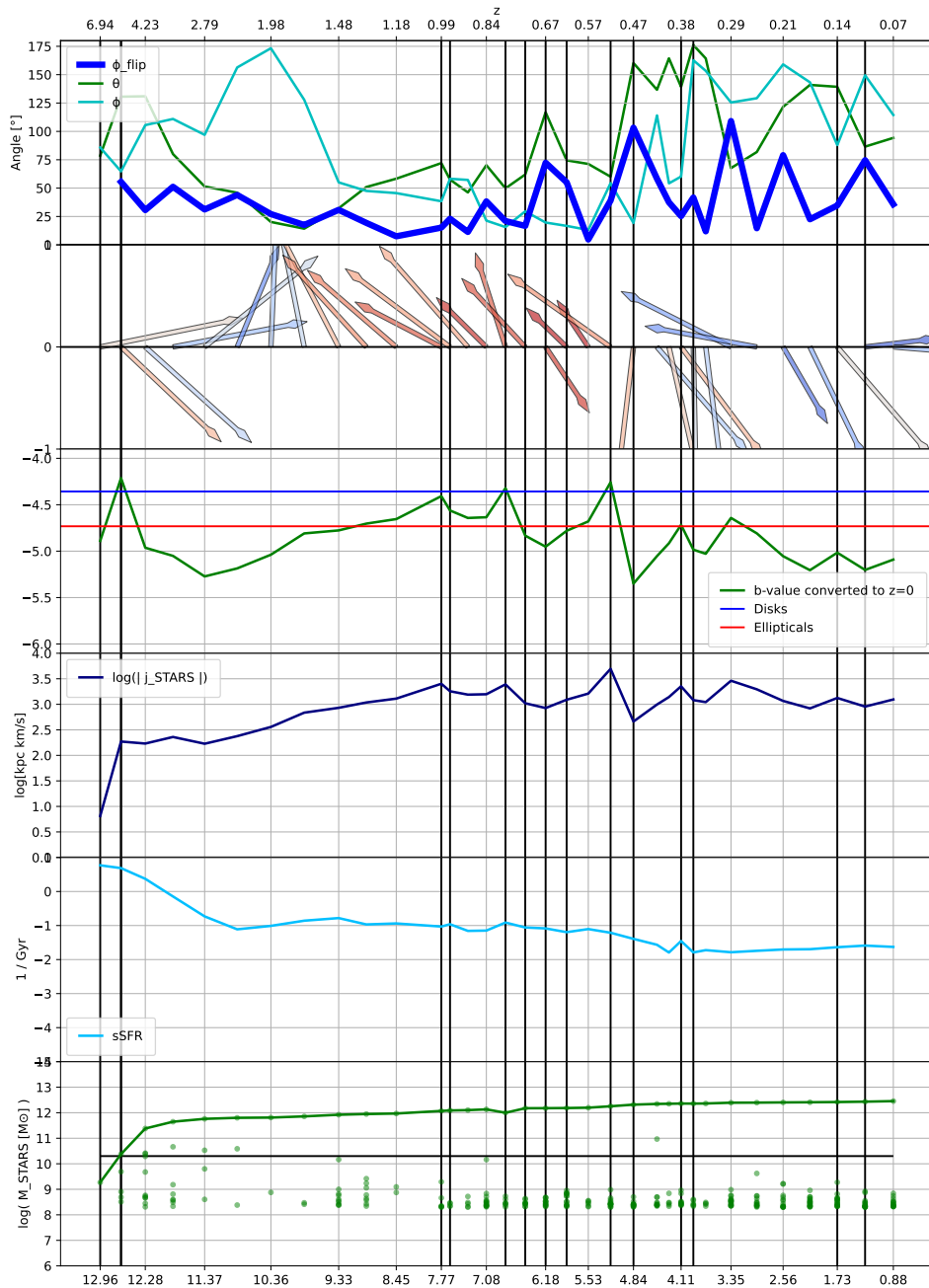
Figure 4.2: Evolution of the features of subhalo 1414. Vertical black lines mark the end points of transitions that were disregarded according to the rules summarized in section 2.4. The top panel shows the flip angle (blue), and spherical coordinates with respect to the simulation box coordinate system. The second panel shows the spin orientation evolution over time with the color representing the orientation into (red) or out of (blue) the plane. The third panel shows the evolution of the b-value. The fourth, fifth and last panels show logarithmic values of the magnitude of j_*, sSFR and stellar mass. In the mass panel, the dots off the line are the mergers that fall into the galaxy during the transition to that snap shot.

The next halo story in Figure 4.3 portrays a harsh contrast to Figure 4.2, as it shows a galaxy that just crosses the mass threshold and accretes only few tiny mergers. After $z \approx 1.3$, its star-formation rate quickly drops down to near zero. While its specific angular momentum remains constant over time, its b-value decreases at around $t_{\mathrm{lbt}} \approx 10$ Gyr due to its mass gain. A highly curious moment appears at $t_{\mathrm{lbt}} \approx 2.5$ Gyr. Here, the spin drops extremely and the mass also slightly decreases. This moment also has no central-switch event, which speaks against incorrect tracing. As this is a smaller galaxy, this event might hint at stripping and tidal disruption by a larger halo over ~ 400 Myr, but a numerical error appears as the more likely explanation.

During the analysis of this work, two different transition sets will be used. One measures transitions over time scales of 0.3 Gyr on average, while the other will compare states about 1 Gyr apart. The latter is used to capture signals as found in the halo story in Figure 4.4. At $t_{\mathrm{lbt}} \approx 4.84$ Gyr a larger merger is accreted, but the transition has no flip angle. This could mean that the merger collision is in alignment with the intrinsic angular momentum, but the flip by $30°$ at $t_{\mathrm{lbt}} \approx 5.5$ Gyr supports a picture that the merger process has been ongoing and the merger has transferred enough angular momentum through stripping prior to the merger event registration. Also, the other kinematic quantities j_* and b-value start to increase from $t_{\mathrm{lbt}} \approx 5.8$ Gyr on. In addition, the typical signature of a fly-by event appears right after the merger, with two consecutive flip by the same angle as the spin vector flips from one orientation to the other and back into the previous state. The star-formation is also increased with the turbulence and gas input from the merger and fly-by incident.

In the formation history of galaxies, the typical path is a disk galaxy that gets disturbed by a merger event turning its rotational support into velocity dispersion (Oser et al., 2010). The halo story in Figure 4.5 shows this with the infall of a large merger at $t_{\mathrm{lbt}} \approx 6.2$ Gyr. First, the spin vector flips followed by a decrease of star-formation rate, j_* and b-value as the halo gains stellar mass until the merger event is registered and the galaxy has transformed from a near-disk to a near-elliptical. Later at $t_{\mathrm{lbt}} \approx 2$ Gyr, the galaxy experiences another merger of a similar mass ratio. This event again starts with large losses of rotational support as the merger flips the spin by $125°$ in its first encounter of the merger. However, when the two galaxies are fully merged, the dominant orbital angular momentum of the merger spins up the adds enough rotational energy to bring the galaxy back to a kinematic disk state. This event is accompanied by an increase of star-formation, even though at a lower level than at high redshift, as the gas reservoirs are likely depleted at lower redshifts.

In this chapter, an overview of several interesting galaxy formation histories is presented. Depending on a galaxy's environment, the kinematic properties can remain constant or undergo large fluctuations. The figures show how the conditions eliminate transitions of unstable halos
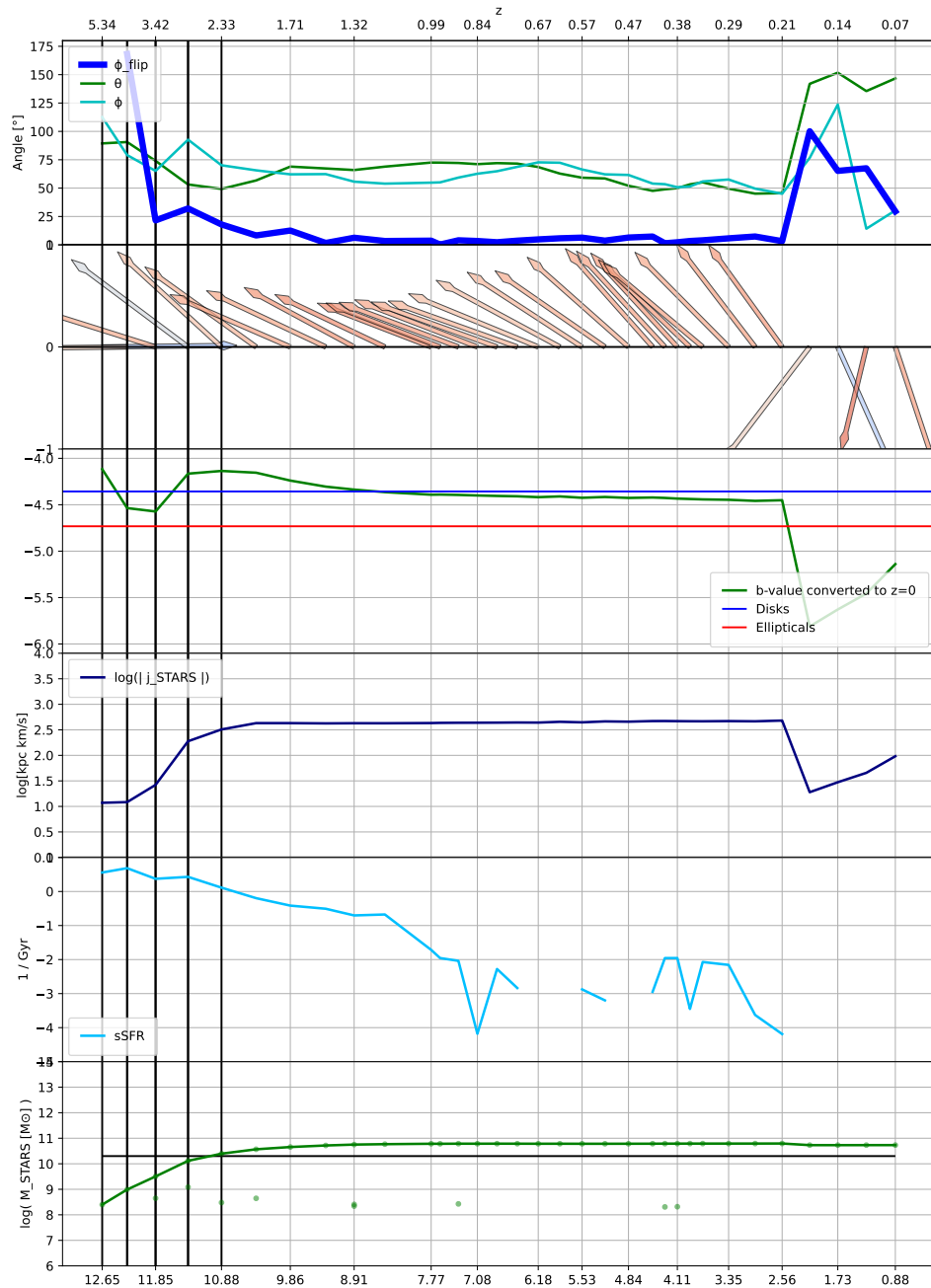
Figure 4.3: Evolution of the features of subhalo 14755. Vertical black lines mark the end points of transitions that were disregarded according to the rules summarized in section 2.4. The top panel shows the flip angle (blue), and spherical coordinates with respect to the simulation box coordinate system. The second panel shows the spin orientation evolution over time with the color representing the orientation into (red) or out of (blue) the plane. The third panel shows the evolution of the b-value. The fourth, fifth and last panels show logarithmic values of the magnitude of j_*, sSFR and stellar mass. In the mass panel, the dots off the line are the mergers that fall into the galaxy during the transition to that snap shot.
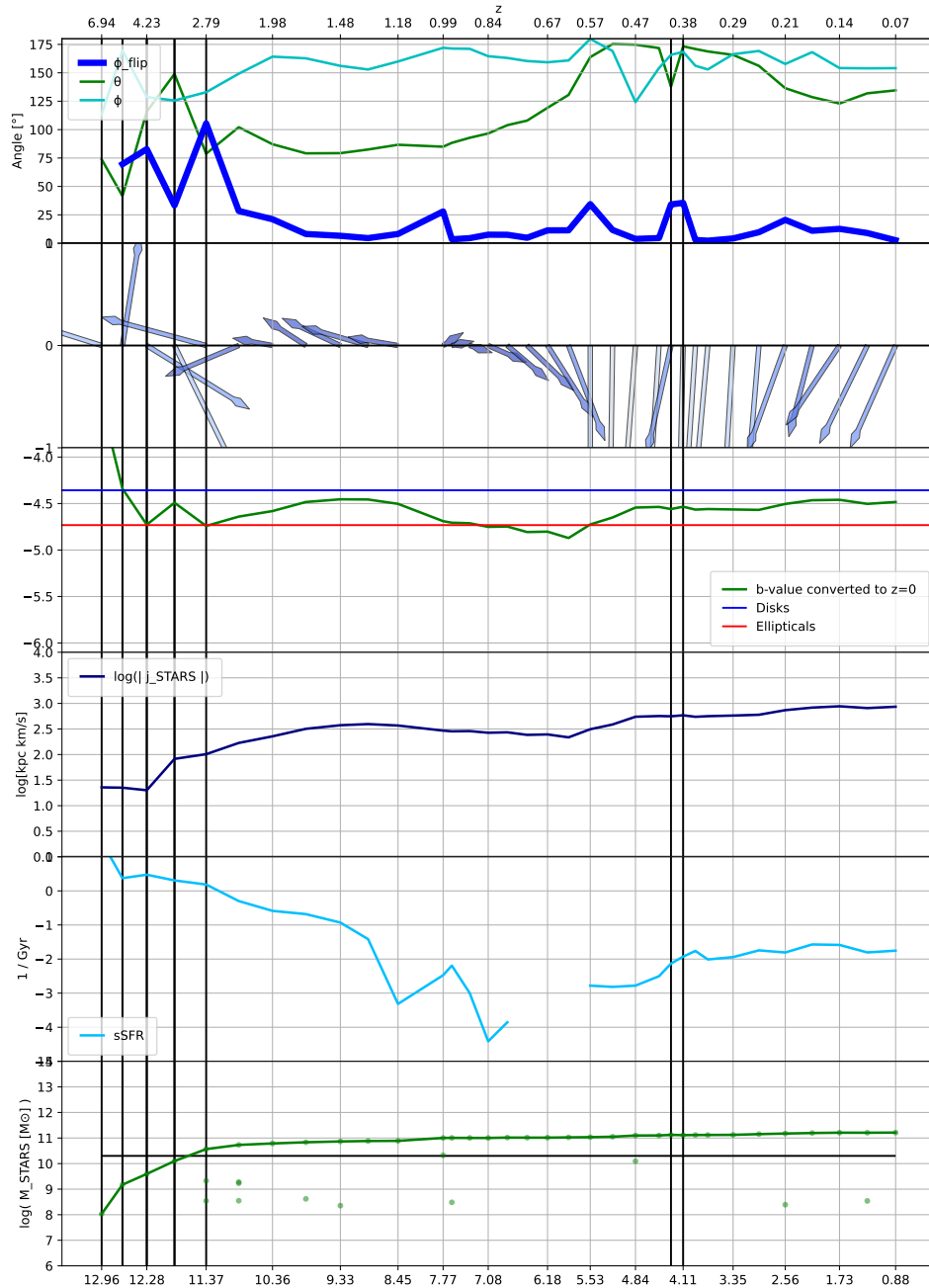
Figure 4.4: Evolution of the features of subhalo 11001. Vertical black lines mark the end points of transitions that were disregarded according to the rules summarized in section 2.4. The top panel shows the flip angle (blue), and spherical coordinates with respect to the simulation box coordinate system. The second panel shows the spin orientation evolution over time with the color representing the orientation into (red) or out of (blue) the plane. The third panel shows the evolution of the b-value. The fourth, fifth and last panels show logarithmic values of the magnitude of j_*, sSFR and stellar mass. In the mass panel, the dots off the line are the mergers that fall into the galaxy during the transition to that snap shot.
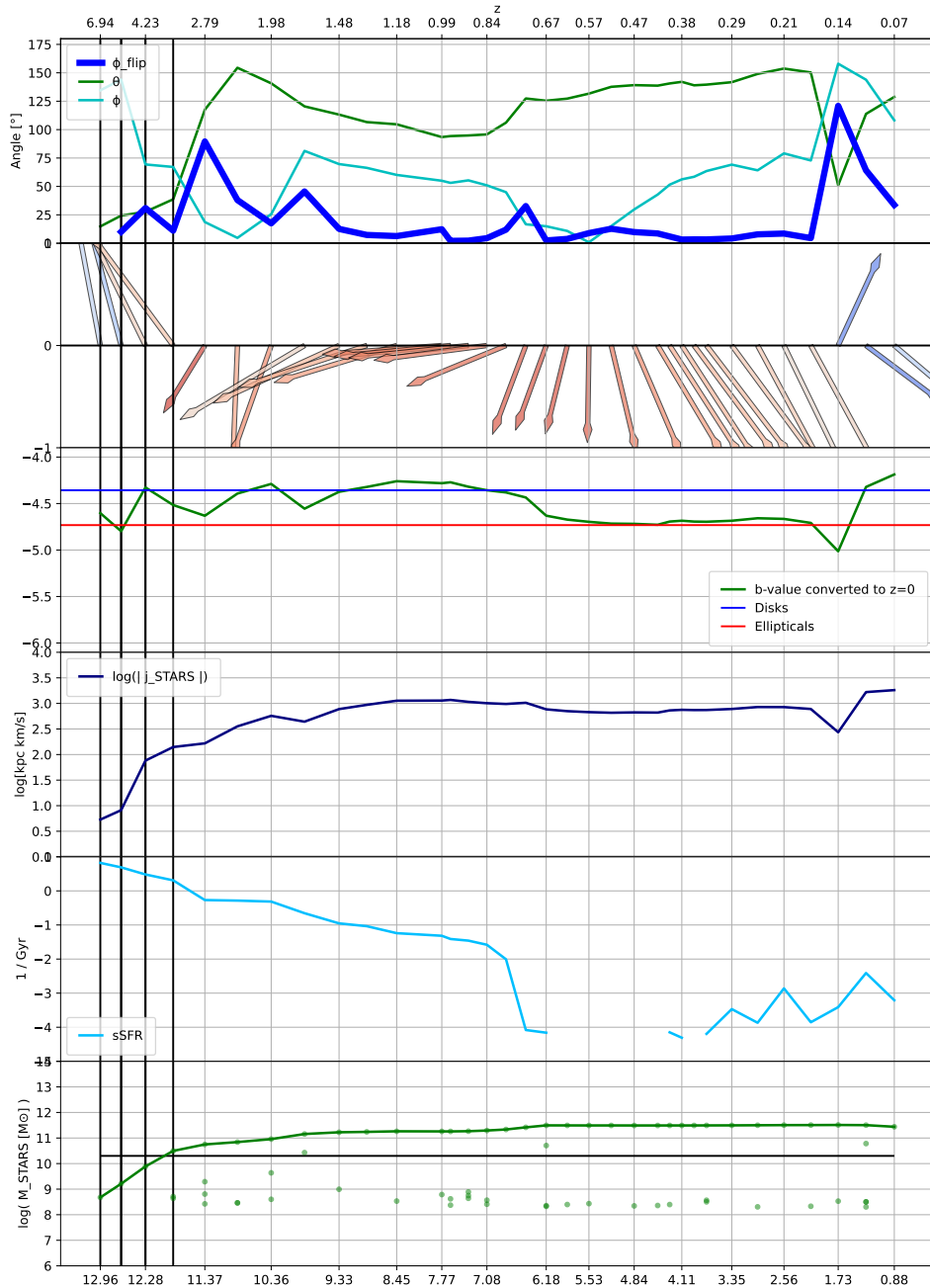
Figure 4.5: Evolution of the features of subhalo 12334. Vertical black lines mark the end points of transitions that were disregarded according to the rules summarized in section 2.4. The top panel shows the flip angle (blue), and spherical coordinates with respect to the simulation box coordinate system. The second panel shows the spin orientation evolution over time with the color representing the orientation into (red) or out of (blue) the plane. The third panel shows the evolution of the b-value. The fourth, fifth and last panels show logarithmic values of the magnitude of j_*, sSFR and stellar mass. In the mass panel, the dots off the line are the mergers that fall into the galaxy during the transition to that snap shot.

in turbulent environments. The help to differentiate between cases, not all odd behaviour is identified automatically and in addition wanted transitions can be wrongly flagged in specific set-ups. We can conclude that much more work is needed to refine the flagging system to distinguish between wanted and unwanted signals more reliably. Also, noise defined as chaotic environment in this work could be studied and the flagging system could be used to search for turbulent galaxy groups.

Chapter 5

Spin Transitions

Having outlined the general sample, it is a good time to discuss changes of the angular momentum in detail. How much does the spin change in which types of galaxies? How does it affect them? What are the limits with respect to the reorientation of each spin vector? What does the interplay between spin transitions initial angular momentum of a galaxy look like? If flips are due to events that change the kinematics, will that also show in star-formation spikes as a consequence of turbulence?

As thin-disk features are characterized by a dominant rotational support (Peebles, 1993), disk galaxies should experience few spin changes that have much impact on them. I expect any galaxy with a large angular momentum to be resilient against disturbances and flip angles to stay overall small for them. Only strong disturbance events, primarily through major mergers or close flyby encounters transferring a lot of orbital angular momentum to a large-spin galaxy should be able to cause large flips. On the other hand, mass contributes just as much to the angular momentum as particle velocities (Equation 3.1) and could therefore serve as a stabilizing factor that disks tend to miss.

These questions and assumptions will be tested in this chapter.

In the double-log plots of Figure 5.1, the spin transition magnitudes are related to the initial halo masses. If we look at the top row, we can see a clear linear relation across the range of two to two and a half magnitudes for mass, three to three and a half for ΔJ and less than two magnitudes for Δj. Evidently, more massive subhalos experience stronger spin transitions for J and for j. The steepness of that trend is different for J and j. If we consider the range of magnitudes covered for the three quantities at play, this is well explained by the mass dependence of J. In order to shed light on the mass-dependent stability, we can look at the bottom row plots of Figure 5.1. Here we find that the relative spin changes are almost constant across all masses with a slight mass trend. However, the distribution is almost the

(a) Angular momentum J

(b) Specific angular momentum j

(c) Relative angular momentum J

(d) Relative specific angular momentum j
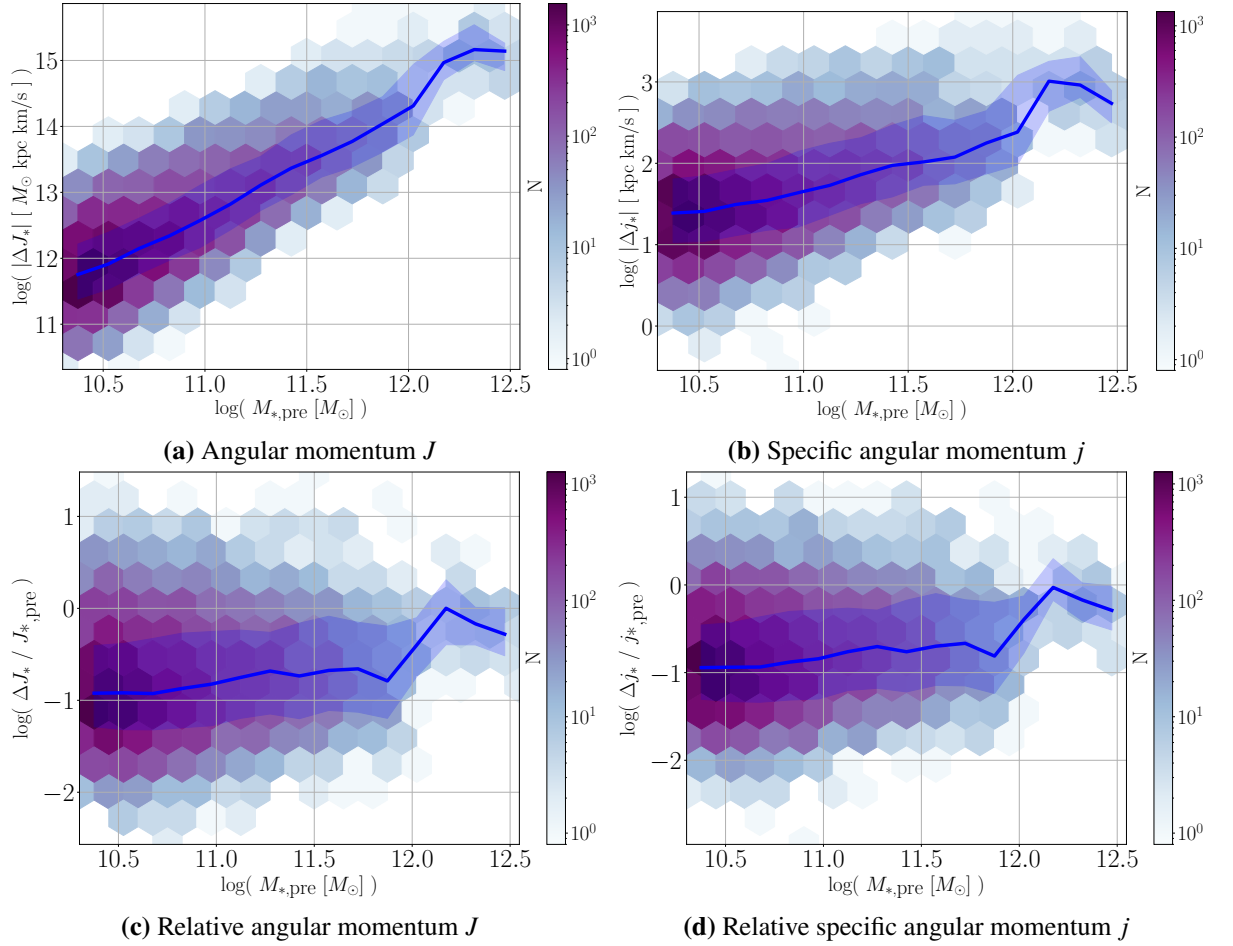
Figure 5.1: Heat map of instant spin magnitude changes related to the subhalo masses prior to the transition. The left-hand figures show the angular momentum changes $\|\Delta J\|$, while $\|\Delta j\|$ is shown on the right. The top row shows changes in absolute values ΔJ and the bottom displays the spin change relative to the initial magnitude $\Delta J / J_{\mathrm{pre}}$ The blue line and shadows highlight the running median and 68th percentiles.

same for J and j. Across all halo masses, spin magnitudes change for about ten to twenty percent across time spans of hundreds of mega-years. The question remains as to why there is this self-similarity in spin transitions. Is the environment more turbulent for massive galaxies? Or is this actually more related to galactic radii than mass directly? Larger radii would result in a larger surface of the sphere, within which the angular momentum is calculated. A larger surface allows for a larger number of in- and out-flowing particles or subhalos. This would also mean that there is a larger sensitivity to fluctuations at the border, as the fluctuation of particle numbers increases, but also the fluctuation happens at larger radii, which both J and j depend on linearly.

(a) Angular momentum J

(b) Specific angular momentum j

(c) Relative angular momentum J

(d) Relative specific angular momentum j
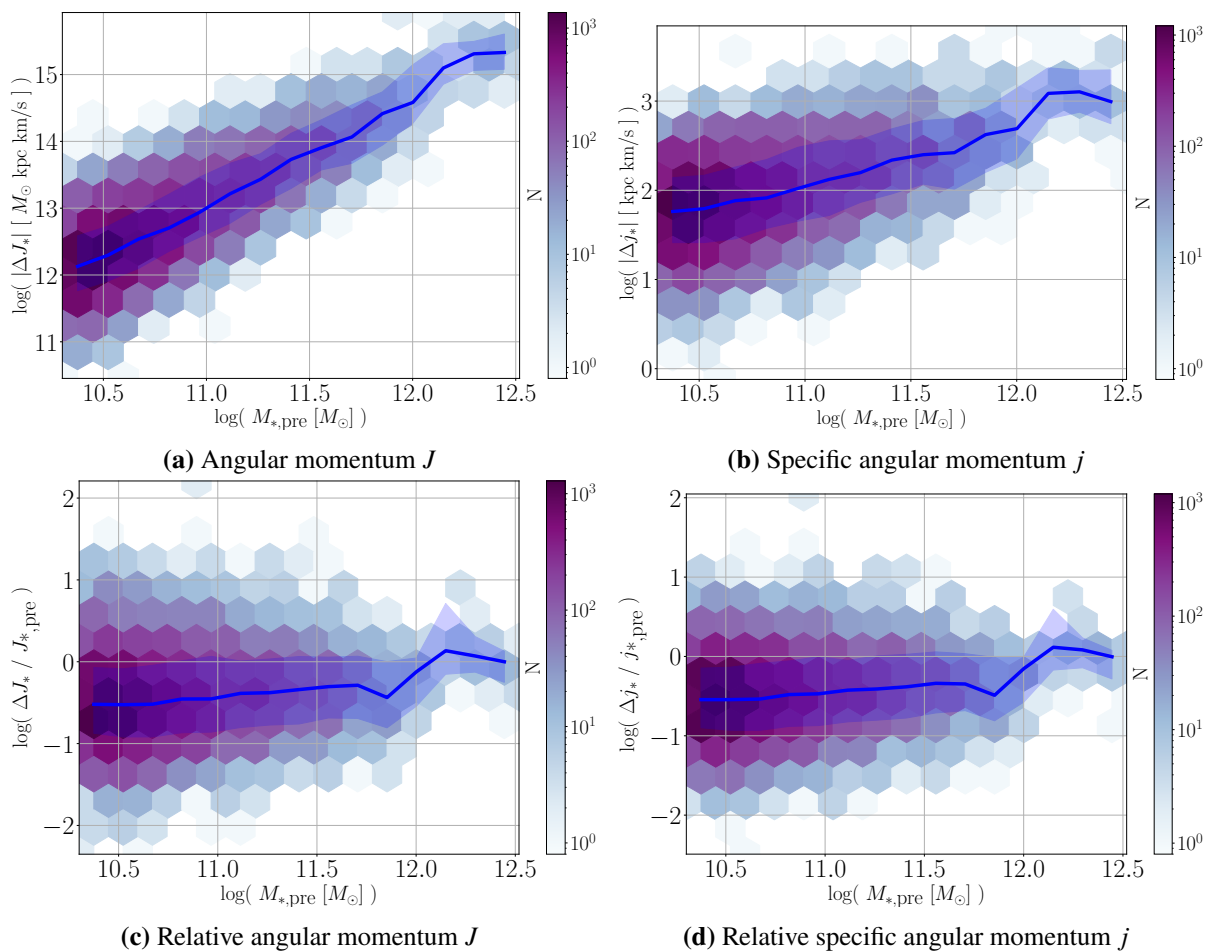
Figure 5.2: Heat map of long-term spin magnitude changes related to the subhalo masses prior to the transition. The left-hand figures show the angular momentum changes $\|\Delta J\|$, while $\|\Delta j\|$ is shown on the right. The top row shows changes in absolute values ΔJ and the bottom displays the spin change relative to the initial magnitude $\Delta J / J_{\text{pre}}$ The blue line and shadows highlight the running median and 68th percentiles.

The latter explanation would suggest that the 10%-changes mark a noise level due to the time-step resolution limit of 0.3 Gyr. With the stellar angular momentum being almost entirely included within ten percent (Figure 3.7), the radial dependence is considered a minor effect and not investigated further.

Next to magnitude, the second parameter in spin transitions is the angle, by which the vectors flip. Since the alignment of galaxy spins is studied in relation to structure formation (Welker et al., 2020), the flip angles will be considered in most of the following studies in this work. However, before that can be done, it is necessary to look at the general scope and limits of flip angles with respect to changes of spin. For that purpose, the theoretical limits between the relative spin changes J_{rel} and flip angles ϕ_{flip} are derived in the following section.

5.1   Theoretical Limits between Relative Spin Change and Flip Angle

To start off, the following nomenclature will be used:

$$x := |\boldsymbol{x}|$$

$$J_{\text{rel}} := \Delta J / J_1 \tag{5.1}$$

$$\Delta \boldsymbol{J} \equiv \boldsymbol{J_2} - \boldsymbol{J_1} \implies J_2 = \sqrt{J_1^2 + \Delta J^2 + 2 \boldsymbol{J_1} \Delta \boldsymbol{J}}$$

Further we need to consider the flip angle described by

$$\cos \phi = \frac{\boldsymbol{J_1} \cdot \boldsymbol{J_2}}{J_1 \, J_2} = \frac{J_1^2 + \boldsymbol{J_1} \cdot \Delta \boldsymbol{J}}{\sqrt{J_1^4 + J_1^2 \, \Delta J^2 + 2 J_1^2 \, \boldsymbol{J_1} \cdot \Delta \boldsymbol{J}}} \tag{5.2}$$

and the change alignment angle with its application

$$\cos \gamma = \frac{\boldsymbol{J_1} \cdot \Delta \boldsymbol{J}}{J_1 \, \Delta J} = \frac{\boldsymbol{J_1} \cdot \Delta \boldsymbol{J}}{J_1^2 \, J_{\text{rel}}} \tag{5.3}$$

$$\iff \boldsymbol{J_1} \cdot \Delta \boldsymbol{J} = J_1^2 \, J_{\text{rel}} \cos \gamma$$

Consequently, Equation 5.2 can be expressed as

$$\cos \phi = \frac{1 + J_{\text{rel}} \, \cos \gamma}{\sqrt{1 + J_{\text{rel}}^2 + 2 J_{\text{rel}} \cos \gamma}} \tag{5.4}$$

In order to find the maximum angle possible for a given J_{rel}, the minimum of Equation 5.4 with respect to the change alignment angle is determined by a solution for

$$\partial_\gamma \cos \phi = - \frac{J_{\text{rel}}^2 \, \sin \gamma \, (J_{\text{rel}} + \cos \gamma)}{(1 + J_{\text{rel}}^2 + 2 \, J_{\text{rel}} \, \cos \gamma)^{3/2}} \overset{!}{=} 0 \tag{5.5}$$

Out of the possible solutions

$$\gamma = \begin{cases} 0 \\ \pm \arccos{(-J_{\text{rel}})} \end{cases} \tag{5.6}$$

only the solution

$$\gamma = \arccos{(-J_{\text{rel}})} \tag{5.7}$$

can be related to the maximum flip angle and simplifies the equation to

$$\cos \phi = \frac{1 - J_{rel}^2}{\sqrt{1 - J_{rel}^2}} = \sqrt{1 - J_{rel}^2} \tag{5.8}$$

and reveals the solutions

$$\Rightarrow \quad \phi_{max} = \arcsin J_{rel}$$
$$J_{rel,min} = \sin \phi \tag{5.9}$$

For a randomly aligned $\Delta \boldsymbol{J}$, the expectation value is $\overline{\gamma} = 90°$, as the angle between two random vectors in 3D follows the probability distribution $\sin \gamma$. If we apply that to Equation 5.4, we find

$$\overline{\phi} = \arccos \frac{1}{\sqrt{1 + J_{rel}^2}}$$
$$\overline{J_{rel}} = \sqrt{\frac{1}{\cos^2 \phi} - 1} \tag{5.10}$$

The relations of Equation 5.9 and 5.10 are implemented as black lines in Figure 5.3 as a reference.

Figure 5.3 shows the relation between relative spin changes and flip angles of the galaxies. We find three types of basic information here. The running median, the scatter and the color distribution. Striking to the eye is the perfect color consistency in the three sub-sample panels of the left-hand figures. This is by design, as those sub-panels in each sub-figure represent the classification into disks (blue), intermediates (yellow) and ellipticals (red) prior to the transition and therefore comply with the color scheme rule. In contrast, the right-hand side figures show the b-value colors after the time step, while keeping the classification from before for the division into sub-panels. Around $\Delta J_{rel} = 1$ different morphological evolution paths split up. Large flips close to $\Delta J_{rel} = 1$ cause b-value drops for all three populations. Then there is a region at the bottom right corner that increases the b-value for intermediates and ellipticals, with dominating spin influx. That region does not exist for disks, telling us that large relative spin changes with alignment to the original spin do not occur for them. As is more clearly shown in Figure 5.4, the flip angles of the three populations deviate differently from random. While the median of ellipticals follows the line of randomly aligned $\Delta \boldsymbol{J}$ rather consistently, the flip for intermediates and disks tends to be aligned with the galaxies' spins. This effect holds for instant flips as well as long-term ones, which is interesting, as is suggests that the environment of disk galaxy tends to share the spin orientation.

(a) Instant, b_{pre}

(b) Instant, b_{post}

(c) Long-term, b_{pre}

(d) Long-term, b_{post}
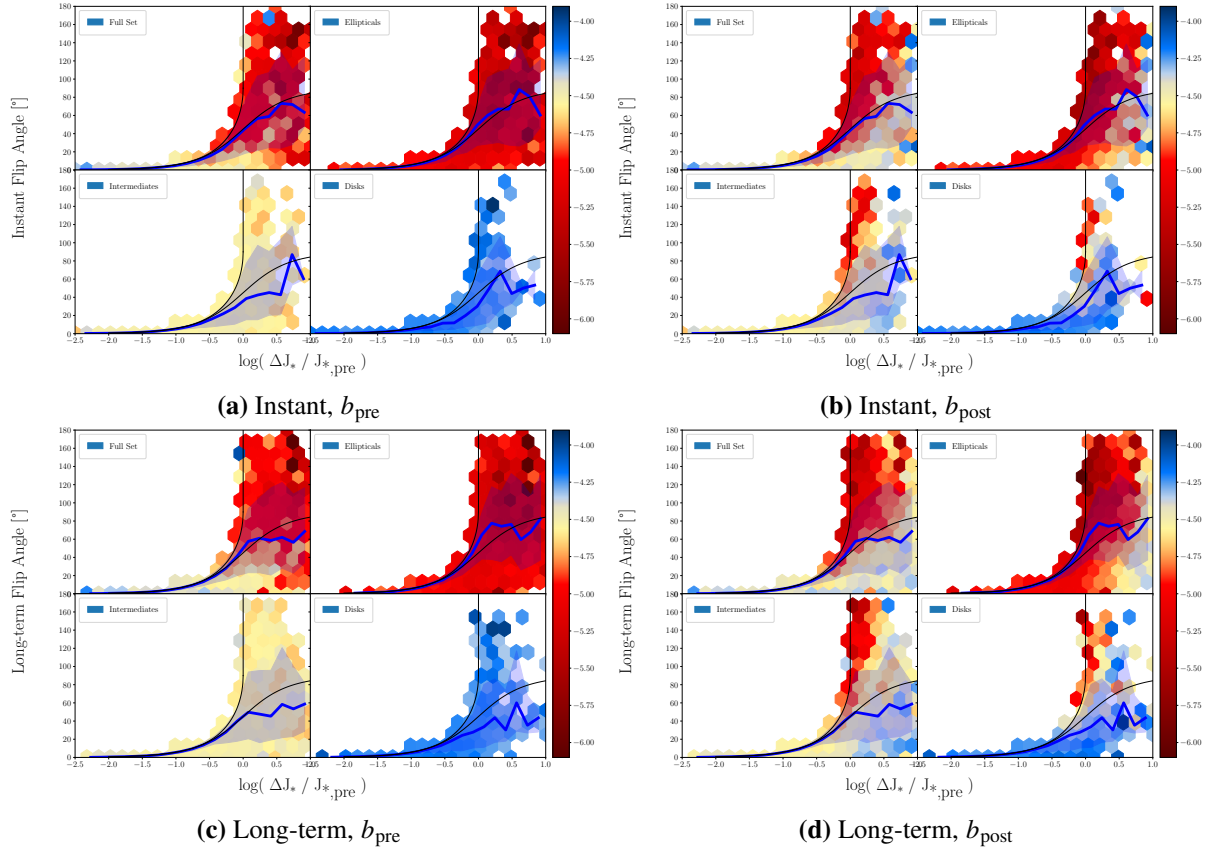
Figure 5.3: Flip angles ϕ_{flip} plotted against ΔJ_{rel} over instant time-steps at the top and long-term transitions at the bottom. The colors indicate the mean b-value in a bin, prior to (left) and after the flip (right), while the four sub-panels show the total sample and a division into three sub-samples according to their morphological type taken from the b-values prior to the flip for the left- and right-hand figures. The blue lines and shades trace the running median and 68th percentiles. The black lines show the theoretical limit and expectation for random changes as described in Equation 5.9 and 5.10. The corresponding heat map is attached in the appendix as Figure A.5.

5.2   Flip Angles and Spin Transitions

From linear algebra, it is expected to find that the relative spin change magnitude ΔJ_{rel} is related to the flip angle. But can we also relate a flip angle to the absolute kinematics of a galaxy? In Figure 5.5, I try to relate the initial spin of a subhalo to its upcoming flip. For these quantities, when looking at the differences for time-step sizes, we find that transitions over 0.3 Gyr and 1 Gyr largely agree. The distribution scatters towards larger flip angles with for longer time steps, and thus have higher number statistics providing a smoother running median. Now we can try to confirm our original assumptions of high-spin galaxies being more resistant to large flip angles than low-spin ones. Interestingly, the distribution rests at a surprisingly constant value and the scatter is generally smaller for small values of ϕ_{flip}. Then

(a) Instant, b_{pre}

(b) Instant, b_{post}

(c) Long-term, b_{pre}

(d) Long-term, b_{post}
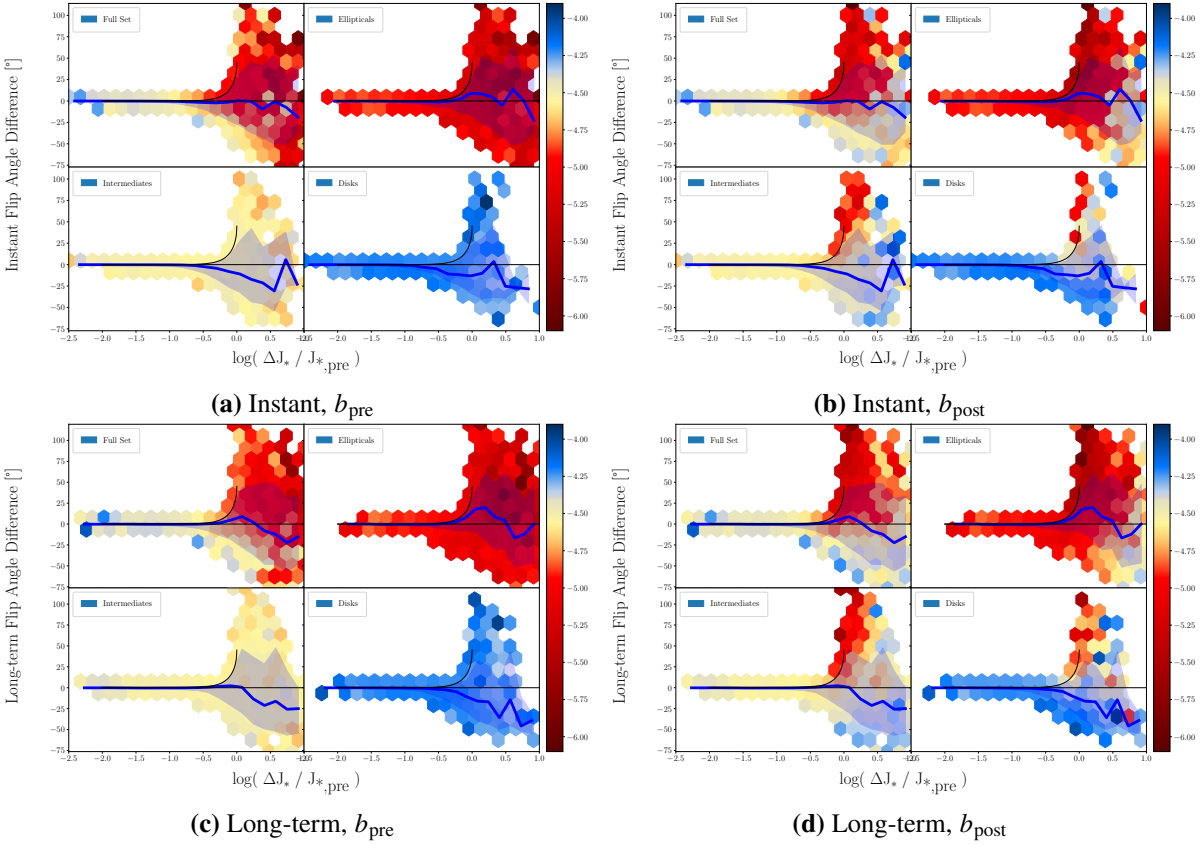
Figure 5.4: Flip angle deviation from randomly aligned $\Delta \boldsymbol{J}$ plotted against ΔJ_{rel} over instant time-steps at the top and long-term transitions at the bottom. The colors indicate the mean b-value in a bin, prior to (left) and after the flip (right), while the four sub-panels show the total sample and a division into three sub-samples according to their morphological type taken from the b-values prior to the flip for the left- and right-hand figures. The blue lines and shades trace the running median and 68th percentiles. The black lines show the theoretical limit and expectation for random changes as described in Equation 5.9 and 5.10.

we only find the expected relation for elliptical galaxies and the combined sample. Disks and even intermediates have constant or even increasing values of J_{pre}. Admittedly, over long time steps, intermediates follow a completely constant distribution. Only if we restrict our observations to the region of $\phi_{flip} < 30°$, the initial assumption is confirmed. The reason for the combined sample to show the most intense effects is due to the scatter. If we look at the three sub-panels, we find that the three galaxy classes have different basic spin magnitudes and in addition have a different contrasts of small-flip numbers to large ones. As those two effects are convoluted in the combined sample, we find that the trend is mostly determined by how many subhalos of which type are found for a chosen flip angle. Overall, the results indicate that a direct connection between flip angles and spin magnitudes can only be made for ellipticals

that have small spins to begin with. Other galaxies barely undergo large-flip events and if they do, the events are violent enough to overrule any angular momentum, the galaxy has had.

(a) J_{pre}, Instant

(b) j_{pre}, Instant

(c) J_{pre}, Long-term
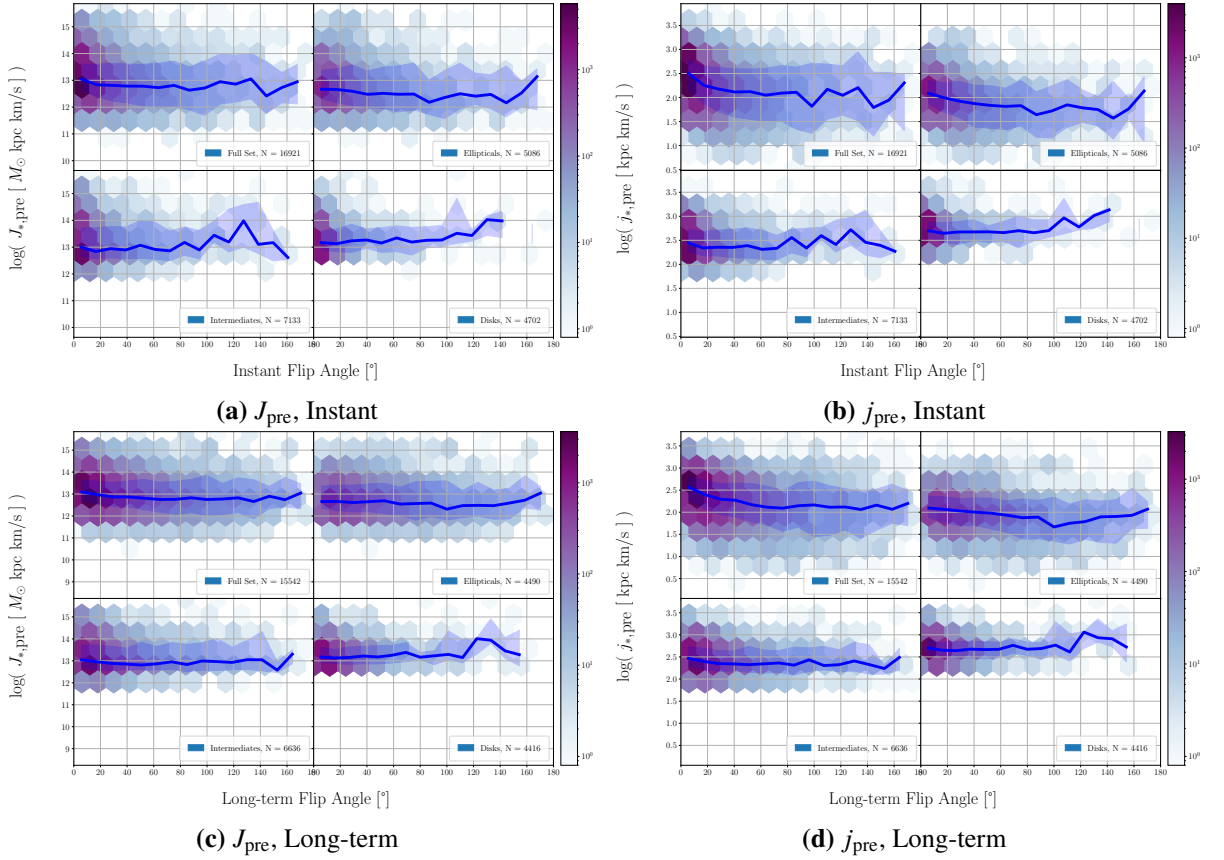
(d) j_{pre}, Long-term

Figure 5.5: Heat map in logarithmic colors of spin magnitudes prior to a time step plotted against the upcoming flip angle. J_{pre} is used in the left-hand figures, j_{pre} on the right. The top figures display instant transitions and long-term ones lie at the bottom. The blue lines and shades mark the running median and 68th percentiles. Each figure is divided into sub-panels with the full sample, elliptical galaxies, intermediates and disks.

Up to this point, we have explored the spin change and flip angles with respect to the galactic morphology. However, as spin transitions are expected to be connected to disturbances by outer structures, star formation would also be affected by the influx of gas or added turbulence. Hwang et al. (2021) show in their merger-simulations, that after the first closest encounter between two merging galaxies, their angular momentum is distorted and the star-formation increases. The intensity of these effects can vary strongly with their collision parameters (prograde or retrograde with respect to the spin orientation of the observed galaxy), and of course the impact parameter. However, I expect the correlation to emerge on a statistical level for the sample of this work. With the intention to investigate that, we can look at Figure 5.6. Before we distinguish between the samples of different star-formation rates, we notice that the

imprint of the constraints of the ϕ_{flip}-ΔJ_{rel} relation (Figure 5.3) is underlying but smoothed out in the sub-panels of Figure 5.6. Then we need to consider the caveat that the number statistics differ greatly between the three samples, starting with large numbers for quiescent galaxies and ending up with only few for highly star-forming ones. The median generally stays in the region of $2.0 < \Delta j < 2.5$ with increasing values connected to larger flip angles, as to be expected. However, the contrast between numbers of small flips and large flips is stronger low star-formation rates, especially considering the logarithmic color scale Highly star-forming galaxies are comparatively more likely to just have undergone a larger flip and spin transition within the past gigayear. This claim is supported by the comparisons made in Table 5.1. Interestingly, the group of medium-star-forming galaxies has the lowest ratio, and therefore the highest concentration of galaxies after small spin flips.
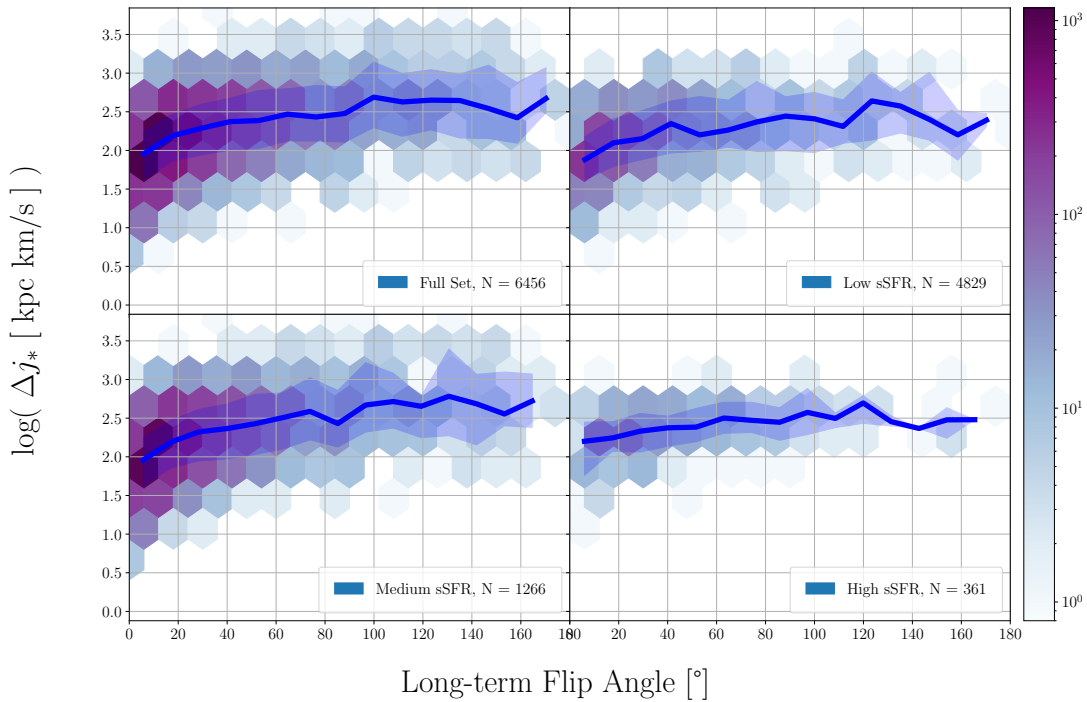
Figure 5.6: Specific angular momentum change magnitudes Δj plotted against the related flip angle. The blue lines and shades show the running median and 68th-percentile distributions. The figure is divided into sub-panels with the full sample and sub-samples from low to high specific star-formation rates separated as shown in Figure 3.10b. The colors scale logarithmically with bin counts.

Like for Figure 5.5, the strongest difference in trends is found for $\phi_{\text{flip}} < 30°$. For highly star-forming galaxies, there is a much shallower drop towards $\phi_{\text{flip}} = 0°$, while for medium and low sSFR subhalos, the bulk resides here with an abundance of small Δj. One can conclude that a high star-formation rates are observed in subhalos that have experienced larger changes of their spin, independently of large flip angles. This correlation matches the expectations

$N_{\mathrm{a}}/N_{\mathrm{b}}$	$\phi_{\mathrm{thr}} = 30°$	$\phi_{\mathrm{thr}} = 60°$	$\phi_{\mathrm{thr}} = 90°$
All	0.39	0.12	0.05
Low sSFR	0.49	0.15	0.07
Medium sSFR	0.34	0.10	0.04
High sSFR	1.04	0.29	0.09

Table 5.1: Ratios $N_{\mathrm{a}}/N_{\mathrm{b}}$ of numbers of subhalos above and below a flip angle threshold $\phi_{\mathrm{thr}} \in \{30°, 60°, 90°\}$. Different values are calculated depending on the sub-sample in accordance with Figure 5.6.

that high star-formation rates usually appear as a result of disturbances of a subhalo angular momentum. However, according to Table 5.1, the correlation is restricted to the highest values of sSFR.

We started this chapter with assumptions on how kinematics as one of galaxies prerequisites determine the range and conditions of upcoming flips. As a factor of Spin J, mass was tested for its contribution. On a statistical level, mass has no impact in spin transitions, as the changes of angular momentum also increase so that galaxies experience the same spin change magnitude with respect to their mass. Whether this effect appears due to the way, the sample is produced (time-step size, radial cut at 10% R_{vir}) or this is due to the environment that statistically changes with mass, remains a question for future work. Then the influence of morphology was tested by comparing the relative spin change magnitude ΔJ_{rel} to the flip angle ϕ_{flip}. Complying with expectations, large flips can be generally associated with the decrease of rotational support. The most interesting result of that analysis was that disks have less randomly-oriented spin changes, telling us that the immediate environment of disks and even intermediates have a slight alignment with their intrinsic spin. This effect is noticeable but weak, so further investigation with regards to epoch of the universe, mass dependence or environment could help reveal further insight. Moving away from relative spin changes, the relation between initial spin and flip was tested expecting higher spins to be more robust. Contrary to expectations, this is only confirmed for ellipticals. As the b-value increases, large flips become less likely, but if they appear, it is independent of the spin magnitude at the beginning of the transition. The last point of this chapter is that we do find traces of spin-flip-induced starbursts and confirms expected trends considering the scenarios shown by Hwang et al. (2021). With star-formation rates being a fundamental quantity of galaxies and its popularity in observations, including tight relations to morphology and evolution (Madau & Dickinson (2014)), they will be further analyzed in the following chapter 6.

Chapter 6

Star Formation Rate

Analogous to angular momentum, the star formation of a galaxy is affected by the surroundings. It mainly depends on the availability of cold gas that can clump and collapse to stars. Dekel et al. (2009) found in simulations that the accretion of cold gas via narrow streams from the cosmic web in the early universe was responsible for the bulk of star formation at $z \geq 2$, but also quenching mechanisms like stellar feedback in smaller galaxies and gravitational heating in more massive halos. The different effects can be explained by the nature of the influx, because in contrast to smooth streams, mergers are responsible for extreme star bursts, but also destroy the disk, while a coherent clumpy stream will dominate the disk spin and slowly contribute to the central bulge until the galaxy becomes a quenched elliptical. Either scenario shows that star-formation is a quantity closely tied to a galaxy's intrinsic kinematics.

From chapter 5, we get a hint that starbursts and spin changes are related supported by the effects of merger scenarios as studied by Hwang et al. (2021). In an attempt to make a more direct connection, we can consider Figure 6.1. For spin changes Δj, one could make an argument for the high-density region to show different trends for ellipticals, intermediates and disks, but the differences are barely noticeable especially considering the large uncertainty.

A more clear trend emerges for Δj_{rel}. Especially for long-term transitions, we find that larger relative spin changes are connected to higher star-formation rates. Interestingly, the relation appears strongest for intermediates over short time steps. Here, we need to consider that the classification is performed after the end of the transitions. If we recall Figure 5.3b, this sample can consist of former ellipticals with aligned intense spin changes or disks that experience large flips. Table 6.1 shows this in absolute numbers.

(a) Instant Δj_*

(b) Instant Δj_{rel}

(c) Long-term Δj_*

(d) Long-term Δj_{rel}
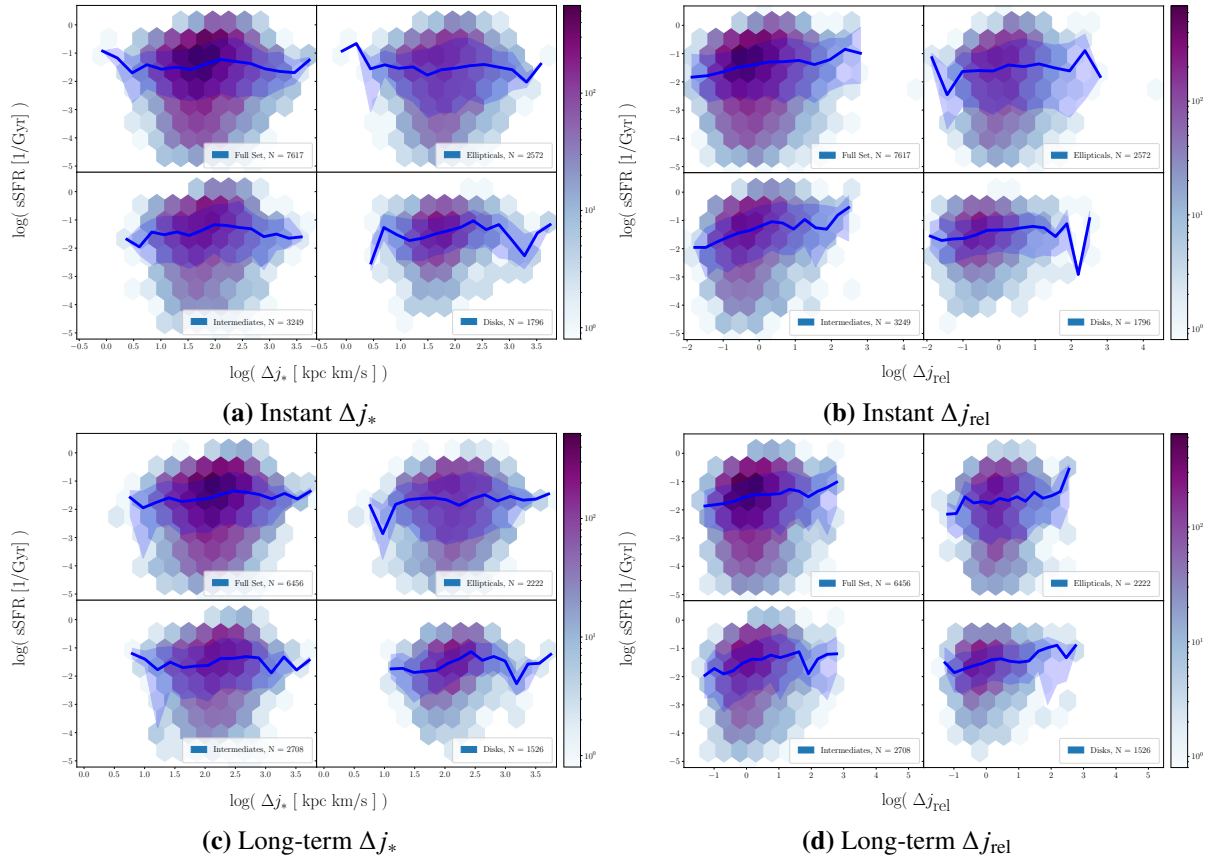
Figure 6.1: Heat map of specific star-formation rates of the galaxies plotted against spin changes. Each set of four sub-panels shows the full sample and three sub-samples according to the classification by b-value. The top figures contain instant transitions and the bottom goes over longer time steps. The left- and right-hand side figure differ by spin-change types Δj_* and Δj_{rel}. The blue line and shade demarcate the running median and 68-percentile region.

Short-term	$\mathrm{Ell_{pre}}$	$\mathrm{Int_{pre}}$	$\mathrm{Disk_{pre}}$
$\mathrm{Ell_{post}}$	1564	955	53
$\mathrm{Int_{post}}$	71	2073	1105
$\mathrm{Disk_{post}}$	12	32	1752

Long-term	$\mathrm{Ell_{pre}}$	$\mathrm{Int_{pre}}$	$\mathrm{Disk_{pre}}$
$\mathrm{Ell_{post}}$	1214	879	129
$\mathrm{Int_{post}}$	155	1654	899
$\mathrm{Disk_{post}}$	7	54	1465

Table 6.1: Start- and end-state numbers of star-forming galaxies for short time steps (left) and long ones (right).

6.1   Redshift Dependence

While we can observe a universal relation between spin transitions and star-formation, it is Up until now we have observed a universal relation between star-formation rates and changes to the stellar kinematics in a galaxy. However, the epoch of the universe plays an important role when considering star formation as discussed in the context of Figure 3.2. Additionally, I wanted to

test the consistency between classification by stellar kinematics and the star-formation rates. Both aspects are combined in Figure 6.2. Depending on the redshift bin, stellar kinematics and star-formation are related slightly differently. The trend is consistent with the expectations that disks tend to higher star-formation rates, but Figure 6.2b shows very clearly, that before the SFRD peak (Figure 3.2), the overall rates were higher and the correlation with angular momentum is weaker, suggesting that galaxies were generally more star-forming. As we look towards lower redshifts, the rates are generally much lower, but the correlation with galaxy class is noticeably stronger, meaning that in that epoch, the picture of star-forming disks and quenched ellipticals becomes more distinct.

(a) Heat map   **(b)** Linear fits
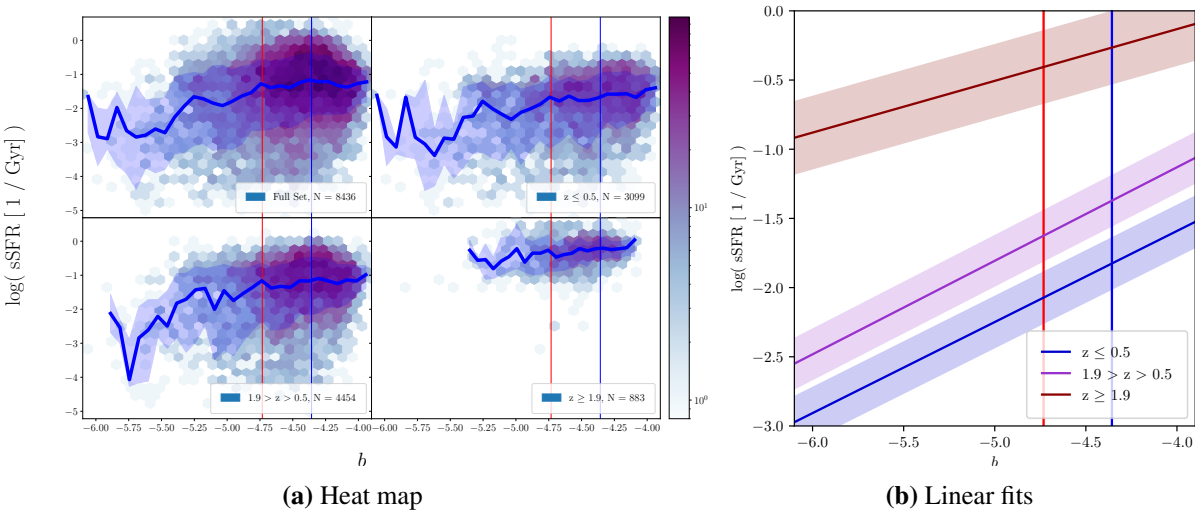
Figure 6.2: Relation between specific star-formation rates and the morphological b-value. The vertical lines demarcate the borders between disks, intermediates and ellipticals. Three sub-samples of redshift bins are considered: $z \leq 0.5$ (low), $0.5 < z < 1.9$ (medium) and $z \geq 1.9$ (high). *Left:* Heat maps, running median and 68th percentiles of full sample and the three sub-samples. *Right:* Linear regression with two free parameters for the sub-samples using the function $f(x) = a_1 \cdot x + a_2$. the colored shades outline the standard deviations of a_2. The fits were conducted with the package `LsqFit.jl` for `Julia` code.

This epoch-dependence of star formation also affects the view on Figure 6.1. The relations presented there can be further refined by splitting the plot up into different redshift bins as done in Figure 6.3. It shows impressively well that, only at high redshifts, starbursts can be linked to spin changes. At low redshifts, there is no trend or even a slightly negative one. The trend in Figure 6.3b barely shows in Figure 6.1a and Figure 6.1c, as the sample is generally dominated by low-redshift galaxies. Since the availability of cold gas is an important condition for star-formation, we could find better causal relations by considering it as well.

If we want to combine the puzzle pieces of this chapter and use flip angles as a measure of spin change, we end up with Figure 6.4. In this figure, we evaluate the three different galaxy

(a) $z \leq 0.4$ **(b)** $z \geq 1.2$
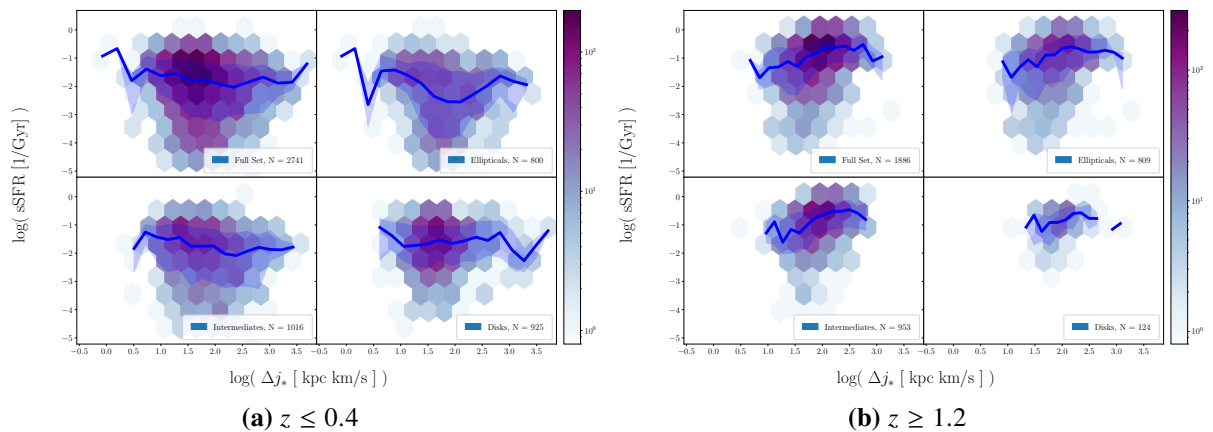
Figure 6.3: Specific star-formation rates versus angular momentum magnitude changes. Left and right differ from each other by their redshift bins of $z \leq 0.4$ and $z \geq 1.2$. In addition, the sub-panels show samples divided by morphological class at the end of the time step.

types at different redshifts, providing a sense of following them through time. The expected starburst-flip relation can be found preferably at higher redshifts, where the distribution scatter is also the smallest. Intermediates and disks maintain the trend until lower redshifts than ellipticals. This complies with expectations when considering that the heated halos stop the supply of cold gas of the inner galaxy (Dekel et al., 2009). Towards $z = 0$, lower star-formation rates seem to follow larger flip angles. But the numbers of cases provide increasingly unreliable results for larger b-values, which restricts the analysis to ellipticals. The latter have distributions with larger scatter, so ellipticals have a large range of more or less star-forming members across the full range of flip angles. This could either hint at a large range of cold-gas availability or a stronger time-dependence. The redshift bins cover long time frames where the star-formation rate densities decrease rapidly, as shown in Figure 3.2. If ellipticals are the main driver for this evolution, the redshift bins of Figure 6.4 would cover too many evolutionary stages creating a larger scatter. As a last point of this figure, I want to point out that classifying galaxies before or after the transition results in the same trends. Only disks show noticeable differences, as post-flip disks display similar trends as ellipticals. These could be the effect of quenched ellipticals that gained a large amount of angular momentum. Table 6.1 shows that these cases appear in relatively small numbers but matching the low count numbers in that sub-panel.

In accordance with expectations from the work by Dekel et al. (2009), the star-formation rate is primarily depending on the epoch of the universe. That also determines the relations with the evolution of the stellar galaxy components and their morphology. The latter is less of a factor at high redshifts where the morphological state is less related to quenching, but towards $z = 0$ the kinematic morphology becomes a good proxy for star-formation. The redshift-dependence also affects the relation between disturbances of a galaxy's stellar component and

(a) Pre-flip classification

(b) Post-flip classification
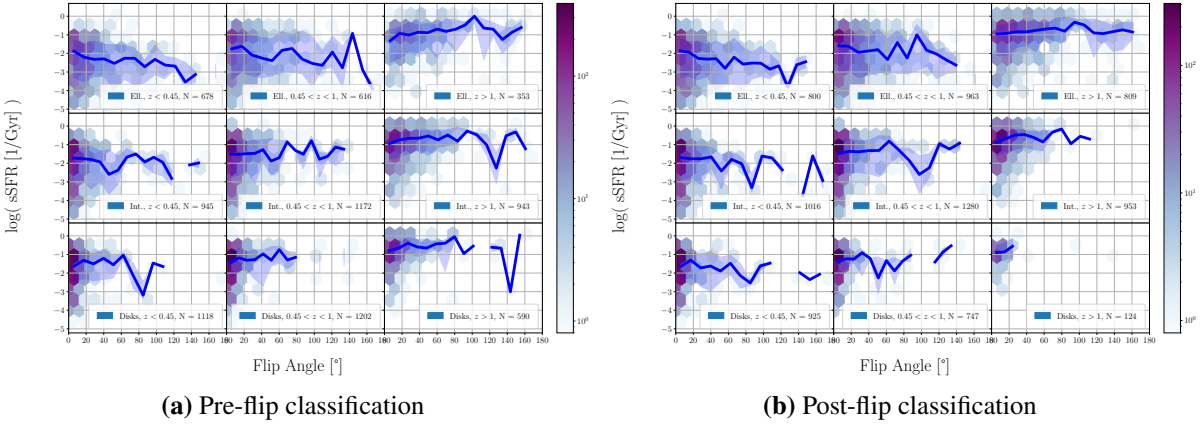
Figure 6.4: Evolutionary heat map of specific star-formation rates and the corresponding past flip angles. Following the sub-panels from left to right, we look at the distributions for bins with increasing redshift as $z \leq 0.4$, $0.4 < z < 1.2$ and $z \geq 1.2$. From top to bottom the sub-panels contain ellipticals, intermediates or disks. The classification is done either prior to the flip (left-hand figure) or after the flip (right-hand figure).

star bursts. This might be related to quenching and the stellar component primarily growing through accretion at low redshifts as found by Oser et al. (2010). Tracing the kinematics of the gaseous component and infalling star particles explicitly could fill the gaps of the relation and result in a better constrained picture.

Chapter 7

Mergers

Up to this point we have analyzed how angular momentum can change and its correlation with star-formation. In this chapter, we want to shed light on one of the causes of angular momentum changes: merger events.

7.1 What is a Merger?

This question is - both from a physical and a numerical point of view - not as trivial to answer as it seems. As for the definition in this work, a merger event has occurred when a subhalo is associated with more than one progenitor in a previous snapshot as described in Figure 2.3. This means that at this point, the merger is not massive and concentrated enough anymore to be identified by SUBFIND and is a late stage during a merger event. Even if the halo is not virialized by that time, the spin contribution is complete. If we want to relate a merger event to spin changes, a starting point needs to be defined. This is where the two samples of different time-step sizes must be compared. The 0.3-Gyr sample represents our maximum time resolution. However, depending on the merger parameters (mass ratio, impact parameter, initial velocities), the transfer of angular momentum has started long before SUBFIND registers a merger event. This can be through stripping of particles or gravitational interaction that creates tidal arms as a prominent example. The former is a physical process, but as to be seen in section 2.4, stellar particles are quickly attributed to the central halo by SUBFIND and considered stripped. To account for the time scales of merger processes better, the second sample with time-step sizes of roughly one gigayear has been created.

In order to compensate for stripping, merger masses are not measured just before the event, but the mergers are each traced back to the point of their maximum mass and evaluated there. Figure 7.1 shows how the merger masses compare to the mass differences between time steps.

While Figure 3.4 provides an overview of the individual merger masses, their sums within a time step are the preferred quantity here. The bulk of transitions show mass changes larger than the merger contribution as seen in Figure 7.1b. As some cases go beyond the black line, they are either cases where the traced-back merger masses differ much from the moment of merging or the observed galaxy loses mass simultaneously with stellar particles leaving the virial radius. The latter case does occur as shown in Figure 7.1a. Here, no relation with the black reference line is expected. Some cases of large mass loss and large merger mass accretion appear. These cases have not been checked further but they seem to be rather connected to problems with the methodology than actual processes.

(a) Mass loss

(b) Mass gain
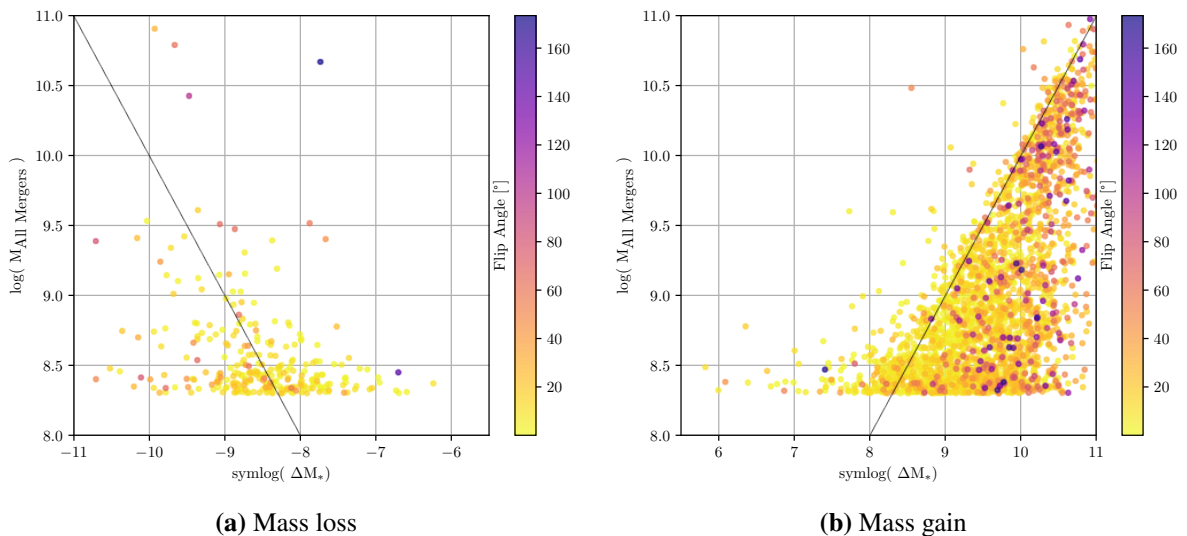
Figure 7.1: Comparison of sums of merger masses to the mass changes in the instant transition sample. The "symlog" label on the x-axis indicates that negative (left) and positive (right) mass changes are differentiated. Thus, negative values indicate losses of large stellar masses instead of values of $0 < \Delta M_* < 1 M_\odot$. The colors indicate the corresponding spin flip angles with large values plotted in front overlapping small values. The black line provides a reference for equal values.

7.2   Linking Mergers to Spin Flips

When flips occur, can they be directly related to a recent merger? Figure 7.2 and 7.3 make very clear that the connection can be made without precise knowledge about the merger alignment. Across all sub-panels the same trend is displayed with few differences in detail. From around the 1:10 ratio towards the 1:1 ratio marker, the median flip angles and their scatter become larger. Less rotational support, measured by J, j or b-value, results in a earlier, but less steep rise of flip angles and much larger scatter. It is impressive to see, how distinctively the flip

angles start to rise from the region of mini-mergers onwards, for systems with higher rotational support. This is partly due to the logarithmic scale but still shows that these borders are not purely arbitrary. The top- and center-row figures have a less smooth distribution due to their overall lower numbers. While the 0.3-gigayear sample has a total number of 16921 accepted transitions, only 3045 of them contain merger events. For the 0.9-gigayear sample, these numbers shrink to and 2596 respectively. The long-term flip sample shows similar trends but larger flip angles and a larger scatter. This affects the the bottom-row figures more than the merger transitions. While I would be inclined to see this as a sign that the greater time steps trace merger-induced flips better, this claim is barely supported by Figure 7.2 and 7.3 alone. While the figures successfully support expectations and show an impressively direct relation of flip angles and merger masses,

In a bottom-up hierarchical structure formation scenario, I expect galaxies in the early universe to be undergo higher spin changes, since giant ellipticals have not had the time to form and dominate their surroundings and more gas is transformed into stars. Figure 7.4 shows that there is a clear difference in merger scenarios when looking at different epochs of the universe. At higher redshifts, all galaxies experience larger flip angles independent for each merger ratio and significantly less ellipticals are present compared to the other types. In addition to that, the trend for ellipticals and intermediates is a more constant trend over the logarithmic merger ratio values, while they have constant values and show a steeper trend from around $\log(M_{\mathrm{gal}}/M_{\mathrm{Mergers}}) \approx 1.5$. As we have found star-formation to be highly redshift dependent in chapter 6, a hypothesis can be that flips are amplified by star-formation, triggered by accretion of even small halos. The redshift correction of the b-value could also play a role as it changes the classification. However, I consider that unlikely, since the trend also affects ellipticals. A non-physical explanation could be found in the effect of data points tending towards major mergers and thus providing a more balanced distribution across the x-axis range. Independent of the question about the background, it can be stated flips a larger at high redshifts.

The results above agree with studies by Welker et al. (2014), who linked flip angle distributions to merger mass accretion in a similar fashion. In their work, they make use of the HORIZON-AGN cosmological hydrodynamical simulation to study the correlation. Apart from the different simulation, structure finder and merger tree finder, their physical outlines are similar enough to expect complying results with the time step sizes range between 100 and 300 megayears and only subhalos with a stellar mass of $M_* \geq 2 \cdot 10^8 M_{\odot}$ are accepted as mergers, disregarding anything below that as smooth accretion. Their results and a direct comparison can be found in Figure 7.5. As a result, the trends are roughly similar: The more mergers mass is accreted over a time step, the more randomly are the flip angles distributed. For dark matter,

(a) Most Massive, *j*-split   **(b)** Most Massive, *J*-split   **(c)** Most Massive, *b*-split

(d) Sum, *j*-split   **(e)** Sum, *J*-split   **(f)** Sum, *b*-split

(g) ΔM, *j*-split   **(h)** ΔM, *J*-split   **(i)** ΔM, *b*-split
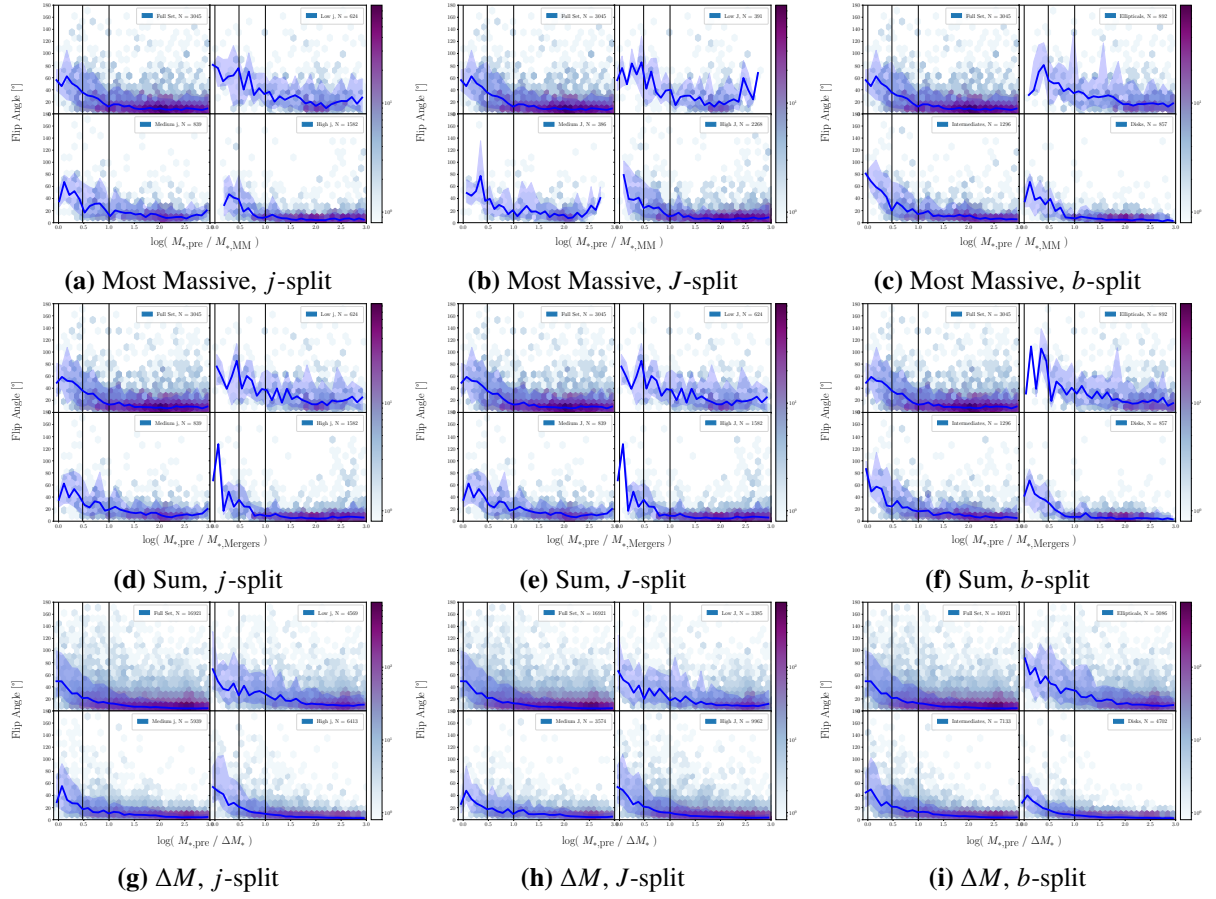
Figure 7.2: Instant flip angles plotted against logarithmic mass ratios. The three vertical black lines mark out the borders between ratios of (from left to right) 1:1, 1:3 and 1:10. In case of mergers, these borders classify the incidents as major mergers ($> 1 : 3$), minor mergers ($> 1 : 10$) and mini-mergers ($< 1 : 10$). From top to bottom, the figures differ by their x-axes with most massive merger mass, sum of merger masses and mass change compared to the galaxy mass prior to the transition. From left to right, the sub-panels of each figure have been divided by *j*, *J* and *b*-value according to the limits found in Figure 3.6 and the morphological classes.

the differences are significantly smaller than for stellar mass. Unfortunately, the sample of this work has fewer data points available and therefore the distribution is less smooth and stable. Decreasing the number of bins from 10 to 5 was a way to compensate partly for that effect, but it is clear that the range is not properly covered by all sub-samples. An additional interesting point is that when including the full redshift range with many more transition events, the distributions become steeper, meaning that the same merger ratios cause smaller flip angles. This point agrees with Figure 7.4, which shows that flip angles are generally smaller at lower redshifts.

The statistical method from Figure 7.5 was used to investigate a different possible relation of mergers and spin flips. Figure 7.6 tests if the same trend can also be observed for the number

(a) Most Massive, *j*-split

(b) Most Massive, *J*-split

(c) Most Massive, *J*-split

(d) Sum, *j*-split

(e) Sum, *J*-split

(f) Sum, *b*-split

(g) ΔM, *j*-split

(h) ΔM, *J*-split

(i) ΔM, *b*-split
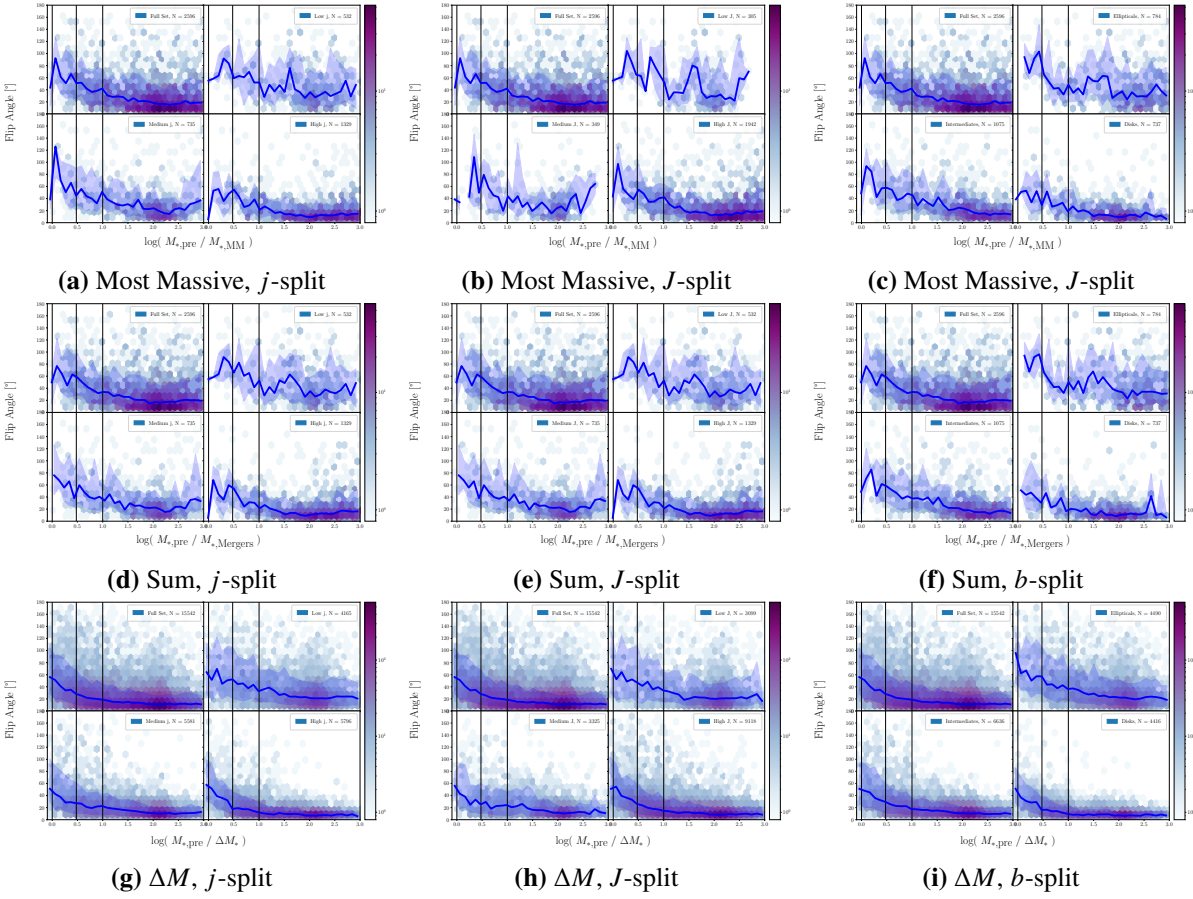
Figure 7.3: Same as Figure 7.2 but with Long-term flip angles plotted against logarithmic mass ratios. The three vertical black lines mark out the borders between ratios of (from left to right) 1:1, 1:3 and 1:10. In case of mergers, these borders classify the incidents as major mergers ($> 1 : 3$), minor mergers ($> 1 : 10$) and mini-mergers ($< 1 : 10$). From top to bottom, the figures differ by their x-axes with most massive merger mass, sum of merger masses and mass change compared to the galaxy mass prior to the transition. From left to right, the sub-panels of each figure have been divided by *j*, *J* and *b*-value according to the limits found in Figure 3.6 and the morphological classes.

of mergers instead of the sum of their masses. While the cases of more than ten mergers over one time step are few, the same general trend is clearly visible. For long-term flips, cases with many mergers show a similar distribution, whereas flips with few or no mergers show as strong increase towards more random flips. The latter point is expected, but the contrast to the former is interesting as this implies that longer time-steps only increase the noise level without helping to trace merger effect. Due to the low number statistics and logarithmic scale, it might also be a misconception.

This section showed a clear impact of merger size and numbers on angular momentum flips, even when using a simplistic approach as in this work. The results inspire to look into how well it is possible to predict the spin transition from the incoming mergers.

(a) Instant transitions   **(b)** Long-term transitions
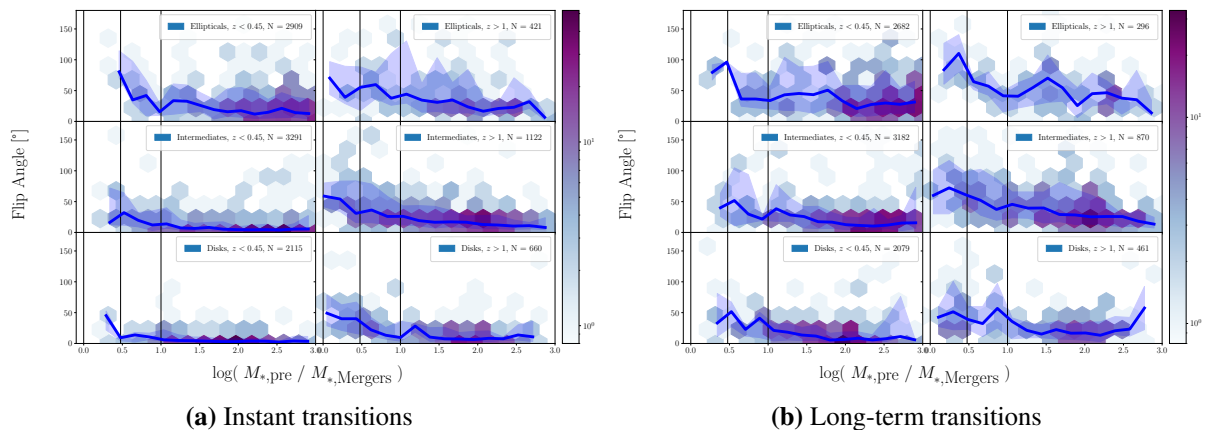
Figure 7.4: Flip angles plotted against logarithmic mass ratios of central halo to sum of mergers. The three vertical black lines mark out the borders between ratios of (from left to right) 1:1, 1:3 and 1:10. In case of mergers, these borders classify the incidents as major mergers ($> 1 : 3$), minor mergers ($> 1 : 10$) and mini-mergers ($< 1 : 10$). The left and right figures differ by the time step size of the transition. In each figure, the sub-panels show upcoming transitions of (from top to bottom) ellipticals, intermediates and disks at different redshifts (from left to right) within $z < 0.45$ and $z > 1$.

7.3   Flip Prediction

In the attempt to predict the spin flip due to a merger, one has to consider the two components of angular momentum transported by the merger into the galaxy. One is the intrinsic angular momentum according to Equation 3.1 and the other is the orbital angular momentum J_{orb}. It is defined with respect to the physical rest frame of the accreting central galaxy as

$$J_{\mathrm{orb}} = M_{\mathrm{merger}} \cdot \left(x_{\mathrm{merger}} - x_{\mathrm{central}} \right) \times \left(v_{\mathrm{merger}} - v_{\mathrm{central}} \right) \tag{7.1}$$

Figure 7.7 shows that the orbital angular momentum dominates the two components by easily two orders of magnitude in all methods. Also, when reading out the data at an earlier time, the whole distribution shifts to slightly higher values, supporting the expectation that parts of the angular momentum are transferred long before the registration of a merger event. For the further analysis the two components are added.

As a first impression of how well we can predict the angular momentum change, the magnitude of spin change and contribution from mergers are compared in Figure 7.8. The figure shows a promising image as the merger contributions follows the measured changes, albeit with a median offset of about half an order of magnitude. The larger time steps clearly show no improvement, as the mergers tend to underestimate the spin change, which only increases with this method. Reading out the merger spin at an earlier time reveals an interesting behaviour. While the immediate read-out method consistently underestimates the
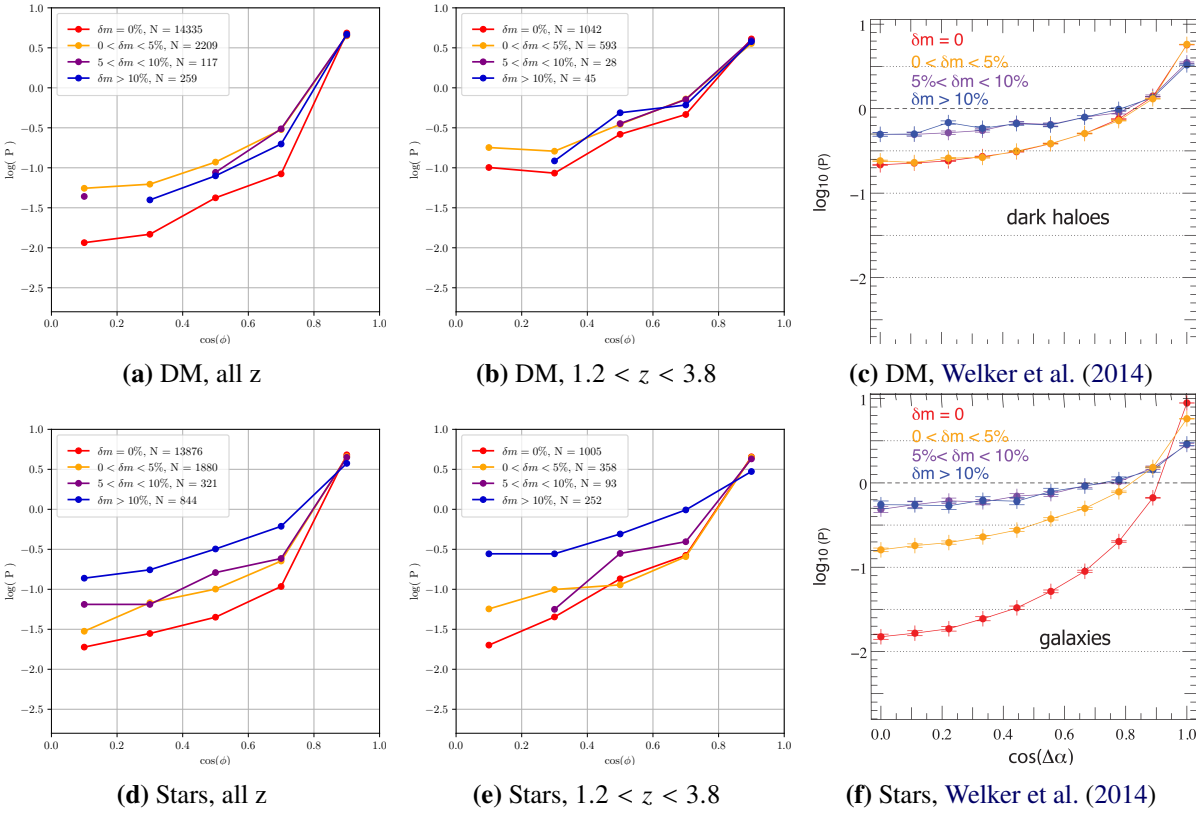
Figure 7.5: Logarithmic probability distribution functions of $\cos\left(\phi_{\text{flip}}\right)$ (or $\cos\left(\Delta\alpha\right)$ as the equivalent by Welker et al. (2014). The four different colors denote transitions where the sum of mergers transported mass fractions of >10 % (blue), 5 - 10 % (purple), <5 % (yellow) and 0 % (red, no mergers) into the galaxy. The range of $0 \leq \cos\left(\phi_{\text{flip}}\right) \leq 1$ translates to $90° \geq \phi_{\text{flip}} \geq 0°$. A vertical line would mean a random distribution of angles. The top-row sub-panels show the interaction between dark matter halos and the stellar components are shown at the bottom. The right-hand plots are from the work by Welker et al. (2014). The central plots use the sample of this work, but the same redshift range of $1.2 < z < 3.8$ and the left-hand plots include galaxies from all available redshifts.

spin change with a constant offset, reading out at an earlier time creates a different trend. Very small spin changes even get overestimated while at the higher end, we return to the negative offset as found with the immediate read-out. This method seems to work better as it lies closer to the ideal line but it comes at the cost of a larger scatter and differing trend. The colors are none the less interesting as they show how the spin changes by mergers are especially underestimated for disks undergoing small changes. Ellipticals, on the other hand, get overestimated for transitions with small changes. The separation of the two classes fades out towards higher values of ΔJ.

With the spin change magnitude prediction working seemingly well, we can confidently move forward to spin flip angles ϕ_{flip}. As using instant transitions with merger spins from one gigayear before the event seemed the most promising approach (Figure 7.8b), it is selected for

(a) Instant flips   **(b)** Long-term flips
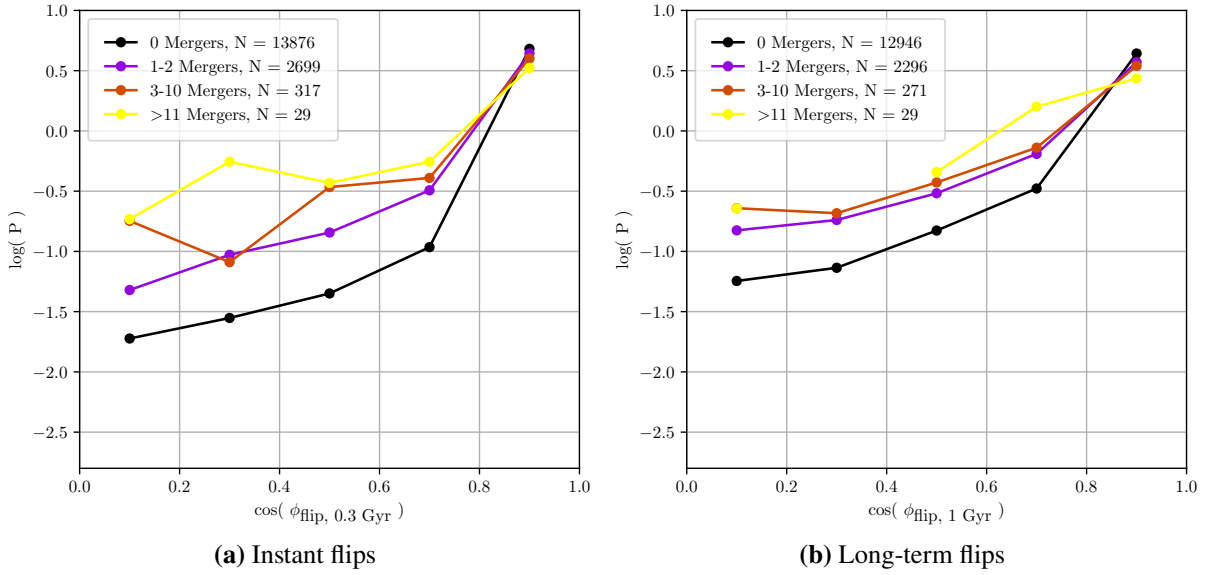
Figure 7.6: Similar to Figure 7.5, logarithmic probability distribution functions of $\cos\left(\phi_{\text{flip}}\right)$. The graphs of different colors differ by the number of mergers as 0 (black), 1-2 (purple), 3-10 (dark-red) and yellow (≥ 11). Instant and long-term transitions are plotted on the left and on the right respectively.

(a) Immediate J **(b)** Earlier J
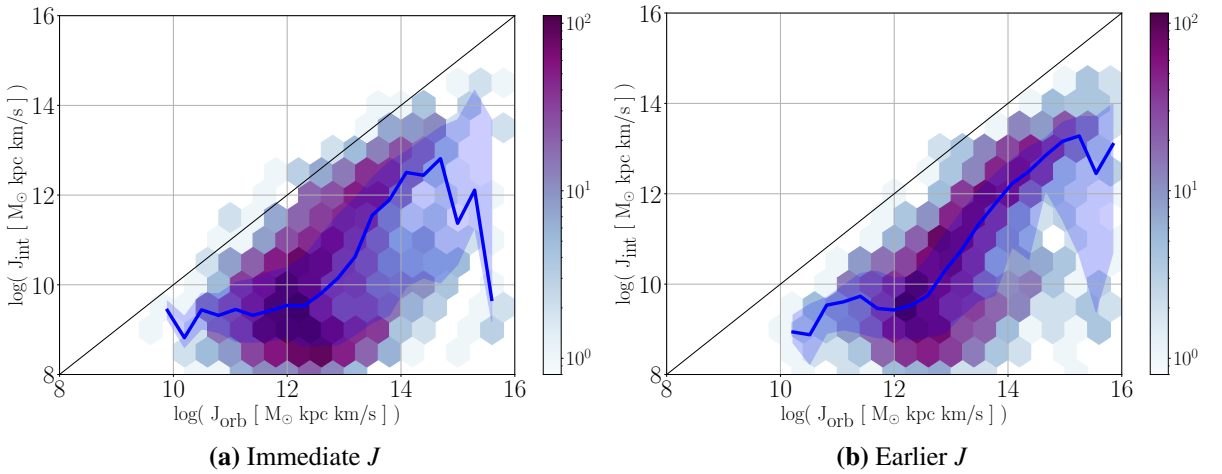
Figure 7.7: Heat map of intrinsic and orbital merger angular momentum components. The black line marks the positions of equal magnitude. The blue line and shades trace the running median and 68th-percentile regions. In the left-hand plot the angular momentum is evaluated right before the merger event, while the right-hand plot shows the situation roughly one gigayear earlier.

the flip angle prediction in Figure 7.9. The scatter of the distributions is huge, as noticeable when looking beyond the 68th-percentile regions at the actual distribution of the data. It does not seem to reveal much of a relation at all. The extreme values merely cancel out to end up with a running median that is somewhat close to the ideal line. This point becomes more clear when regarding the figures with more focus on smaller angles, where predictions seem to work best. As higher values are excluded from the median calculation, it drops further below the

(a) Instant flips, immediate J_{merger}

(b) Instant flips, earlier J_{merger}

(c) Long-term flips, immediate J_{merger}

(d) Long-term flips, earlier J_{merger}
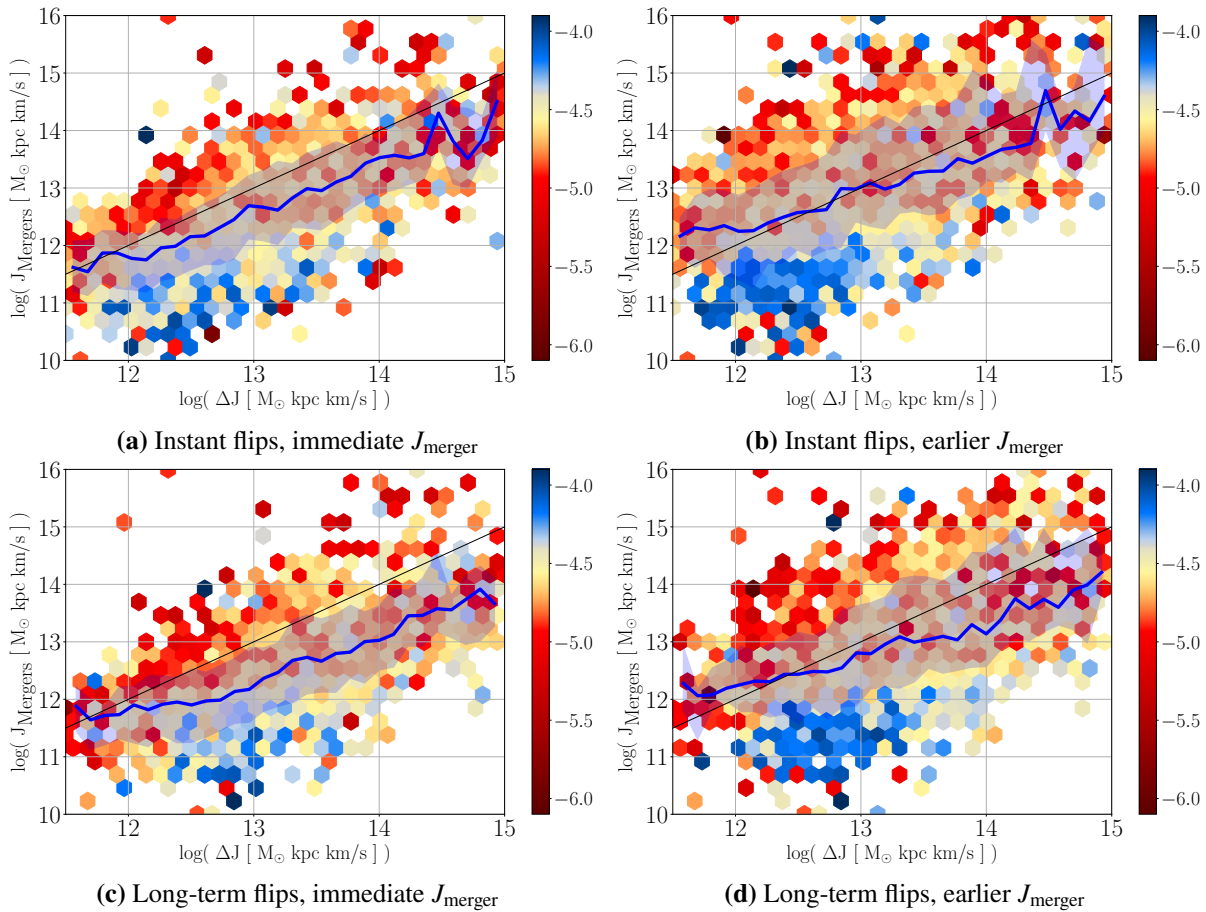
Figure 7.8: Angular momentum that is expected from the incoming mergers plotted against the actual measured change over a transition. The black line marks the one-to-one relation. The blue line and shade trace the running median and 68th percentiles. The colors of the bins are determined by their mean b-values. The figures on top show instant transitions, whereas the bottom row shows long-term transitions. On the left, the merger orbital spins are calculated as soon as possible before the merger is registered. On the right, the mergers were traced back by roughly 1 gigayear and their orbital spin with respect to the galaxy was evaluated there. The corresponding heat map is provided by Figure A.2 in the appendix.

ideal line. The other methods of calculating the angular momentum change do not improve this image as can be seen in section A.2 in the appendix. Figure 7.10 provides further context, showing that on the ideal line, the predicted and measured spin magnitudes are on average equal. The flip angle is underpredicted where the magnitude is also underpredicted and vice versa. When linking the results to Figure 7.8, this seems to be a problem tied to the galaxies' morphology

I conclude this chapter with a partial success on linking mergers to measured spin flips. While mergers can be unambiguously linked to angular momentum changes, the methods used in this work are insufficient to predict the changes from the angular momentum that is

(a) log-log scale

(b) $0° \leq \phi_{\text{flip}} \leq 180°$

(c) $0° \leq \phi_{\text{flip}} \leq 30°$

(d) $0° \leq \phi_{\text{flip}} \leq 5°$
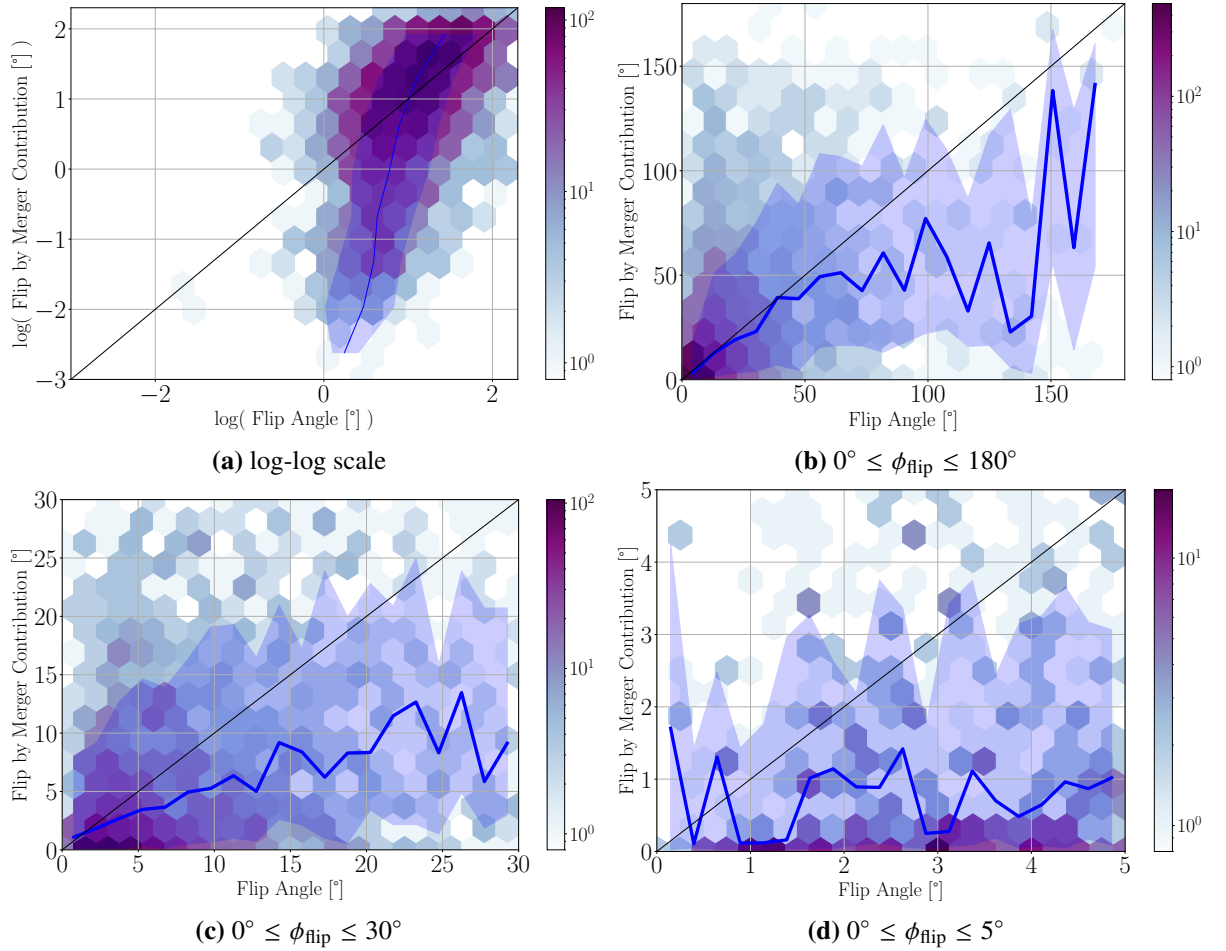
Figure 7.9: Prediction of flip angles by merger spin transport compared to measured instant flip angles on a logarithmic heat map. The merger spin was measured roughly one gigayear prior to the merger event for this figure. The black line marks the theoretical one-to-one relation. The blue line and shades follow the running median and 68th-percentile regions. The top-left figure covers the full range of angles $0° \geq \phi_{\text{flip}} \geq 180°$ on a double-log scale. The other three plots show linear scales with different ranges from 0° to 180° (top right), to 30° (bottom right) and up to 5°. For comparison, the analogous figures for the other methods are attached in the appendix as Figure A.3 and A.4.

contributed by mergers. This could have various reasons: One could be the impact of smooth accretion, star-formation or the influence of the tidal field. The problem might also be of conceptual nature, as the precise attribution of particles to the central galaxy or a subhalo can have a large impact when considering section 2.4. The discrepancy between the accuracy of predictions of spin magnitude changes and flip angles emphasizes how much more sensitive the latter is and highlights the difficulty of relating spin alignments with the cosmic web. With its high sensitivity it could also prove to be a suitable quantity to disentangle the influences on spin changes.

(a) log-log scale

(b) $0° \leq \phi_{\text{flip}} \leq 180°$

(c) $0° \leq \phi_{\text{flip}} \leq 30°$

(d) $0° \leq \phi_{\text{flip}} \leq 5°$
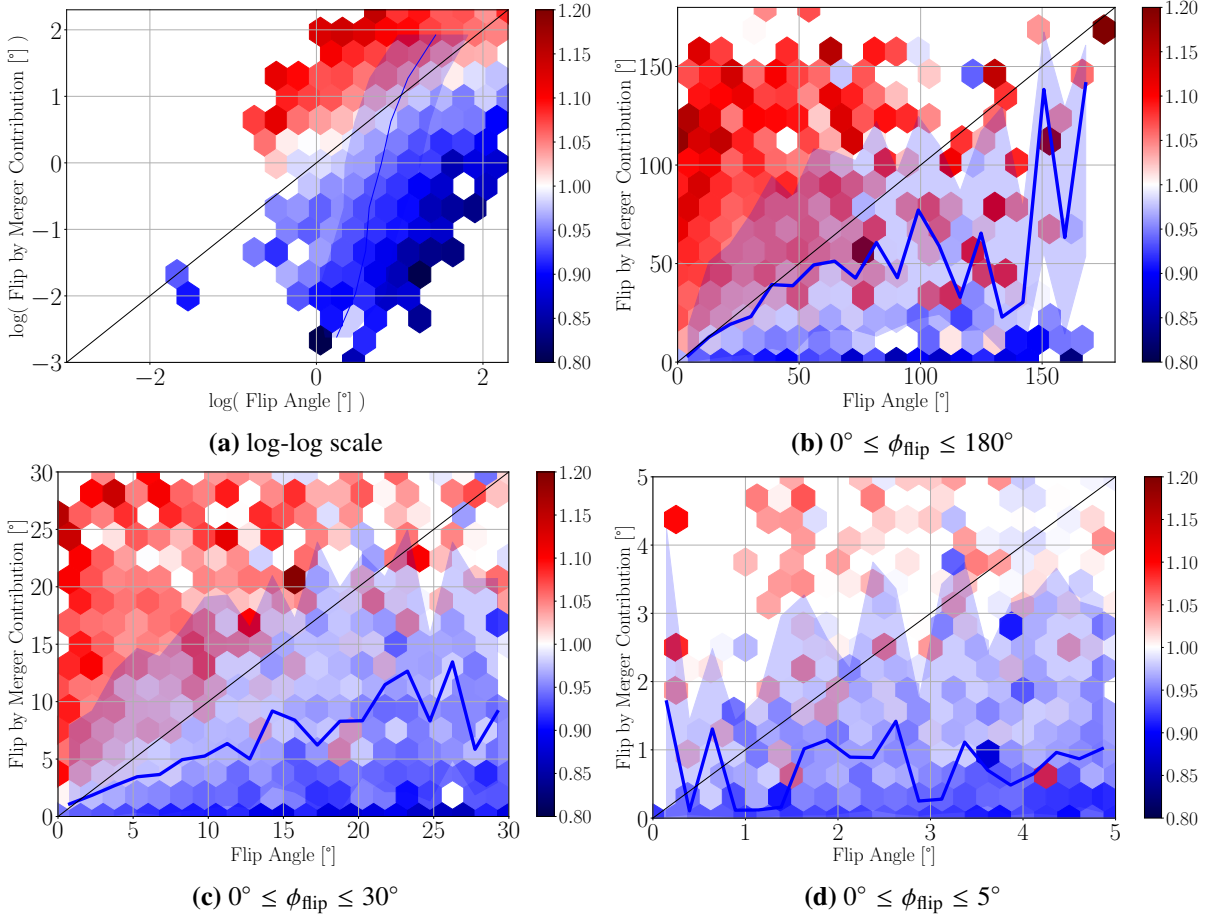
Figure 7.10: Prediction of flip angles by merger spin transport compared to measured instant flip angles. The bin colors highlight the mean ratio of ΔJ predicted by mergers to the measured ΔJ. The merger spin was measured roughly one gigayear prior to the merger event for this figure. The black line marks the theoretical one-to-one relation. The blue line and shades follow the running median and 68th-percentile regions. The top-left figure covers the full range of angles $0° \geq \phi_{\text{flip}} \geq 180°$ on a double-log scale. The other three plots show linear scales with different ranges from $0°$ to $180°$ (top right), to $30°$ (bottom right) and up to $5°$. For comparison, the analogous figures for the other methods are attached in the appendix as Figure A.3 and A.4.

Chapter 8

The *b*-value

Up until now, the *b*-value has been used as means to classify galaxies and differentiate observed evolution steps. In the following analysis, I want to focus on the *b*-value itself and how it evolves over time, as well as investigate on a link between the final morphological state of a galaxy and its history.

## 8.1 Flip Angles and Morphological Changes

In the introduction to the *b*-value in chapter 3, an overview over morphological changes, their starting point and a connection to flip angles was presented in Figure 3.17 and 3.19. In Figure 8.1, I want to present the same topic in a different way. The figure shows directly, that there is a correlation between the starting *b*-value and the flip angle with disks showing significantly more stability The trend is mostly observable for smaller angles below 30° and continuing up to 50° for instant transitions, and a more continuous distribution towards larger flip values when looking at longer time steps. Beyond that angle, the figure shows a large scatter, telling us that large flip angles happen to all types of galaxies, but favoring ellipticals. The colors provide us with information on how the galaxies are affected. For $\phi_{\text{flip}} \simeq 0°$, the galaxies are stable and the color gradient follows the color bar, as the position matches the color. As flip angles increase, it can be observed that the galaxies lose rotational support, which agrees with previous results. For long-term transitions, there even appears to be a trend with disks being destroyed sooner than intermediates with increasing flip angles. While it would be exciting to find a function to describe this, the claim could be an effect of the colorization scheme and requires further analysis.

As we find that large flips shift galaxies towards the elliptical class, it would be interesting to find a direct connection of a change of morphology and the flip angle. In Figure 8.2 one

(a) Instant transition, mean b_{post} coloration

(b) Long-term transition, mean b_{post} coloration

(c) Instant transition, heat map

(d) Long-term transition, heat map
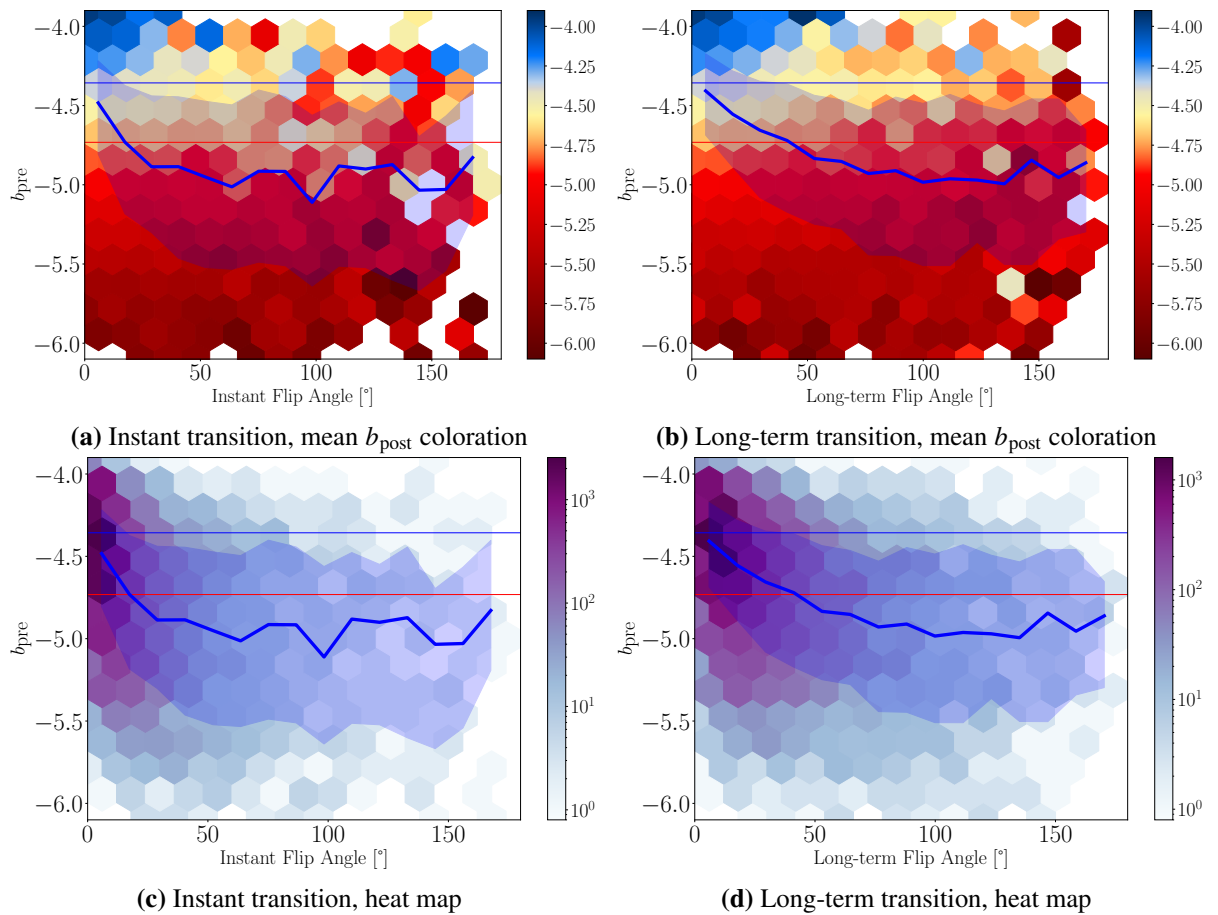
Figure 8.1: *b*-values before a transition on the y-axis plotted against the upcoming spin flip angle on the x-axis. The red and blue vertical lines highlight the borders between disks, intermediates and ellipticals. The blue line and shade follow the running median and 68th-percentile regions. The bottom figures show logarithmically colored heat maps, while the coloration at the top is determined by the mean *b*-value after spin flips. Instant and long-term transitions are compared by left- and right-hand figures.

can find a strong limit of a stable morphology on the possible flip angles. As we look into cases with more intense morphological changes, we find quickly scattering distribution of flip angles, symmetrically for $\Delta b > 0$ and $\Delta b < 0$. The figure also brings a smooth gradient to light about losses of rotational support experienced by disks and gains by ellipticals. Like for Figure 8.1b, long-term transitions seem to reveal distinct trends that resemble the image of Figure 5.4.

(a) Instant transitions   **(b)** Long-term transitions
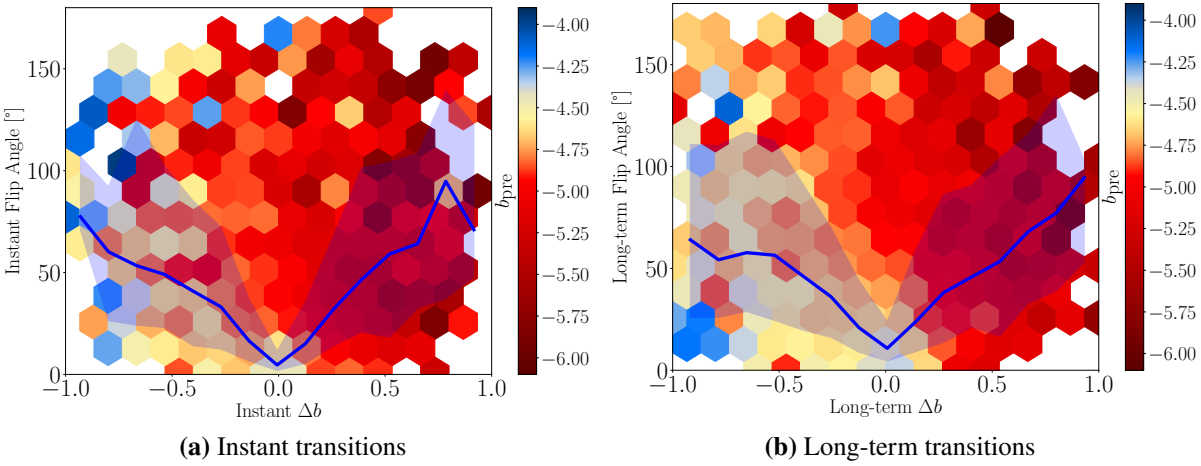
Figure 8.2: Connection of ϕ_{flip} to morphological changes Δb. The blue line and shades trace the running median and 68th-percentile regions. The colors indicate the mean galaxy morphology prior to the time step in a bin.

8.2   Final Galactic State and its History

Table 6.1 indicates that most transitions that come with a switch of morphological class are towards lower b-values, which shows what happens over the small scale steps. However, the goal of this section is to outline a greater picture and investigate on whether the final morphological state of a galaxy can be connected to its formation history.

Figure 8.3 highlights points out how the final morphological state can be connected to the number flips a galaxy has gone through. Especially for small-angle flips, the high order of stability in the history of disks stands out compared to ellipticals, which cover a broad spectrum of stable and turbulent histories. As the flip angle threshold rises the trend becomes weaker, while transitions of a length of one gigayear overall show higher counts. While flip angles of more than 90° in magnitude are generally rare, ellipticals do not seem to dominate those transitions any longer.

From a point of view on structure formation, it is also interesting to see, if we can also link morphology to a galaxies accretion history. This is done in Figure 8.4 which compares the number of mergers over a stellar mass threshold a galaxy has accreted to its morphological state at $z = 0$. The figure reveals a similar trend for a weaker effect for larger thresholds as the cases of major mergers become rare for all galaxies. With most galaxies experiencing no or very few mergers, we can observe a similar trend as ellipticals do tend to have varying merger accretion histories, while disks are dominated by histories of few or no merger encounters.

To summarize the chapter, we can conclude several aspects of morphological evolution of galaxies. The most common transitions are losses of rotational support, while ellipticals can
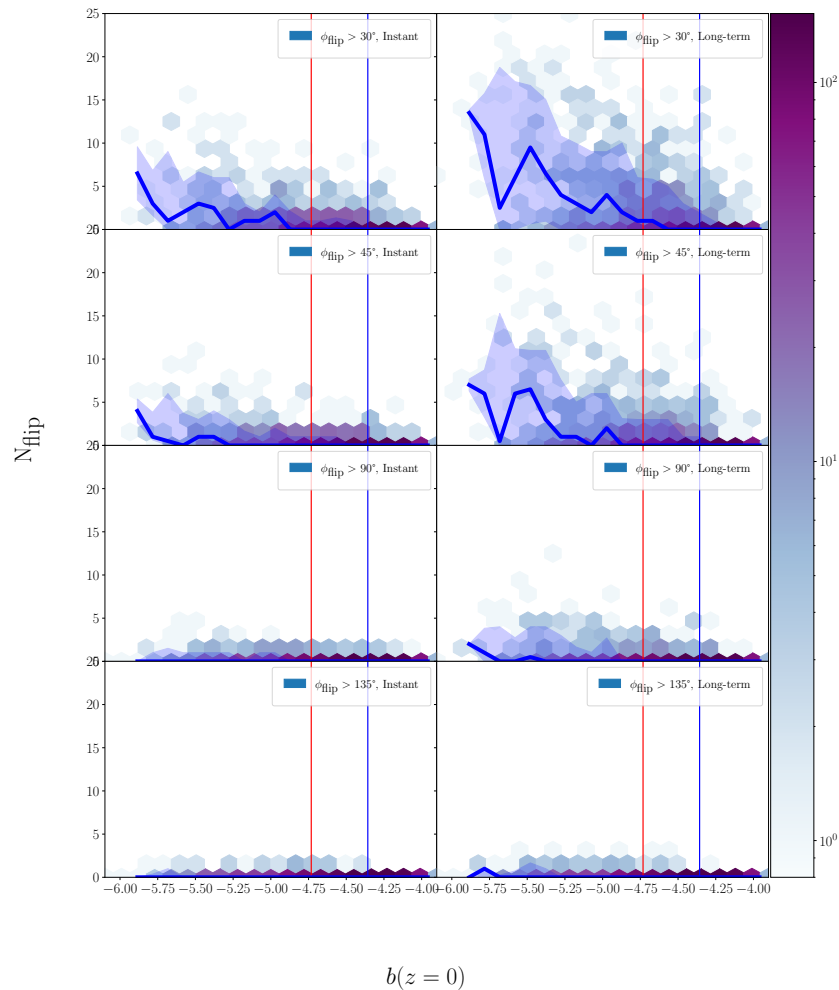
Figure 8.3: Heat map of counts of flip angles of a galaxy compared to its final morphological state at $z = 0$. The blue and red vertical lines separate the morphological classes. Left- and right-hand sub-panels differ by the time-step sizes for transitions. From top to bottom, different flip angle thresholds are applied for counting the cases as $\phi_{\text{flip}} \geq 30°$, $\phi_{\text{flip}} \geq 45°$, $\phi_{\text{flip}} \geq 90°$ and $\phi_{\text{flip}} \geq 135°$

also gain spin over time. For the formation histories of galaxies, we can confirm expectations from observations as disks at $z = 0$ have a quiet history with few mergers and spin flips while ellipticals show a broad range of formation histories from calm to turbulent. In follow-up studies, I would like to compare the end states of the galaxies to the point of their peak *b*-value to better distinguish the formation histories of galaxies that have always been purely spheroidal and susceptible to large flips from the galaxies that had distinct disks at one point and experienced drastic changes of their morphology.
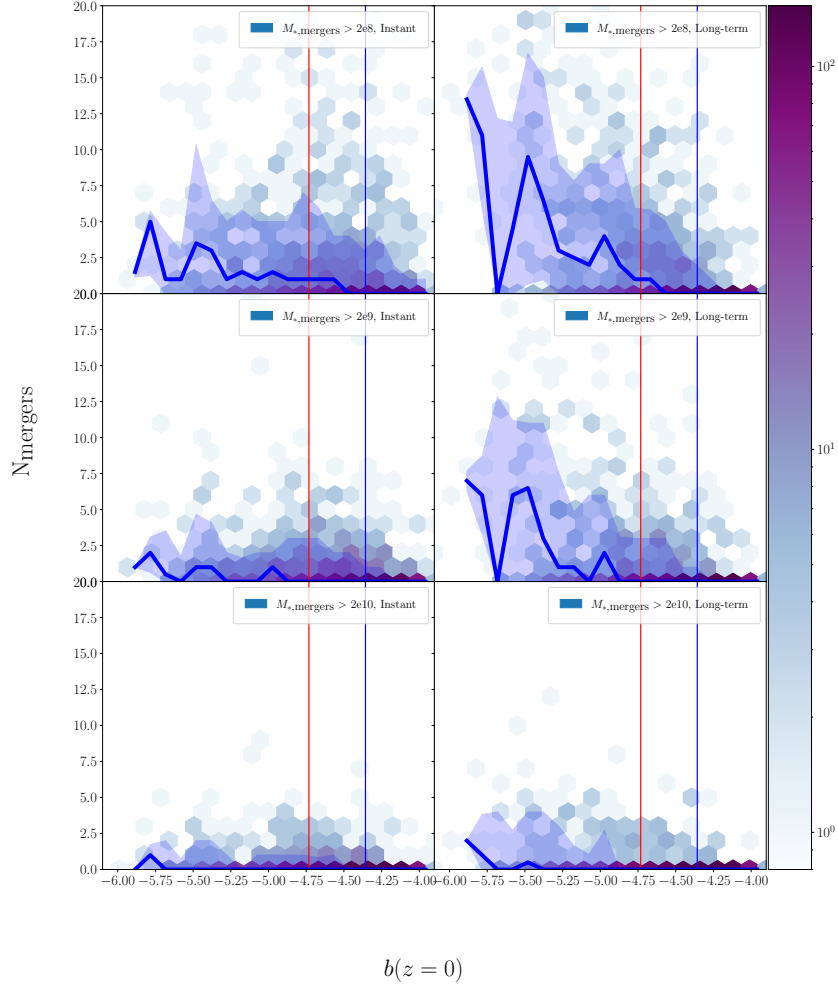
Figure 8.4: Heat map of counts of flip angles of a galaxy compared to its final morphological state at $z = 0$. The blue and red vertical lines separate the morphological classes. Left- and right-hand sub-panels differ by the time-step sizes for transitions. From top to bottom, different merger mass thresholds are applied for counting the cases as $M_{\text{merger}} \geq 2 \cdot 10^8$, $M_{\text{merger}} \geq 2 \cdot 10^9$ and $M_{\text{mergers}} \geq 2 \cdot 10^1 0$

Chapter 9

Summary and Conclusion

The kinematic evolution of galaxies has been an ongoing topic since their discovery. The great variety of shapes and features associated with galaxies naturally raises the question of how all the different structures like bulges, disks, bars, arms, shells, rings and different colors that we can observe today were produced. Today, most features have well-established explanations, that are often related to merger events, the formation history that leads to the current state of a galaxy is often still ambiguous and its relation to the cosmic web is subject of current research (Welker et al., 2014, 2020; Malavasi et al., 2021). In this project I shed light onto how turbulent these evolution paths can be by studying angular momentum and the derived quantities b-value and flip angle. I showed how robust different types of galaxies are, how well kinematic changes can be related to different types of merger events and to what degree observations at $z = 0$ can reveal about the formation history of a galaxy. The MAGNETICUM PATHFINDER simulations provide the ideal tools to study the evolution of galaxies over cosmic time scales from the formation of the first halos initiating the epoch of reionization all the way to $z = 0$. While in theory simulations provide perfect information, they also ask us to interpret it carefully. Tracing galaxies through time in simulations requires us to detect (sub-)structures which is achieved through algorithms such as SUBFIND. We then link the subhalos across time to reconstruct their formation and merger history, which creates a tree-like structure as merger events create nodes where the histories of the progenitors branch off. The numerical problem of limited time resolution with snapshots is less of an issue than conceptually disentangling subhalos in a dynamic environment with collisions and particle exchange through galaxy stripping. With the central-switch method I have used an approach that suits the selection of central subhalos of a friend-of-friend group and reflects the expectation that only subhalos dominating their group can take the position of a central halo in the next step. Solving ambiguity and improving transitions to function as expected remains to be left to future work.

One problem tackled during this work was how to interpret the kinematic information of galactic angular momentum in an environment with other nearby subhalos. The approach taken was to identify fly-by events by looking for transitions that are nearly reverted in the next transition, as the spin vector flips back after the fly-by. In order to focus on long-lasting spin modifications, such fly-by transitions were removed from the analysis, a method that can be fine-tuned in future work. Such refinement can be achieved by considering anomalies in the phase space as fly-by events should show up as clusters there. Further, the differences between the mass within R_{vir} and in the 10%-R_{vir} sphere for the spin calculation as well as between the spin vectors for these radii could forecast spin flips, as the fly-by galaxy is included earlier at R_{vir} In most cases the stellar mass is covered by the smaller sphere but such cases could hint at dynamic events. A more computationally expensive approach could be tracing single particles to disentangle the causes for spin flips.

This work provides an extensive overview of the evolution of galaxies in the highest-resolution simulation of MAGNETICUM PATHFINDER and the kinematic changes that shape their formation histories. An important aspect throughout the analysis was the differentiation by galactic morphology and the impact of spin changes on the morphology. For that, I used the kinematic b-value (Teklu et al., 2015) that provides a straightforward tool to quantify a galaxy's morphology. Thereby, it could be confirmed that the bulk of morphological transitions are from rotation- to dispersion-dominated states, which agrees with the global evolution trend of galaxies in observations in the bottom-up structure formation model. Connected to the b-value, an interesting finding was the relation with star-formation. Disks are known for their higher star-formation rates in observation, while ellipticals are usually found in a quenched state. This is also used in observations for classification when galaxies are not spatially resolved but spectral data is available. While this trend is true, it is strongly dependent on the epoch of the universe as the steepness of the relation declines towards lower redshifts. At the same time, star-formation rates are related to disturbances of the stellar angular momentum, but only at earlier redshifts. The dependence on redshift highlights the importance of considering the availability of cold gas. In subsequent work, studying the contribution of gas to the spin evolution of the stellar component could be used to explicitly show how stellar disks form, as the accretion of stellar mass still leaves gaps to fill when predicting stellar spin changes.

The prediction of spin changes in this work was done by calculating the angular momentum of infalling mergers. By tracing the merger scenario back in time until roughly 1 Gyr before the event, the spin change magnitude could be predicted well on average. When differentiating the predictions by morphology, a systematic underprediction for disks undergoing small spin changes of $10^{12} M_{\odot}$ kpc km/s $\geq |\Delta J_*| \geq 10^{13} M_{\odot}$ kpc km/s emerges. While the prediction of ΔJ from mergers works rather well and systematic errors in slope and offset, these errors have

a large impact on the prediction of the flip angle, which appears barely correlated. In future work, predicting the flip angles properly could help with disentangling the influence of other aspects in the kinematic interplay with the galaxies. Among them are smooth accretion, the gas and dark matter components and the impact of the tidal field acting on the galaxies and reconsiderations about how to assign particles to subhalos or the central halo.

When comparing the theoretical expectations of relative spin change magnitudes and flip angles with the observed transitions, a surprising result was found regarding the different behaviors among the morphological classes: In the cases with angular momentum changes that overwhelm the intrinsic spins, galaxies with higher rotational support tend to experience spin changes aligned with their initial spin. This suggests that disks tend to sit in an environment with alignment to them. Further investigation into the reasons behind this could reveal interesting details of the galaxy formation histories and even show a connection to satellite planes (Förster, 2019). If this affects mainly low-mass galaxies at higher redshifts, it would fit well into the image of galaxies gaining angular momentum as they accrete onto filaments and then lose rotational support on the way towards the nodes of the cosmic web.

In the attempt to relate the morphological classes of galaxies at $z = 0$ to their formation histories, a very clear picture was drawn. The bulk of disk galaxies has had few spin flips larger than $\phi_{\text{flip}} = 30°$ in its formation history, while ellipticals show a broad range of evolutions from turbulent to conservative. This could be a consequence of ellipticals having small rotational support that easily flips compared to disks. However, the same relation is shown for their merger histories, so there is a physical connection to flips. As a next step, I would like to compare the final states of galaxies to their peak b-values to answer the hen-or-egg question if flips create ellipticals or if ellipticals just tend to flip more often.

I present a first approach to the analysis of spin transitions in the MAGNETICUM PATHFINDER simulations which serves as a signpost for future research on the topic. This includes approaches to numerical methods to help interpret the galactic formation histories in simulations. Throughout the analysis in this project, the b-value and its classification thresholds have proven to be a very consistent measure for robustness of a halo against disturbances. Distinguishing by it revealed different signals for spin changes. Identifying disks at $z = 0$ using the b-value gives a very high chance to find isolated galaxies, that never had any major disturbances. And while it is calculated independently of gas particles, it also correlated with star-formation rates. In this picture, mergers are found to be related to kinematic changes and star-formation rates but there is still a significant gap to close by other influences. This issue was mainly revealed by considering flip angles, a quantity that served as a signal for turbulence like spin change magnitudes. However, correlations between flip angles and other quantities like star-formation or even for predictions were usually only found below 30° or 50°, depending on the time scales.

This range is also the most likely transition of galactic spins while greater flips occur significantly less frequent. Focusing on this range could prove beneficial to finding better-constrained relations to causes of disturbances of galaxies. In future work, the formation history of galaxies can be put into the context of the cosmic web. For comparability with observations, a structure finder algorithm like DISPERSE (Sousbie, 2011; Sousbie et al., 2011) could be used. This way, the alignment of galaxy spins with filaments can be tested along the travel path from voids to walls, from walls to filaments and finally from filaments to nodes. While observations struggle with high uncertainties from working with projected spin and filament orientation as done by Welker et al. (2020), cosmological hydrodynamical simulations could reveal features with higher confidence.

Appendix A

Appendix

A.1 The Galaxy Sample
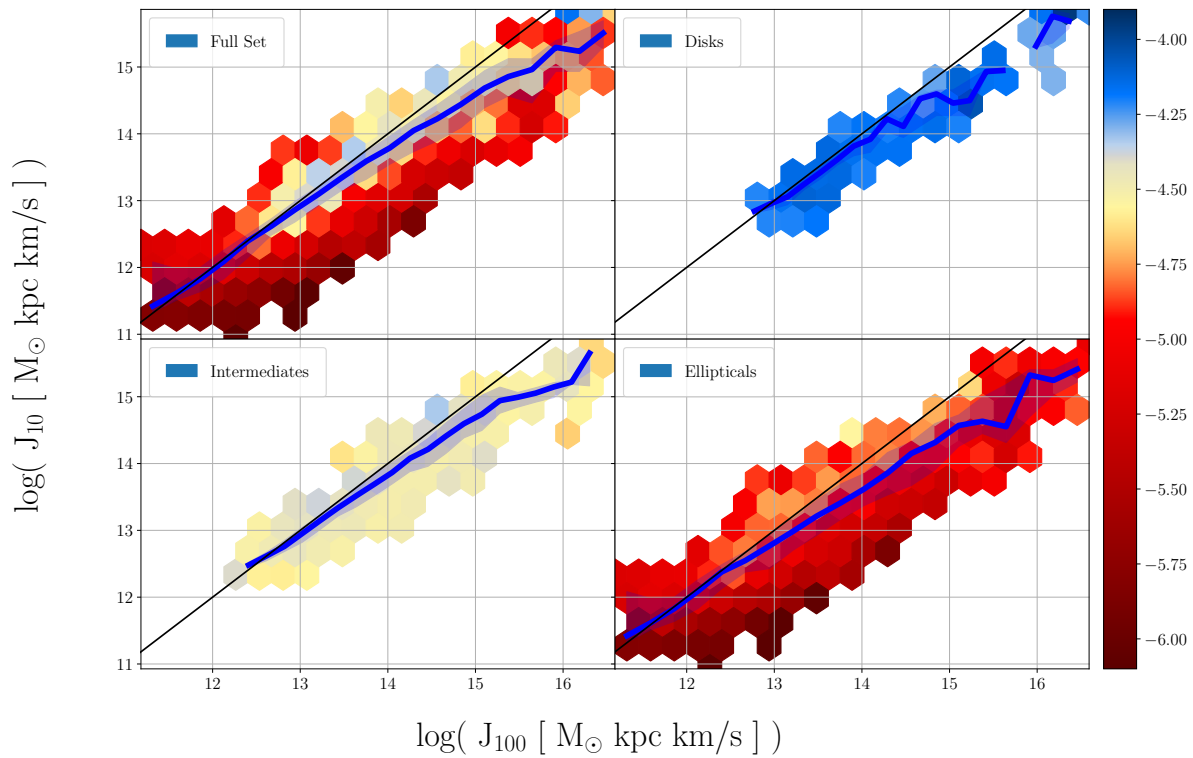
Figure A.1: Stellar spin magnitude within 10% of the virial radius plotted against the value within the full virial radius. The colors represent the average b-value in a bin. The black line marks the theoretical perfect-agreement relation. The blue line and shade follow the running median and 68th-percentile area of the sample distribution.

A.2   Mergers

(a) Instant flips, immediate J_{merger}

(b) Instant flips, earlier J_{merger}

(c) Long-term flips, immediate J_{merger}

(d) Long-term flips, earlier J_{merger}
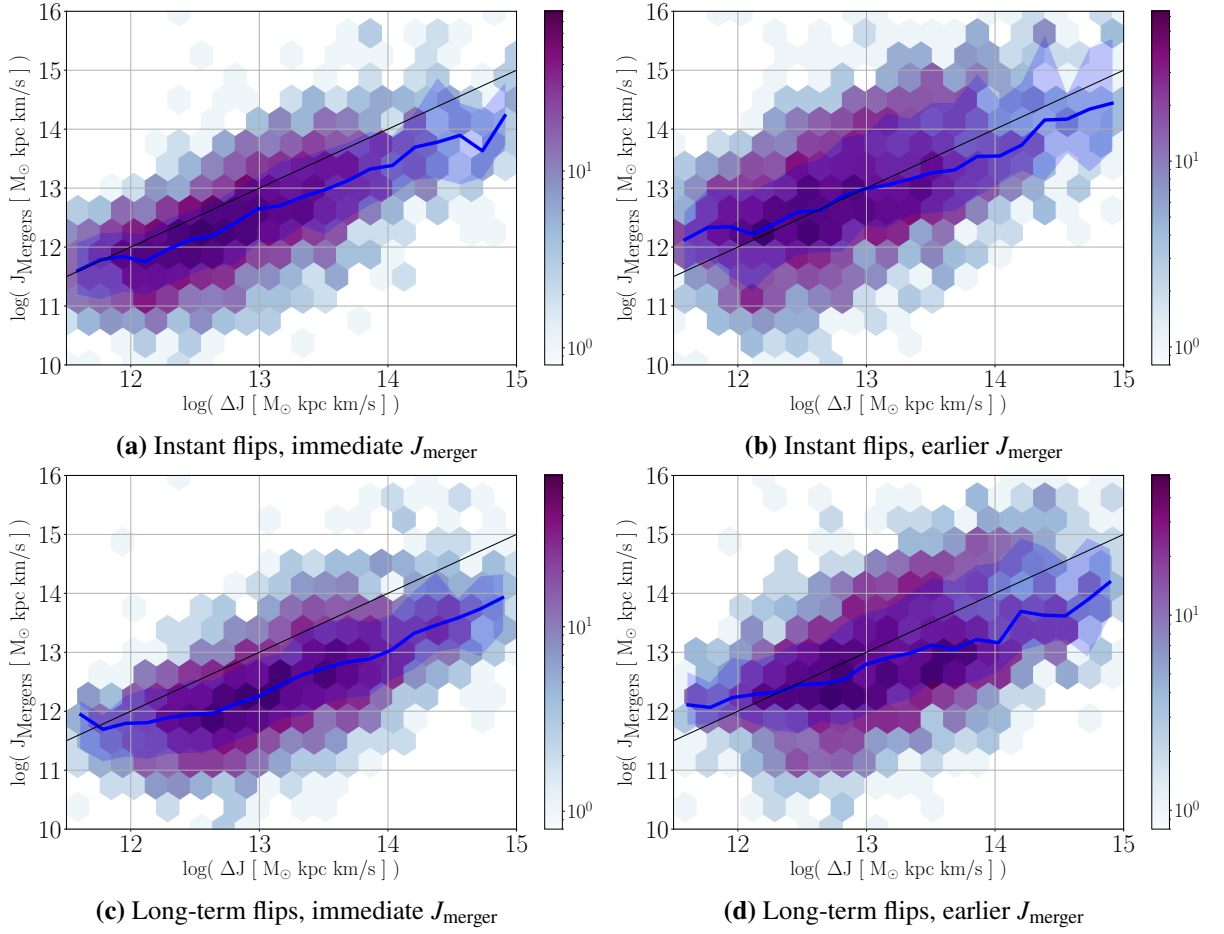
Figure A.2: Heat map of the angular momentum that is expected from the incoming mergers plotted against the actual measured change over a transition. The black line marks the one-to-one relation. The blue line and shade trace the running median and 68th percentiles. The figures on top show instant transitions, whereas the bottom row shows long-term transitions. On the left, the merger orbital spins are calculated as soon as possible before the merger is registered. On the right, the mergers were traced back by roughly 1 gigayear and their orbital spin with respect to the galaxy was evaluated there. The corresponding heat map is provided by Figure A.2 in the appendix.

(a) log-log scale

(b) $0° \leq \phi_{\text{flip}} \leq 180°$

(c) $0° \leq \phi_{\text{flip}} \leq 30°$

(d) $0° \leq \phi_{\text{flip}} \leq 5°$
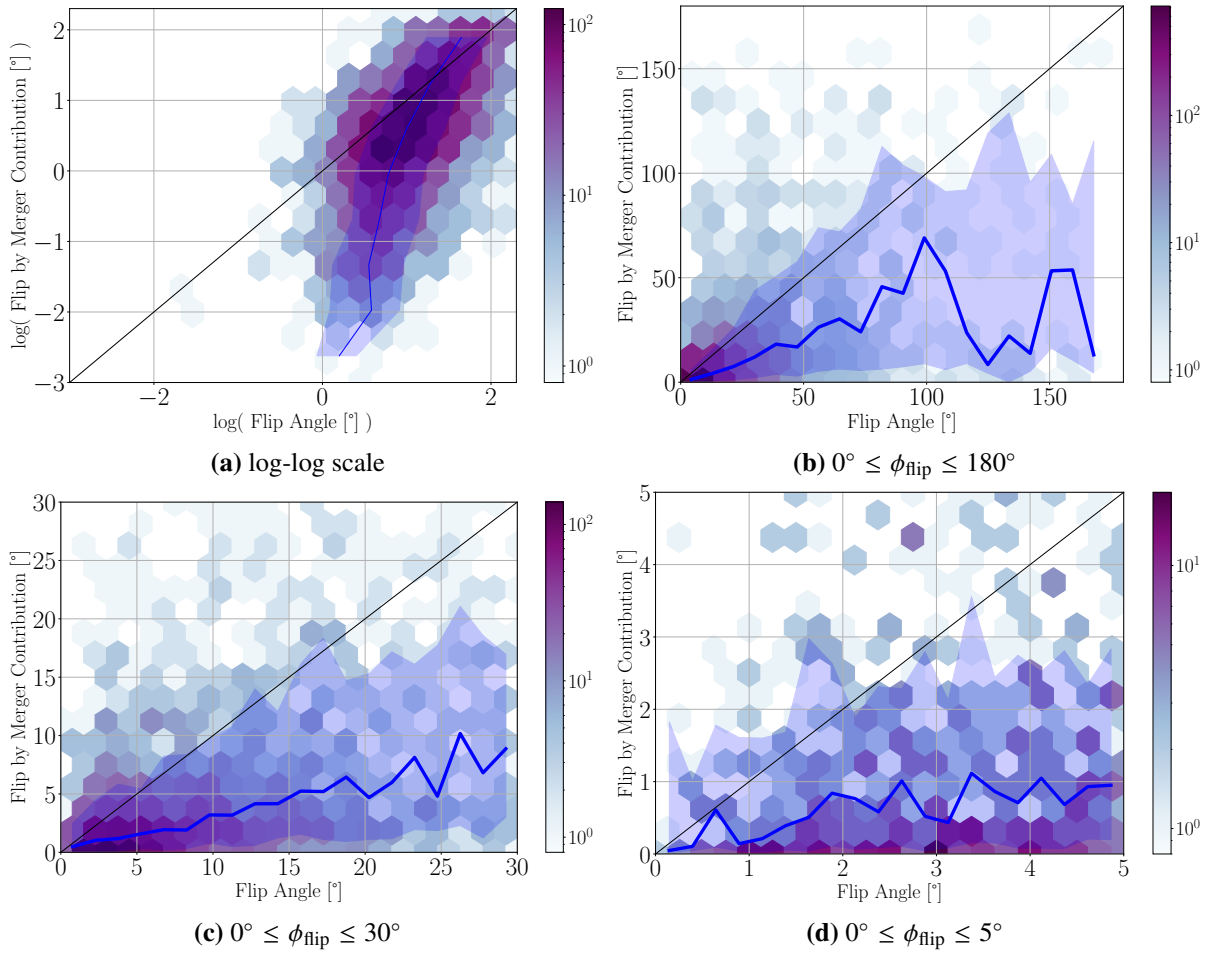
Figure A.3: Prediction of flip angles by merger spin transport compared to measured instant flip angles on a logarithmic heat map. The merger spin was measured immediately before the merger event for this figure. The black line marks the theoretical one-to-one relation. The blue line and shades follow the running median and 68th-percentile regions. The top-left figure covers the full range of angles $0° \geq \phi_{\text{flip}} \geq 180°$ on a double-log scale. The other three plots show linear scales with different ranges from $0°$ to $180°$ (top right), to $30°$ (bottom right) and up to $5°$.

(a) log-log scale

(b) $0° \leq \phi_{\text{flip}} \leq 180°$

(c) $0° \leq \phi_{\text{flip}} \leq 30°$

**(d)** $0° \leq \phi_{\text{flip}} \leq 5°$
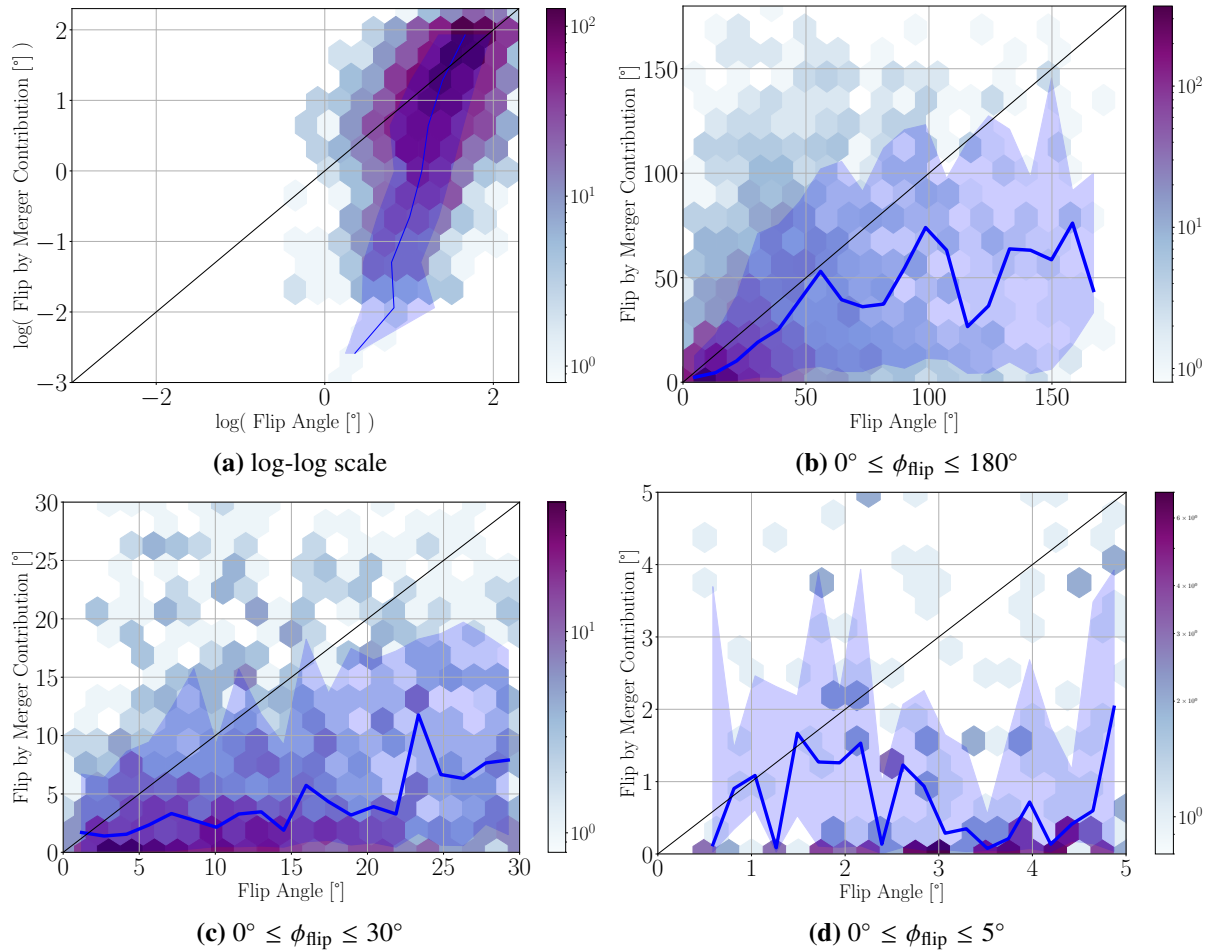
Figure A.4: Prediction of flip angles by merger spin transport compared to measured long-term flip angles on a logarithmic heat map. The merger spin was measured roughly one gigayear prior to the merger event for this figure. The black line marks the theoretical one-to-one relation. The blue line and shades follow the running median and 68th-percentile regions. The top-left figure covers the full range of angles $0° \geq \phi_{\text{flip}} \geq 180°$ on a double-log scale. The other three plots show linear scales with different ranges from 0° to 180° (top right), to 30° (bottom right) and up to 5°.

A.3   Spin Transitions

(a) Instant, $\Delta J/J_{\mathrm{pre}}$

(b) Instant, $\Delta J/J_{\mathrm{post}}$

(c) Long-term, $\Delta J/J_{\mathrm{pre}}$
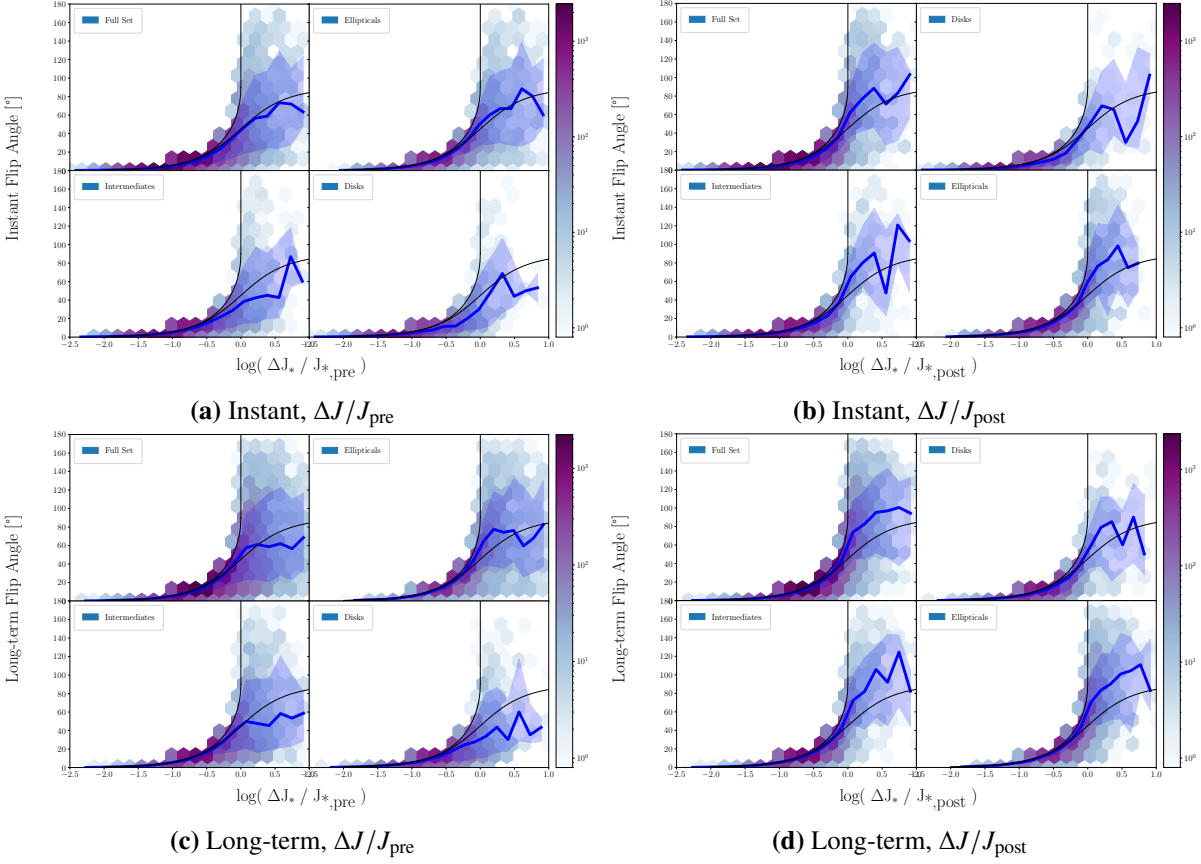
(d) Long-term, $\Delta J/J_{\mathrm{post}}$

Figure A.5: Heat map of flip angles ϕ_{flip} plotted against spin changes ΔJ relative to the angular momentum prior to the flip J_{pre} (left-hand figures) and after the transition J_{post} (right-hand figures) over instant time-steps at the top and long-term transitions at the bottom. Flip angles ϕ_{flip} plotted against ΔJ_{rel} over instant time-steps at the top and long-term transitions at the bottom. The blue lines and shades trace the running median and 68th percentiles. The black lines show the theoretical limit and expectation for random changes as described in Equation 5.9 and 5.10.

(a) J_{post}, Instant

(b) j_{post}, Instant

(c) J_{post}, Long-term
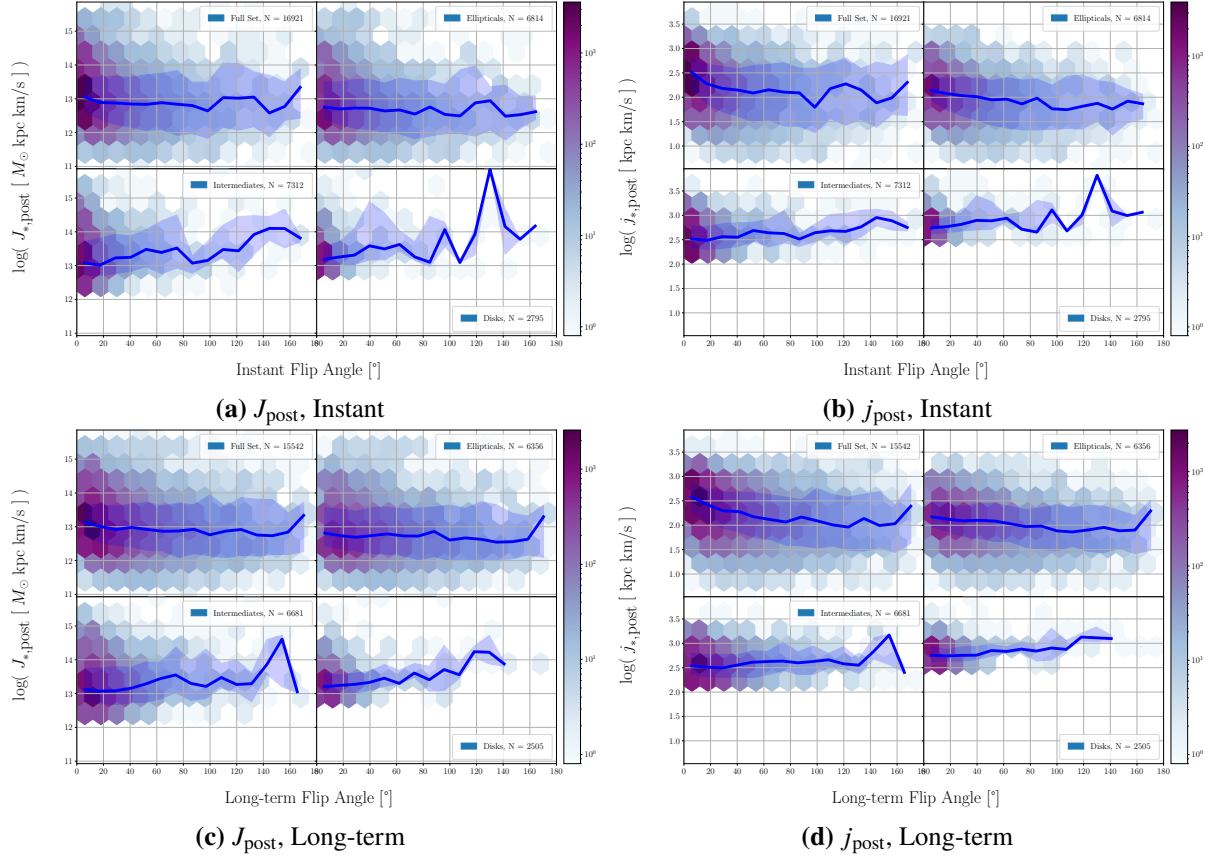
(d) j_{post}, Long-term

Figure A.6: Heat map in logarithmic colors of spin magnitudes prior to a time step plotted against the past flip angle. J_{post} is used in the left-hand figures, j_{post} on the right. The top figures display instant transitions and long-term ones lie at the bottom. The blue lines and shades mark the running median and 68th percentiles. Each figure is divided into sub-panels with the full sample, elliptical galaxies, intermediates and disks.

References

Abadi, M. G., Navarro, J. F., Steinmetz, M., & Eke, V. R. (2003). Simulations of Galaxy Formation in a Λ Cold Dark Matter Universe. II. The Fine Structure of Simulated Galactic Disks. *ApJ*, *597*(1), 21–34.

Aubert, D., Pichon, C., & Colombi, S. (2004). The origin and implications of dark matter anisotropic cosmic infall on L_* haloes. *MNRAS*, *352*(2), 376–398.

Baldry, I., Liske, J., & Driver, S. P. (2008). GAMA: a new galaxy survey. In M. Bureau, E. Athanassoula, & B. Barbuy (Eds.) *Formation and Evolution of Galaxy Bulges*, vol. 245, (pp. 83–84).

Birnboim, Y., & Dekel, A. (2003). Virial shocks in galactic haloes? *MNRAS*, *345*(1), 349–364.

Cooper, K. (2022). James webb space telescope beats its own record with potential most distant galaxies. (accessed: 07.08.2022).
URL https://www.space.com/james-webb-space-telescope-new-most-distant-galaxies

Cortese, L. (2016). Astronomers shed light on different galaxy types. (accessed: 01.08.2022).
URL https://phys.org/news/2016-09-astronomers-galaxy.html

Dekel, A., Birnboim, Y., Engel, G., Freundlich, J., Goerdt, T., Mumcuoglu, M., Neistein, E., Pichon, C., Teyssier, R., & Zinger, E. (2009). Cold streams in early massive hot haloes as the main mode of galaxy formation. *Nature*, *457*(7228), 451–454.

Dolag, K. (2016a). Pictures - magneticum pathfinder & magneticum. (accessed: 01.08.2022).
URL http://www.magneticum.org/media.html#PICTURES

Dolag, K. (2016b). Simulations - magneticum pathfinder & magneticum. (accessed: 02.08.2022).
URL http://www.magneticum.org/simulations.html

Dolag, K., Borgani, S., Murante, G., & Springel, V. (2009). Substructures in hydrodynamical cluster simulations. *MNRAS*, *399*(2), 497–514.

Dubois, Y., Pichon, C., Welker, C., Le Borgne, D., Devriendt, J., Laigle, C., Codis, S., Pogosyan, D., Arnouts, S., Benabed, K., Bertin, E., Blaizot, J., Bouchet, F., Cardoso, J. F., Colombi, S., de Lapparent, V., Desjacques, V., Gavazzi, R., Kassin, S., Kimm, T., McCracken, H., Milliard, B., Peirani, S., Prunet, S., Rouberol, S., Silk, J., Slyz, A., Sousbie, T., Teyssier, R., Tresse, L., Treyer, M., Vibert, D., & Volonteri, M. (2014). Dancing in the dark: galactic properties trace spin swings along the cosmic web. *MNRAS*, *444*(2), 1453–1468.

Emsellem, E., Cappellari, M., Krajnović, D., van de Ven, G., Bacon, R., Bureau, M., Davies, R. L., de Zeeuw, P. T., Falcón-Barroso, J., Kuntschner, H., McDermid, R., Peletier, R. F., & Sarzi, M. (2007). The SAURON project - IX. A kinematic classification for early-type galaxies. *MNRAS*, *379*(2), 401–417.

Fall, S. M. (1983). Galaxy formation - Some comparisons between theory and observation. In E. Athanassoula (Ed.) *Internal Kinematics and Dynamics of Galaxies*, vol. 100, (pp. 391–398).

Fall, S. M., & Romanowsky, A. J. (2013). Angular Momentum and Galaxy Formation Revisited: Effects of Variable Mass-to-light Ratios. *ApJ*, *769*(2), L26.

Förster, P. U. (2019). *Planes of Satellite Galaxies in Large-scale Cosmological Simulations*. Master's thesis, University Observatory Munich.
URL https://www.usm.uni-muenchen.de/~halos/theses/MA_foerster.pdf

Gaia Collaboration (2016). The Gaia mission. *A&A*, *595*, A1.

Hirschmann, M., Dolag, K., Saro, A., Bachmann, L., Borgani, S., & Burkert, A. (2014). Cosmological simulations of black hole growth: Agn luminosities and downsizing. *Monthly Notices of the Royal Astronomical Society*, *442*, 2304–2324.

Hwang, J.-S., Park, C., Nam, S.-h., & Chung, H. (2021). Evolution of the Spin of Late-type Galaxies Caused by Galaxy-galaxy Interactions. *Journal of Korean Astronomical Society*, *54*, 71–88.

Khandai, N., Di Matteo, T., Croft, R., Wilkins, S., Feng, Y., Tucker, E., DeGraf, C., & Liu, M.-S. (2015). The MassiveBlack-II simulation: the evolution of haloes and galaxies to z ~ 0. *MNRAS*, *450*(2), 1349–1374.

Kimmig, L. C. (2022). *Are You Bound or Just Projected? The Behavior of Substructures From Expansion to Galaxy Clusters*. Master's thesis, University Observatory Munich.
URL https://www.usm.uni-muenchen.de/~halos/theses/MA_kimmig_lucas.pdf

Knebe, A., Gill, S. P. D., Gibson, B. K., Lewis, G. F., Ibata, R. A., & Dopita, M. A. (2004). Anisotropy in the Distribution of Satellite Galaxy Orbits. *ApJ*, *603*(1), 7–11.

Komatsu, E., Smith, K. M., Dunkley, J., Bennett, C. L., Gold, B., Hinshaw, G., Jarosik, N., Larson, D., Nolta, M. R., Page, L., Spergel, D. N., Halpern, M., Hill, R. S., Kogut, A., Limon, M., Meyer, S. S., Odegard, N., Tucker, G. S., Weiland, J. L., Wollack, E., & Wright, E. L. (2011). Seven-year Wilkinson Microwave Anisotropy Probe (WMAP) Observations: Cosmological Interpretation. *ApJS*, *192*(2), 18.

Kudritzki, R.-P., Teklu, A. F., Schulze, F., Remus, R.-S., Dolag, K., Burkert, A., & Zahid, H. J. (2021). Galaxy Look-back Evolution Models: A Comparison with Magneticum Cosmological Simulations and Observations. *ApJ*, *910*(2), 87.

Madau, P., & Dickinson, M. (2014). Cosmic Star-Formation History. *ARA&A*, *52*, 415–486.

Malavasi, N., Langer, M., Aghanim, N., Galárraga-Espinosa, D., & Gouin, C. (2021). The effect of nodes and filaments on the quenching and the orientation of the spin of galaxies. In A. Siebert, K. Baillié, E. Lagadec, N. Lagarde, J. Malzac, J. B. Marquette, M. N'Diaye, J. Richard, & O. Venot (Eds.) *SF2A-2021: Proceedings of the Annual meeting of the French Society of Astronomy and Astrophysics. Eds.: A. Siebert*, (pp. 399–400).

Masters, K. (2019). The hubble tuning fork illustrated with images of nearby galaxies from the sloan digital sky survey (sdss). (accessed: 01.08.2022).
URL https://ras.ac.uk/media/37

Mayer, A. C., Teklu, A. F., Dolag, K., & Remus, R.-S. (2022). ΛCDM with baryons vs. MOND: the time evolution of the universal acceleration scale in the Magneticum simulations. *arXiv e-prints*, (p. arXiv:2206.04333).

Mo, H. J., Mao, S., & White, S. D. M. (1998). The formation of galactic discs. *MNRAS*, *295*(2), 319–336.

Nelson, D., Pillepich, A., Springel, V., Weinberger, R., Hernquist, L., Pakmor, R., Genel, S., Torrey, P., Vogelsberger, M., Kauffmann, G., Marinacci, F., & Naiman, J. (2018). First results from the IllustrisTNG simulations: the galaxy colour bimodality. *MNRAS*, *475*(1), 624–647.

Obreschkow, D., Glazebrook, K., Bassett, R., Fisher, D. B., Abraham, R. G., Wisnioski, E., Green, A. W., McGregor, P. J., Damjanov, I., Popping, A., & Jørgensen, I. (2015). Low angular momentum in clumpy, turbulent disk galaxies. *Astrophysical Journal*, *815*.

Oegerle, W. R., & Hoessel, J. G. (1991). Fundamental Parameters of Brightest Cluster Galaxies. *ApJ*, *375*, 15.

Oser, L., Ostriker, J. P., Naab, T., Johansson, P. H., & Burkert, A. (2010). The Two Phases of Galaxy Formation. *ApJ*, *725*(2), 2312–2323.

Peebles, P. J. E. (1993). *Principles of Physical Cosmology*. Princeton University Press.

Romanowsky, A. J., & Fall, S. M. (2012). Angular Momentum and Galaxy Formation Revisited. *ApJS*, *203*(2), 17.

Scannapieco, C., Tissera, P. B., White, S. D. M., & Springel, V. (2008). Effects of supernova feedback on the formation of galaxy discs. *MNRAS*, *389*(3), 1137–1149.

Schaye, J., Crain, R. A., Bower, R. G., Furlong, M., Schaller, M., Theuns, T., Dalla Vecchia, C., Frenk, C. S., McCarthy, I. G., Helly, J. C., Jenkins, A., Rosas-Guevara, Y. M., White, S. D. M., Baes, M., Booth, C. M., Camps, P., Navarro, J. F., Qu, Y., Rahmati, A., Sawala, T., Thomas, P. A., & Trayford, J. (2015). The EAGLE project: simulating the evolution and assembly of galaxies and their environments. *MNRAS*, *446*(1), 521–554.

Schulze, F., Remus, R.-S., Dolag, K., Burkert, A., Emsellem, E., & van de Ven, G. (2018). Kinematics of simulated galaxies - I. Connecting dynamical and morphological properties of early-type galaxies at different redshifts. *MNRAS*, *480*(4), 4636–4658.

Sousbie, T. (2011). The persistent cosmic web and its filamentary structure - I. Theory and implementation. *MNRAS*, *414*(1), 350–383.

Sousbie, T., Pichon, C., & Kawahara, H. (2011). The persistent cosmic web and its filamentary structure - II. Illustrations. *MNRAS*, *414*(1), 384–403.

Springel, V., & Hernquist, L. (2002). Cosmological smoothed particle hydrodynamics simulations: the entropy equation. *MNRAS*, *333*(3), 649–664.

Springel, V., & Hernquist, L. (2003). Cosmological smoothed particle hydrodynamics simulations: a hybrid multiphase model for star formation. *MNRAS*, *339*(2), 289–311.

Springel, V., White, S. D. M., Tormen, G., & Kauffmann, G. (2001). Populating a cluster of galaxies - I. Results at [formmu2]z=0. *MNRAS*, *328*(3), 726–750.

Teklu, A. F., Remus, R. S., & Dolag, K. (2016). Dynamical Properties of Galaxies with Different Morphological Types at z=0 and z=2. In S. F. Sanchez, C. Morisset, & G. Delgado-Inglada (Eds.) *The Interplay between Local and Global Processes in Galaxies,*, (p. 41).

Teklu, A. F., Remus, R. S., Dolag, K., Beck, A. M., Burkert, A., Schmidt, A. S., Schulze, F., & Steinborn, L. K. (2015). Connecting angular momentum and galactic dynamics: The complex interplay between spin, mass, and morphology. *Astrophysical Journal*, *812*.

The Dark Energy Survey Collaboration (2005). The Dark Energy Survey. *arXiv e-prints*, (pp. astro–ph/0510346).

Tully, R. B., & Fisher, J. R. (1977). A new method of determining distances to galaxies. *A&A*, *54*, 661–673.

Welker, C., Bland-Hawthorn, J., van de Sande, J., Lagos, C., Elahi, P., Obreschkow, D., Bryant, J., Pichon, C., Cortese, L., Richards, S. N., Croom, S. M., Goodwin, M., Lawrence, J. S., Sweet, S., Lopez-Sanchez, A., Medling, A., Owers, M. S., Dubois, Y., & Devriendt, J. (2020). The SAMI Galaxy Survey: first detection of a transition in spin orientation with respect to cosmic filaments in the stellar kinematics of galaxies. *MNRAS*, *491*(2), 2864–2884.

Welker, C., Devriendt, J., Dubois, Y., Pichon, C., & Peirani, S. (2014). Mergers drive spin swings along the cosmic web. *MNRAS*, *445*, L46–L50.

Williams, R. E., Blacker, B., Dickinson, M., Dixon, W. V. D., Ferguson, H. C., Fruchter, A. S., Giavalisco, M., Gilliland, R. L., Heyer, I., Katsanis, R., Levay, Z., Lucas, R. A., McElroy, D. B., Petro, L., Postman, M., Adorf, H.-M., & Hook, R. (1996). The Hubble Deep Field: Observations, Data Reduction, and Galaxy Photometry. *AJ*, *112*, 1335.

York, D. G., & SDSS Collaboration (2000). The Sloan Digital Sky Survey: Technical Summary. *AJ*, *120*(3), 1579–1587.

Acknowledgments

Selbstständigkeitserklärung

Hiermit erkläre ich, die vorliegende Arbeit selbstständig verfasst zu haben und keine anderen als die in der Arbeit angegebenen Quellen und Hilfsmittel benutzt zu haben.

München, 08.08.2022

_____

Silvio Fortuné